ULTRA-HIGH-RESOLUTION LOW-TEMPERATURE MAGNETIC FORCE MICROSCOPY

A THESIS SUBMITTED TO
THE GRADUATE SCHOOL OF NATURAL AND APPLIED SCIENCES
OF
MIDDLE EAST TECHNICAL UNIVERSITY

BY

ARASH BADAMI BEHJAT

IN PARTIAL FULFILLMENT OF THE REQUIREMENTS
FOR
THE DEGREE OF MASTER OF SCIENCE
IN
PHYSICS

SEPTEMBER 2019

Approval of the thesis:

ULTRA-HIGH-RESOLUTION LOW-TEMPERATURE MAGNETIC FORCE MICROSCOPY

submitted by **ARASH BADAMI BEHJAT** in partial fulfillment of the requirements for the degree of **Master of Science in Physics Department, Middle East Technical University** by,

Prof. Dr. Halil Kalıpçılar
Dean, Graduate School of **Natural and Applied Sciences** _____

Prof. Dr. Altug Ozpineci
Head of Department, **Physics** _____

Prof. Dr. Ahmet Oral
Supervisor, **Physics, METU** _____

Examining Committee Members:

Assoc. Prof. Dr. Sinan Kaan Yerli
Physics, METU _____

Prof. Dr. Ahmet Oral
Physics, METU _____

Assoc. Prof. Dr. Şinasi Barış Emre
Engineering Physics, Ankara University _____

Date: 09.09.2019

I hereby declare that all information in this document has been obtained and presented in accordance with academic rules and ethical conduct. I also declare that, as required by these rules and conduct, I have fully cited and referenced all material and results that are not original to this work.

Name, Surname: Arash Badami Behjat

Signature:

ABSTRACT

ULTRA-HIGH-RESOLUTION LOW-TEMPERATURE MAGNETIC FORCE MICROSCOPY

Badami Behjat, Arash
Master of Science, Physics
Supervisor: Prof. Dr. Ahmet Oral

September 2019, 103 pages

Scanning probe microscopy is a conventional technic which has opened new methods to investigate surface properties. Imaging atoms or manipulating them as well as measuring surface structures with high resolution and accuracy are fantastic features which are utilized in surface science to study the characterization of materials. Atomic Force Microscopy (AFM) a standard popular method can measure the interaction forces between the sharp tip and the sample surface. This method allows us imaging atoms individually with the atomic resolution or the structure of molecules. AFM could measure various types of forces like van der Waals, electrostatic, friction or magnetic forces under the different environment condition, high vacuum or Ultra high vacuum, ambient, and aqua, as well as high magnetic field at room or cryogenic temperature. Affordable price, easy sample preparation, and operation, specifically high resolution down to the nanometer are the advantages of this method. Moreover, ability to image almost any type of samples such surface of the ceramic material, or the dispersion of the metallic nanoparticles, or so soft material, such very flexible polymers, the human cell, and DNA is the most considerable advantages of AFM.

Magnetic Force Microscopy (MFM) is another standard method for surface investigation of magnetic properties, which is the aim of this thesis. MFM is one of the significant roles in material science that magnetic resolution of 10 nm and less,

provides critical information in the different area of science such as spintronics, spin glass system, magnetic nanoparticles, superconductivity, high-density magnetic recording media, magnetic phase transition, etc. The capability of AFM/MFM in working at a low-temperature range of 300 kelvin to hundreds of millikelvin increases the versatility of the microscope.

Principally, low-temperature Atomic/Magnetic Force Microscope (LT-AFM/MFM) is working with the measuring the cantilever deflection; This means the fiber interferometer which directs the laser light to the cantilever tip by a fiber cable can measure the deflection with calculating the percentage of laser light coming back from the tip. The significant role here is the operation of the microscope in extremely low temperature for further material evaluation and also the reliability of working that in various temperature properly.

The critical issue is microscope alignment, which the cantilever and fiber respectively could collapse in the cooling status. Therefore, the design of the microscope head should be wholly centric, and a particular mechanism aligns considering the different thermal contraction of the material. Besides, most cryogenic systems are limited in the sample space; consequently, this limitation should be applied in the whole design and system alignment.

In my master thesis, I have improved a Low-Temperature Fabry-Perot Atomic Force Microscope / Magnetic Force Microscope (LT-AFM/MFM). This instrument was developed earlier in our group and used standard tips and a Fabry-Perot fiber interferometer for measuring the cantilever deflection. The earlier version of this LT-AFM had some reliability issues with the fiber nanopositioner at low temperatures. Principally, in a Fabry-Perot AFM/MFM it is required to reduce the distance between cantilever and fiber by moving the latter. This issue is also an essential means to improve the resolution because thereby, the signal intensity of the reflected light can be increased. In the previous setup, the piezo nanopositioner was not able to move the ferrule that holds to fiber, due to the limited space in the vertical direction in the

cryostat. Therefore, I modified the design, resulting in improved reliability of the fiber nanopositioner. This was achieved by (1) centering the AFM tip at the piezo tube; (2) improving the surface quality of the groves in which the ferrule is sliding; (3) increasing the inertial mass of the fiber holder.

The new concentric design enabled the piezoelectric nanopositioner not only to move the fiber forward and backward in the vertical direction but also worked reliably and precisely at extremely low temperatures down to 300 milliKelvins. The movability of the fiber to optimize its position with respect to the cantilever is essential for the performance of the microscope. Thereby the slope is increased, i.e., the change of the signal at the photodiode with respect to a change of cantilever position, of the reflected laser signal, and hence the vertical resolution of the AFM. With this new design, a slope of 148 (mV/Å) was reached using a laser power of 3.5 mW, whereas before the slope only amounted to 120 (mV/Å). Increasing this slope also means improved vertical resolution in AFM and MFM as well.

In this research, we have improved the previously developed AFM/MFM Fabry-Perot low-temperature microscope with an outer dimension less than 25.4 mm which is completely commercialized for various types of cryogen-free cryostats from different manufacturers or liquid He bathes. All measurements conducted in the newly installed cryogen-free cryostat with the capability to reach 1.3 K from Cryomagnetic instrument; This ultra-low temperature is a vital issue in material science and also physics investigation on many phenomenon. The working potential of the microscope, in both AFM and MFM mode at various temperature, besides ultra-low noise level around 25 fm/$Hz^{1/2}$ in 300 K and 12 fm/$Hz^{1/2}$ in 1 K gives high-resolution images.

Keywords: Atomic force microscope, AFM, magnetic force microscope, MFM, low temperature, magnetic field, high resolution imaging, cryostat, milliKelvin, fibre interferometer, fibre Fabry-Pérot interferometer

ÖZ

ULTRA-YÜKSEK-ÇÖZÜNÜRLÜK DÜŞÜK SICAKLIKLI MANYETİK KUVVET MİKROSKOPİSİ

Badami Behjat, Arash
Yüksek Lisans, Fizik
Tez Danışmanı: Prof. Dr. Ahmet Oral

Eylül 2019, 103 sayfa

Tarama probu mikroskobu, yüzey özelliklerini araştırmak için yeni yöntemler açan geleneksel bir tekniktir. Atomları görüntülemek veya bunları manipüle etmek, aynı zamanda yüzey yapılarını yüksek çözünürlük ve hassasiyetle ölçmek, malzemelerin karakterizasyonunu incelemek için yüzey biliminde kullanılan fantastik özelliklerdir. Atomik Kuvvet Mikroskobu (AFM) standart bir popüler yöntemdir, keskin uç ile numune yüzeyi arasındaki etkileşim kuvvetlerini ölçebilir. Bu yöntem atomları atomik çözünürlük veya moleküllerin yapısı ile ayrı ayrı görüntülememize izin verir. AFM, farklı ortam koşulları altında van der Waals, elektrostatik, sürtünme veya manyetik kuvvetler, yüksek vakum veya Ultra yüksek vakum, ortam ve su ve ayrıca oda veya kriyojenik sıcaklıktaki yüksek manyetik alan gibi çeşitli kuvvetleri ölçebilir. Uygun fiyat, kolay numune hazırlama ve işletme, özellikle nanometreye kadar yüksek çözünürlük bu yöntemin avantajlarıdır. . Ayrıca, seramik malzemenin yüzeyi veya metalik nano partiküllerin ya da çok yumuşak polimerlerin, çok esnek polimerlerin, insan hücresinin ve DNA'nın dağılması gibi hemen hemen her tür numuneyi görüntüleyebilme yeteneği, AFM'nin en önemli avantajlarıdır.

Manyetik Kuvvet Mikroskobu (MFM), bu tezin amacı olan manyetik özelliklerin yüzey araştırması için başka bir standart yöntemdir. MFM, 10 nm ve daha düşük manyetik çözünürlüğe sahip malzeme bilimi alanındaki önemli rollerden biridir;

spintronics, spin cam sistemi, manyetik nanopartiküller, süper iletkenlik, yüksek yoğunluklu manyetik kayıt ortamı, manyetik faz gibi farklı bilim alanlarında kritik bilgiler sağlar. geçiş, vb. AFM / MFM'nin 300 kelvin ila yüzlerce millikelvin düşük sıcaklık aralığında çalışma kabiliyeti mikroskobun çok yönlülüğünü arttırır.

Prensip olarak, düşük sıcaklıkta Atomik / Manyetik Kuvvet Mikroskobu (LT-AFM / MFM), konsol sapmalarının ölçülmesi ile çalışmaktadır; Bu, lazer ışığını bir fiber kablo ile konsol ucuna yönlendiren fiber interferometresinin, sapmadan geri dönen lazer ışığının yüzdesini hesaplayarak sapmayı ölçebileceği anlamına gelir. Buradaki önemli rol, mikroskobun daha fazla malzeme değerlendirmesi için son derece düşük sıcaklıklarda çalışması ve aynı zamanda çeşitli sıcaklıklarda uygun şekilde çalışmanın güvenilirliğidir.

Kritik sorun, konsol ve elyafın sırasıyla soğutma durumunda çökebileceği mikroskop dizilimidir. Bu nedenle, mikroskop kafasının tasarımı tamamen merkezli olmalı ve malzemenin farklı termal büzülmesini göz önünde bulundurarak belirli bir mekanizma aynı hizada olmalıdır. Ayrıca, çoğu kriyojenik sistem numune alanında sınırlıdır; sonuç olarak, bu sınırlama tüm tasarım ve sistem uyumunda uygulanmalıdır.

Yüksek lisans tezimde Düşük Sıcaklıkta Fabry-Perot Atomik Kuvvet Mikroskobu / Manyetik Kuvvet Mikroskobu (LT-AFM / MFM) geliştirdim. Bu cihaz grubumuzda daha önce geliştirildi ve konsol sapmasını ölçmek için standart uçlar ve bir Fabry-Perot fiber interferometre kullanıldı. Bu LT-AFM'nin önceki versiyonunda düşük sıcaklıklarda fiber nanopozlayıcı ile bazı güvenilirlik sorunları vardı. Prensip olarak, bir Fabry-Perot AFM / MFM'de, ikincisini hareket ettirerek konsol ile fiber arasındaki mesafeyi azaltmak gerekir. Bu sorun aynı zamanda çözünürlüğü iyileştirmek için gerekli bir araçtır, çünkü yansıyan ışığın sinyal yoğunluğu artabilir. Önceki kurulumda, piezo nanopozlayıcı, kriyostattaki düşey doğrultuda sınırlı alan nedeniyle elyafı tutan yüksüğü hareket ettiremedi. Bu nedenle, tasarımı değiştirdim, böylece elyaf nanopozitörünün güvenilirliğini arttırdım. Bu, (1) piez tüpünde AFM ucunun

merkezlenmesi; (2) yüksük kaydığı yivlerin yüzey kalitesini iyileştirmek; (3) elyaf tutucunun atalet kütlesinin arttırılması.

Yeni eşmerkezli tasarım, piezoelektrik nanopozitifin sadece fiberi dikey yönde ileri ve geri hareket ettirmekle kalmayıp, aynı zamanda 300 miliKelvin'e kadar olan aşırı düşük sıcaklıklarda da güvenilir ve hassas bir şekilde çalıştı. Elyafın konsoluna göre konumunu optimize etme hareketi mikroskobun performansı için önemlidir. Böylece eğim, yani, fotodiyottaki sinyalin, konsol pozisyonunun, yansıyan lazer sinyalinin değişmesine ve dolayısıyla AFM'nin dikey çözünürlüğüne bağlı olarak değişmesi ile artar. Bu yeni tasarımla, 3.5 mW'lık bir lazer gücü kullanılarak 148 (mV / Å) eğime ulaşılırken, eğimden önce sadece 120 (mV / Å) değerindeydi. Bu eğimi arttırmak, AFM ve MFM'de de dikey çözünürlüğün artması demektir.

Bu araştırmada, daha önce geliştirilen AFM / MFM Fabry-Perot düşük sıcaklık mikroskobunu, 25,4 mm'den daha düşük bir dış boyutu olan, farklı üreticilerden veya sıvı He banyolarından gelen çeşitli kriyojen içermeyen kriyolar için tamamen ticarileştirilmiş şekilde geliştirdik. Yeni kurulan kriyojensiz kriyostatta yapılan ve tüm ölçümler Kriyognetik cihazdan 1,3 K değerine ulaşabilir; Bu ultra düşük sıcaklık, malzeme biliminde hayati bir konudur ve aynı zamanda birçok fenomen üzerinde fizik araştırması yapar. Mikroskopun hem AFM hem de MFM modunda çeşitli sıcaklıklarda çalışma potansiyeli, 300 K'da 25 fm / $Hz^{1/2}$ ve 1 K'da 12 fm / $Hz^{1/2}$ civarında ultra düşük gürültü seviyesi yüksek çözünürlüklü görüntüler verir.

Anahtar Kelimeler: Atomik kuvvet mikroskobu, AFM, manyetik kuvvet mikroskobu, MFM, düşük sıcaklık, manyetik alan, yüksek çözünürlüklü görüntüleme, kriyostat, milliKelvin, fiber interferometre, fiber Fabry-Pérot interferometre

ACKNOWLEDGEMENTS

I would like to thank TUBITAK for funding this work.

I would like to thanks Prof. Ahmet Oral for all his supports during my master's study and providing me a great chance to get trained, work and collaborate in the NanoMagnetics Instrument company. These three years were an opportunity to get in touch with expert people who help me to overcome problems as well as doing experiments with various microscopes.

I would like to thank Prof. Tofik Mamadov who helped me a lot in instruments installation.

I thank Muherram Demir, Hilal Gozler, Kazim Ayhan, Seda Surucu and all NanoMagnetics Instruments family for all their efforts and help to finish this project.

I would like to thank my lab mates and my friends Shayeste Moravati, Parisa Sharif, and Muammer Kozan, who helped me in my tough times.

And finally I do appreciate my family, specially my mother who always pushes me forward in all my level of my life.

TABLE OF CONTENTS

LIST OF TABLES

TABLES

LIST OF FIGURES

FIGURES

LIST OF ABBREVIATIONS

ABBREVIATIONS

AC	Alternating current
AFM	Atomic Force Microscope
Co	Co
CoPt	Cobalt platinum
DC	Direct current
DOS	Density of states
DR	Dilution refrigerator
EFM	Electrostatic Force Microscope
Fe	Iron
FFPI	Fiber Fabry-Pérot interferometer
FWHM	Full Width Half Maximum
FMR	Frequency Modulation Reflective coating
GB	Gigabit
GBP	Gain bandwidth product
Gbpsi	Giga bit per square inch
HF	Hydrofluoric acid
HOPG	Highly Ordered Pyrolytic Graphite
^{3}He	Helium three
ID	Inner diameter
IR	Infrared
ITO	Indium tin oxide
I-V	Current to voltage
IVC	Inner vacuum jacket
K	Kelvin
kHz	Kilo Hertz
LT	Low Temperature
LT-AFM/MFM	Low Temperature Atomic Force Microscope/Magnetic Force Microscope
MFM	Magnetic Force Microscope
MFMR	Magnetic Force Microscopy Reflective coating
MHz	Mega Hertz
mK	milliKelvin
mbar	milibar
NA	Numerical aperture
nm	Nanometer
Ni	Nickel

OD	Outside diameter
PCB	Printed circuit board
PD	Photodetector
PhBr	Phosphor bronze
PID	Proportional Integral Derivative
PLL	Phase Lock Loop
SHPM	Scanning Hall Probe Microscopy
SPM	Scanning Probe Microscope
ss	Stainless steel
STM	Scanning Tunneling Microscope
SHO	Simple harmonic oscillator
TL	Top loading
VTI	Variable temperature insert
V_PD	Signal photodiode voltage

LIST OF SYMBOLS

SYMBOLS

Symbols	
A	Amplitude
A_0	The amplitude at the resonance frequency
Å	Angstrom
$Å_{pp}$	Angstrom peak to peak
B_W	Bandwidth
C	Speed of light
D	The outside diameter of the piezo tube
d	Fiber-cantilever separation
d_{31}	Transverse piezoelectric coefficient
E	Magneto static energy
e	Charge ($1.6x10^{-19}$ C)
ε	Thermal conductivity coefficient
emu	Electromagnetic unit
F	Force
F_{ts}	Tip-sample interaction force
$F_d(t)$	Driving force
f_0	Resonance frequency
fm	Femtometer
$\vec{H}$	Magnetic stray field
H_c	Critical field density
h	Planck constant ($6.63x10^{-34}$ J.s)
i	Photocurrent
i_shot	Shot noise current
i_0	Midpoint photocurrent
J_c	Critical current density
k	Spring constant
k_B	Boltzmann constant ($1.38x10^{-23}$ J/K)
kx	Piezo coefficient in the x-axis
ky	Piezo coefficient in the y-axis
Kz	Piezo coefficient in the z-axis
L	Length
$\vec{M}$	Magnetization
N_{Total_rms}	Summation of noises
m	Mass
m	Interference slope
ms	Millisecond
$\vec{m}$	Magnetic moment
μ	Micro

μ_0	Permeability of free space (4π x10^{-7}H)
N	Newton
n	Refractive index
n_{rms}	Average mean square value of noise
n_m	Number of moles
n_p	Number of photons
nF	Nano Farad
ns	Nanosecond
Oe	Oersted
P	Optic power
p	Pico
P_{RP}	The momentum of the light
Q	Q-Factor
Q_{Total}	Total heat
θ	Half angle of the maximum cone of the light
R	Reflectivity
R_F	Feedback resistor
R_{number}	Thermal conductivity
S	Spectral noise density
s	Wall thickness of tube piezo
S_{PD}	The responsivity of the photodetector
T	Temperature
T	Tesla
T_F	Fermi temperature
t	Time
U	Applied voltage to the electrodes
z	Position
Δx	Lateral piezo displacement
Δz	Displacement
Δf	Frequency shift
ΔA	Amplitude shift
$\Delta \emptyset$	Phase shift
Δl	Length change
ΔT	Temperature difference
∇	Gradient
λ	Wavelength
α	Thermal contraction coefficient
β	Fabry-Pérot slope coefficient
τ	Optical path difference of the cavity gap
z_0	initial position, equilibrium position
$<z^2>$	Mean square amplitude of the cantilever
δF'	A derivative of the force
$\frac{\partial z}{\partial t}$	A derivative of position with respect to time

$\frac{\partial V}{\partial z}$	A derivative of potential energy with respect to the position
δ	Damping factor
Ø	Phase
V(z)	Potential
V	Visibility
$\bar{v}$	Voltage noise
v_shot	*shot* Shot noise voltage
ω	Angular frequency
W	Watt
Ω	Ohm
AC	Alternating current
AFM	Atomic Force Microscope
Co	Cobalt
CoPt	Cobalt platinum
DC	Direct current
DOS	Density of states
DR	Dilution refrigerator
EFM	Electrostatic Force Microscope
EI	Experimental insert
Fe	Iron
FFPI	Fibre Fabry-Pérot interferometer
FWHM	Full-Width Half Maximum
FMR	Frequency Modulation Reflective coating
GB	Gigabit
GBP	Gain bandwidth product
Gbpsi	Gigabit per square inch
HF	Hydrofluoric acid
HOPG	Highly Ordered Pyrolytic Graphite
^{3}He	Helium three
ID	Inner diameter
IR	Infrared
I-V	Current to voltage
IVC	Inner vacuum jacket
K	Kelvin
kHz	Kilo Hertz
LT	Low Temperature
LT-FM/MFM	Low-Temperature Atomic Force Microscope/Magnetic Force Microscope
MFM	Magnetic Force Microscope
MFMR	Magnetic Force Microscopy Reflective coating
MHz	MegaHertz
mK	milliKelvin
mbar	millibar
NA	Numerical aperture
nm	Nanometer

Ni	Nickel
OD	Outside diameter
PCB	Printed circuit board
PD	Photodetector
PhBr	Phosphor bronze
PID	Proportional Integral Derivative
PLL	Phase Lock Loop
PrFM	Piezoresponse Force Microscopy
RF	Radiofrequency
SHPM	Scanning Hall Probe Microscopy
SNR	Signal to noise ratio
SPM	Scanning Probe Microscope
ss	Stainless steel
SSS	Super Sharp Silicon
STM	Scanning Tunneling Microscope
SHO	Simple harmonic oscillator
TL	Top loading
VCO	Voltage Controlled Oscillator
VTI	Variable temperature insert
V_PD	Signal photodiode voltage

CHAPTER 1

INTRODUCTION

1.1. Introduction and Overview

Atomic force microscopy (AFM), an innovative method that enables to map the structures of the surface with fabulous resolution and precision. Images with a high resolution of single atoms arrangement on the surface of a sample or the formations of individual molecules are the fascinating capability of this microscopy method. Imaging in a cryogenic temperature with an ultra-high vacuum provides the possibility to measure a sample's surface properties with an atomic resolution [1]. Besides, not necessarily AFM needs to be operated under this extreme condition; it can be performed in the physiological buffers at 37 C to map biological reactions in real-time [2-4]. Different kinds of samples like the surface of ceramic materials such as a very hard one or distribution of metallic nanoparticles as well as very soft, like cells of the human body, very flexible polymers, or DNA fragments could be carried out by the AFM. The great advantages of this imaging method made it such a versatile application since the 1980s which has employed to be utilized in all experimental science areas like chemistry, physics, biology, material and nanotechnology science, medicine, and etc. These days AFM is the most reliable technique to deliver highly quantitative images with ultra-high resolution in the industrial, academic, and also government labs.

An AFM microscope is rather varied from other microscopes which are operating with light or electron focusing on a surface such as an optical or electron microscope. The AFM is an almost mechanical technique and touches the material surface with a very sharp probe, that maps the features as well as the height of the surface, in other words, it projects the sample surface in three dimensions. The data provided by an AFM must

be analyzed by the software to generate the topography image, also analysis possibly helps to remove artifacts from the surface of the image as well.

The first AFM (Figure 1.1) was a stylus profiler including a lever with optical properties that could observe the movement of the lever with a tip at the end and a small bar that was dragged through the surface of the sample and mapped the surface topography. The common problem of this method was the probability of lever bending due to the horizontal force made by surface large features. Becker presented this problem [5] in 1950 and proposed to oscillate the lever in the initial state. The vibration method somehow prevents the lever from bending, collapsing to the surface, and damaging the sample.

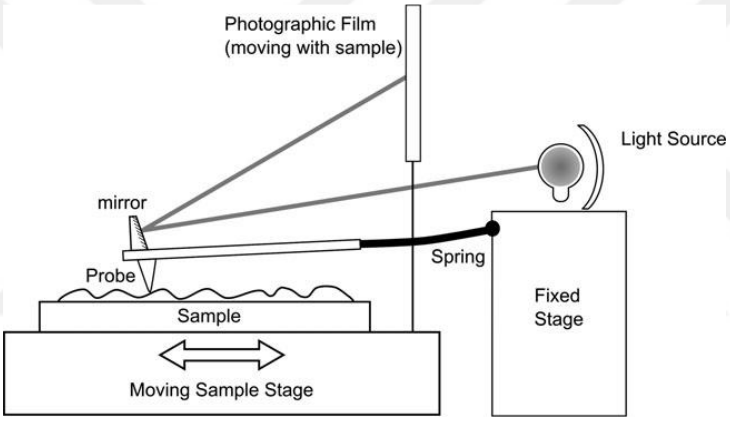

Figure 1. 1Earliest design of the AFM with an optical lever in the 1920s. [6]

In 1971, the non-contact type of scanning probe microscopy was claimed by Russell Young which made of a sharp metal probe and works with the electron field emission current principal [7] in between the metal probe and the sample surface. He mounted the sharp tip on the piezoelectric ceramic elements to move the Z direction. Monitoring the probe motion in three directions (X, Y, and Z) provides the 3-dimensional image of the sample surface.

In 1981 [8-10] Binnig and Rohrer tried to improve this method and apply the vibration isolation. In such a way, it was possible to observe the tunneling of the electron rather

than electron emission among the tip and sample. This method was the first generation of scanning tunneling microscopy (STM).

STM is able to measure individual atoms or molecules as well as measuring the local density of state (DOS) [11]. Figure 1.2 depicts an explanation of the STM method. By applying a bias voltage to a conductive sample and a very sharp metallic tip which basically has one atom at the apex of the tip, the tunneling current can be felt. The tunneling current explicitly depends on the distance of the tip-sample with an exponential factor.

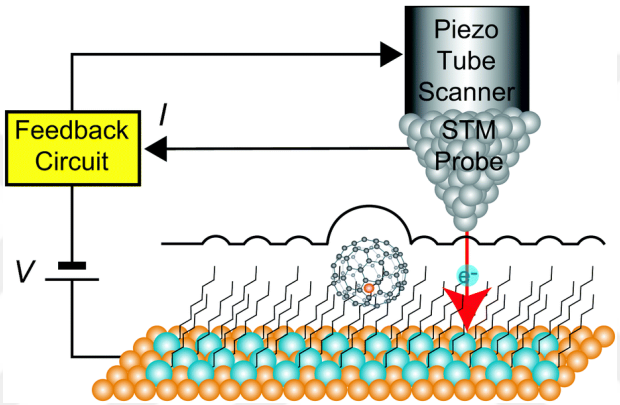

Figure 1. 2 schematic of scanning tunneling microscopy. [12]

The tip-sample distance here is the main factor in controlling the microscope sensitivity; technically, the probability of electron tunneling strongly depends on this factor and is much more sensitive than the electron emission. Binnig and Rohrer applied the isolation vibration by floating all instrument magnetically, then the result of the early experiments was so startling; the single atoms of the silicon on a surface were recorded [13-14]. Finally, this incredible innovation was awarded the Nobel Prize in physics in 1986. Although STM reveals the new technique in the scanning probe microscope, it has a limitation to work only on electrically conductive samples.

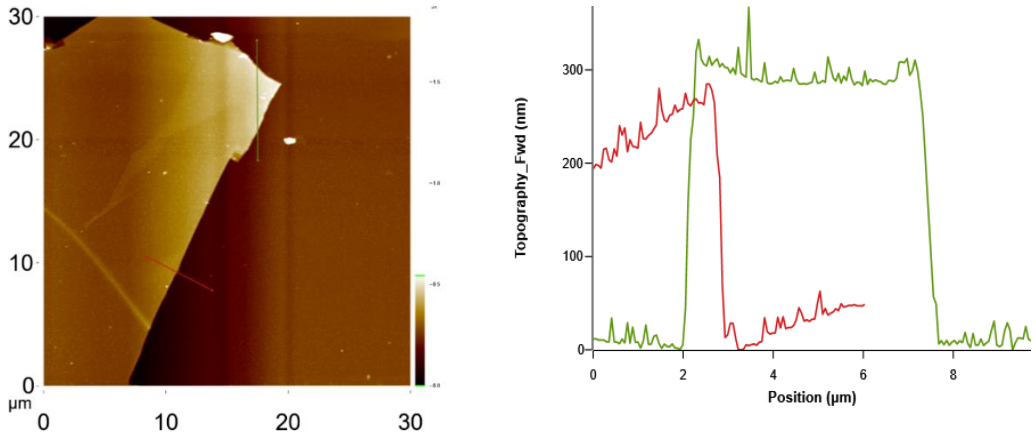

(a) (b)

Figure 1. 3 STM image, (a) Topography, (b) Size of the Graphite on the HOPG.

The invention of the AFM provides an opportunity not only to image conductive samples but also image isolating samples. In AFM, distance dependency of the sample and the tip plays a vital role in dominating either repulsive and attractive force interaction. In AFM contact mode, the probe touches the sample surface and maps the surface in the repulsive force regime. In the contact mode, the periodicity [15] and lateral friction force [16] could be studied. By increasing the tip-sample distance, the role of an attractive force is so essential, and in which the tip does not touches the surface and in any contact with the surface of the sample, we can call AFM non-contact mode [17]. Tapping mode or semi-contact mode [18] or phase image mode [19] AFM works in both attractive and repulsive force regime, which is the commonly used mode these days. The capability of measuring Magnetic, Electrostatic, friction, or Van der Wall forces besides imaging the sample surface by utilizing the specific tips are the advantages of AFM. These forces could be measured when the specific tip is manufactured; for instance, for measuring the magnetic features of the material, the tip should be coated by magnetic materials. This technique is named magnetic force microscopy (MFM). Technically, the method's name obtained by the force name which is measured in AFM.

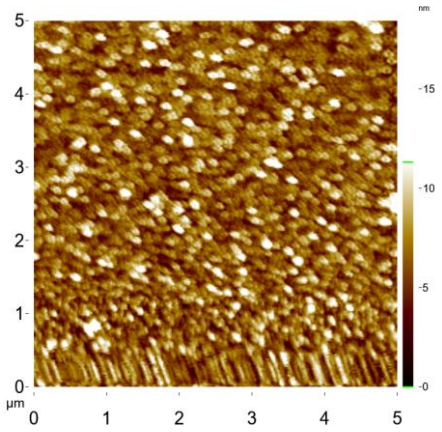

Figure 1. 4 AFM image of the 200 nm Nickle Oxide coated on the glass

Magnetic force microscopy is one of the essential measurements in exposing the magnetic properties of the material [20]. Moreover, this technique is comparatively easy and typical like AFM measurement, which is performed in a variety of environments like the large magnetic field [21], vacuum, low temperature and so on. Magnetic imaging in different temperatures and the high magnetic field has a significant role in vortex imaging or manipulation of vortices [22-29] in superconductors, domain wall in ferromagnetic thin films [30-31], magnetic phase separation [32-33], topological isolators [34].

Low-temperature AFM and MFM (LT-AFM/MFM) measurements have limitations such as small spaces, approximately a few centimeters, inside the cryostats; hence there is a limited description in the literature [35-36] specifically temperatures below the 4K. Measuring the cantilever deflection is relatively hard and fiber interferometer [37-39] is the logical and reliable method for this sort of measurements. Here the cantilever should be aligned entirely concerning the fiber due to a thermal contraction in the low temperature.

1.2. Work Plan

In the aforementioned thesis, the ultra-low noise, self-aligned low-temperature Fabry-Perot AFM/MFM which is working based on fiber interferometer and temperature range of 1.3 K to 300 K was redesigned and developed. In this type of microscope,

there is no need for optical alignment between the fiber and cantilever. Obtaining the graphene single layer image represents the capability of reaching a high resolution. Technically, we used Nanosensor alignment chip [60] to perform the alignment-free system and very simplistic to operate. The design of the mechanical parts in LT Fabry-Perot AFM/MFM was precisely engineered and tried to minimize the thermal contraction of the material, and suitable for different temperature ranges. In the design of the microscope, we attempted to eliminate all the unnecessary positioning procedure mechanism to eliminate the complication as well as utilizing as less mass as possible in order to make the microscope suitable for limited space inside the cryostat and cooling the system with less power.

The principals and the theory of atomic force microscopy and magnetic force microscopy operation are described in chapter 2. In chapter 3, LT Fabry-Perot AFM/MFM instrumentation and a new design with all modification and operation principles are described.

In chapter 4, the experiments at the low temperature and noise sources and measurements are explained. And finally, AFM and MFM images are presented. The Mika single layer at the low temperature presents the high functionality of the microscope.

Chapter 5 is a description of the low-temperature dry cryostat which is newly installed in our lab with the capability of working in 1.3 K. Moreover, an isolation vibration platform is designed to decrease the noise. The value of noise in both on and off status of isolation platform is measured and incredibly we were able to image the single-layer graphene while microscope inside the cryostat and pulse tube cold head working.

In chapter 6, the Fabry-Perot interferometry principle is described as well as the modified mechanism of fiber movement to reach the Fabry- Perot basics and increase the resolution based on increasing the laser power gain. And at the end, this mechanism is tested at low temperature and the reliability of working in various temperature ranges is proved.

CHAPTER 2

MAGNETIC FORCE MICROSCOPY

2.1. Magnetic Force Microscopy (MFM)

MFM is one of the AFM sub-branches with the potential of measuring magnetic features of the sample which is soon realized in AFM history [40-42]. In MFM measurements, it is so significant that the probe stays in very close distance to the surface as magnetic stray field decays promptly with the distance factor. To obtain the magnetic image, the probe should be magnetically coated to feel the distribution of direct magnetic stray field above the surface. Typically, the probe consists of same AFM silicon cantilever which is coated by a thin layer of magnetic material. The typical materials which could be utilized for MFM cantilever are cobalt, cobalt-nickel and cobalt -chromium [43]. Coating the cantilever due to magnetization brings detrimental effects, firstly increasing the tip radius which decreases the resolution, secondly increasing the wear rate as these materials are softer than the silicon itself. Normally, on the sample surface, magnetic forces are being measured in certain distance respect to the surface (of the order of approximately a few to a few hundreds of nm). There are also some techniques to measure magnetic forces which particularly have pros and cons. In "lifting"-type methods, firstly the topography is measured and in the following by raising up in a certain amount, the cantilever can feel and measure the magnetic forces.

One method is mapping the surface topography and then set a z set point to raise the tip and collect the magnetic image. This method works in a flat surface and possibly the thermal drift effects the MFM image (Figure 2.1).

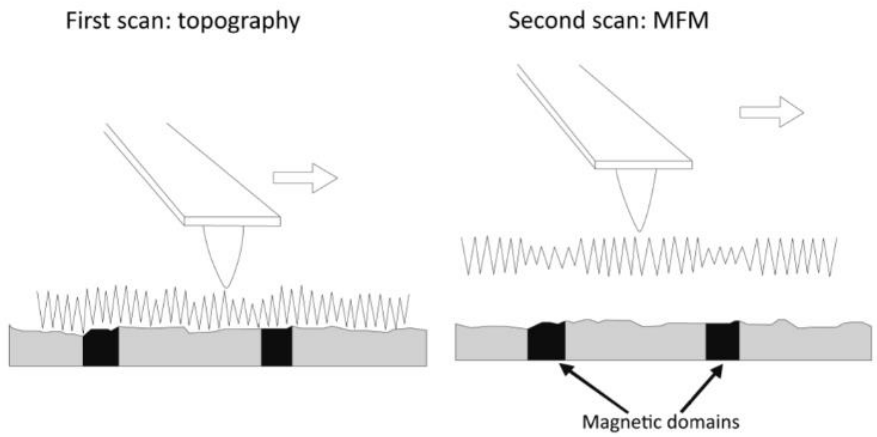

Figure 2. 1 lifting the tip of the surface. [6]

Bard [44] mentioned an improved method, which firstly records the sample surface topography, then by lifting the probe in a certain height and following the same topography collects the MFM image (Figure 2.2). In this method, the probe scans a surface in the forward and backward lines. In the forward scan, topography image is collected, then in the backward line with a fixed lift, MFM image is being measured.

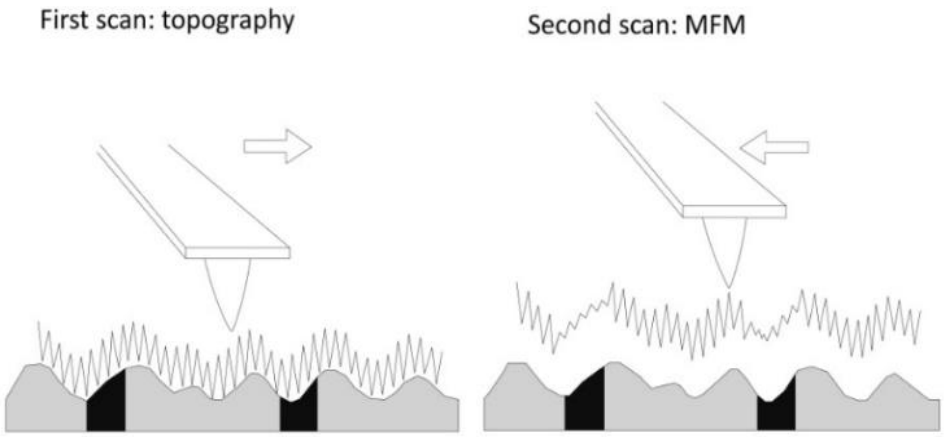

Figure 2. 2 schematic descriptions of the Bard method. [6]

In the other method, the probe changes the height in the Z direction during the scan, in the other word, it will be continually shifting toward the sample to check the topography and away to see the magnetic field (Figure 2.3).

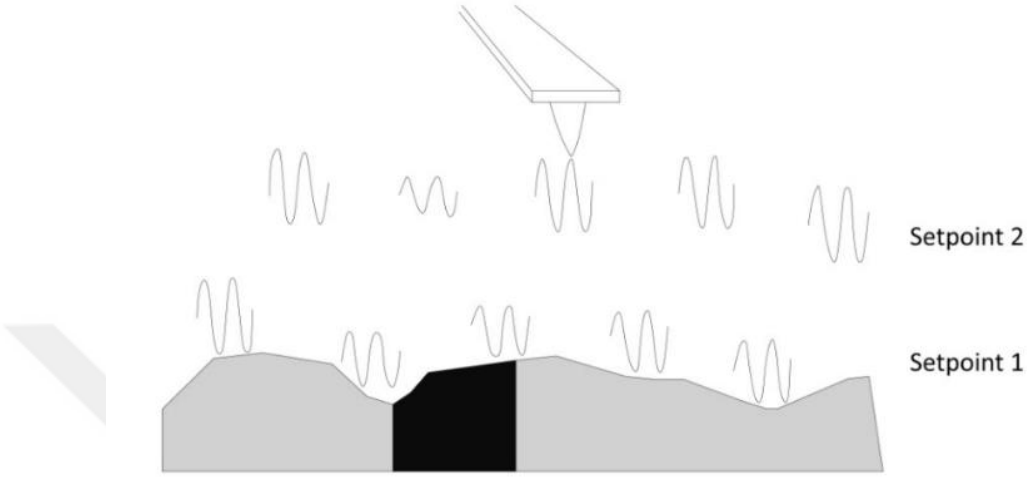

Figure 2. 3 z set-point oscillation. [6]

Finally, according to Hosaka's description [45] at every pixel, the tip is raised above the sample surface to record the magnetic field in various heights then it moves to the next side points, lifted again and repeats. Although this method is slow, it can reduce thermal drift effects (Figure 2.4).

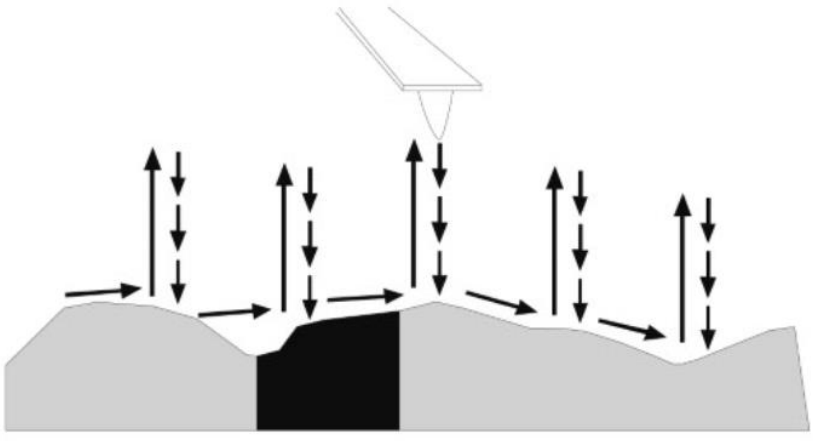

Figure 2. 4Schematic descriptions of the Hosaka method. [6]

Typically, the MFM measurements are conducted in one of these dynamic modes and the phase images expose the magnetic effects.

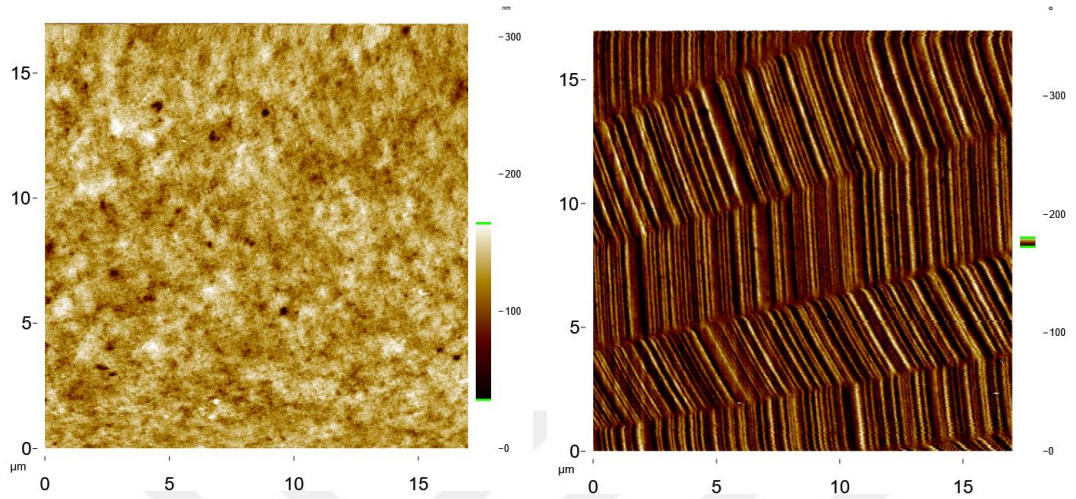

Figure 2. 5 MFM image of the Sony hi8 tape which is conducted in 300K. Topography (a) image is recorded by a forward scan and backward is used to record the magnetic image (b).

2.1.1. Applicability

Magnetic force microscopes are of prime importance in scientific and industrial fields. Particularly, the data storage industry relays on this accurate technique to investigate the magnetic nanodomains of the hundred nanometers size range [46-47]. Study of magnetic nanoparticles is the other tense interest within the scientific society which MFM has a great use [48].

2.2. Operation Theory

AFM imaging measurement is operated in different ways which can be listed in two parts: Static mode and Dynamic mode. The Dynamic mode itself divided in two: semi-contact mode (which is called tapping mode) and non-contact mode.

2.2.1. Dynamic Mode

The cantilever in the dynamic mode is oscillating at its own resonance frequency with utilizing a Piezo actuator. This motion can be modeled resemblance to a simple

harmonic oscillator in a spring-mass system (Figure 2.6) and solved by Newton's 2nd low of motion.

$$F = ma = m\frac{\partial^2 z}{\partial t^2} = -k(z - z_0) \tag{2.1}$$

$$m\frac{\partial^2 z}{\partial t^2} + k(z - z_0) = 0 \tag{2.2}$$

$$f_0 \equiv \sqrt{\frac{k}{m}} \tag{2.3}$$

Respectively k, m, and f_0 are cantilever spring constant, mass, and natural resonance frequency. In the absence of the force field, z_0 is the cantilever position, and z is distance among the sample surface and the cantilever apex.

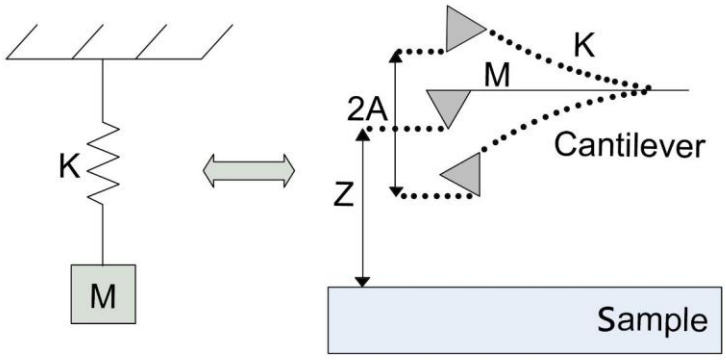

Figure 2. 6 The schematic resemblance of a spring-mass system and cantilever. [49]

Including the friction force, the oscillatory system can be described by a damped harmonic oscillator:

$$m\frac{\partial^2 z}{\partial t^2} + \delta\frac{\partial z}{\partial t} + k(z - z_0) = 0 \tag{2.4}$$

$$\delta = \frac{k}{f_0 Q} \tag{2.5}$$

Where δ is damping factor and Q is the quality factor.

In the presence of a driving force provided by Piezo actuator:

$$F_d(t) = F_0 \cos \omega t \tag{2.6}$$

$$\Rightarrow m\frac{\partial^2 z}{\partial t^2} + \delta\frac{\partial z}{\partial t} + k(z - z_0) = F_d(t) \tag{2.7}$$

By including the tip-sample interaction the equation would be:

$$\Rightarrow m\frac{\partial^2 z}{\partial t^2} + \delta\frac{\partial z}{\partial t} + k(z - z_0) = F_d(t) + F_{ts}(z) \tag{2.8}$$

The tip-sample term makes non-linearity in the equation. Therefore, $F_{ts}(z)$ should be expanded by a Taylor series:

$$F_{ts}(z) = F_{ts}(z_0) + \frac{\partial F_{ts}(z_0)}{\partial z}(z - z_0) \tag{2.9}$$

Approximately, F_{ts} is equal in these two terms with enough oscillation amplitude and small interaction force.

$$m\frac{\partial^2 z}{\partial t^2} + \delta\frac{\partial z}{\partial t} + k(z - z_0) = F_d(t) + F_{ts}(z_0) + \frac{\partial F_{ts}}{\partial z}|_{z=z_0}(z - z_0) \tag{2.1}$$

$$\Rightarrow m\frac{\partial^2 z}{\partial t^2} + \delta\frac{\partial z}{\partial t} + [k - \frac{\partial F_{ts}}{\partial z}|_{z=z_0}](z - z_0) = F_d(t) + F_{ts}(z_0) \tag{2.2}$$

The term $k - \frac{\partial F_{ts}}{\partial z}$ is called effective spring constant, k_{eff}.

The above differential equation solution can be written as:

$$z(t) = z_0 + A\cos(2\pi f_d t - \emptyset) \tag{2.3}$$

And

$$f_d = \sqrt{\frac{k}{m} - \frac{1}{m}\frac{\partial F_{ts}}{\partial z}} \tag{2.4}$$

$$A = \frac{A_0/m}{\sqrt{\left({f_0}^2 - f_d^2\right)^2 + \left(\frac{f_0 f_d}{Q}\right)^2}} \tag{2.5}$$

$$\emptyset = \frac{{f_0}^2 - f_d^2}{\sqrt{\left({f_0}^2 - f_d^2\right)^2 + \left(\frac{f_0 f_d}{Q}\right)^2}} \tag{2.6}$$

In the cantilever resonance frequency, Phase and Amplitude would be:

$$A_0 = \frac{F_0 Q}{m{f_0}^2} \tag{2.16}$$

$$\emptyset_0 = \frac{\pi}{2} \tag{2.17}$$

If we assume k>>$\partial F_{ts}/\partial z$ and $\sqrt{1-x} = 1 - x/2$ the Eq 2.14 would be:

$$\Delta f \approx \frac{f_0}{2k}\frac{\partial F_{ts}}{\partial z} \tag{2.18}$$

In fact, in the force field present, the resonance frequency of the cantilever would change and the gradient of the force could be calculated with measuring the amount of this shift, or by measuring the Amplitude change (ΔA) as well as the phase change ($\Delta\emptyset$) (Figure 2.7) when oscillation frequency is kept constant.

$$\Delta A = -\frac{2A_0 Q}{3\sqrt{3}k}\frac{\partial F_{ts}}{\partial z} \tag{2.19}$$

$$\Delta\emptyset = \frac{Q}{k}\frac{\partial F_{ts}}{\partial z} \tag{2.20}$$

In the dynamic mode of our system, the excitation frequency and oscillation amplitude are kept constant. Changing the scanner piezo tube length helps to keep the amplitude constant, and finally, the topography image is measured by the piezo tube length change.

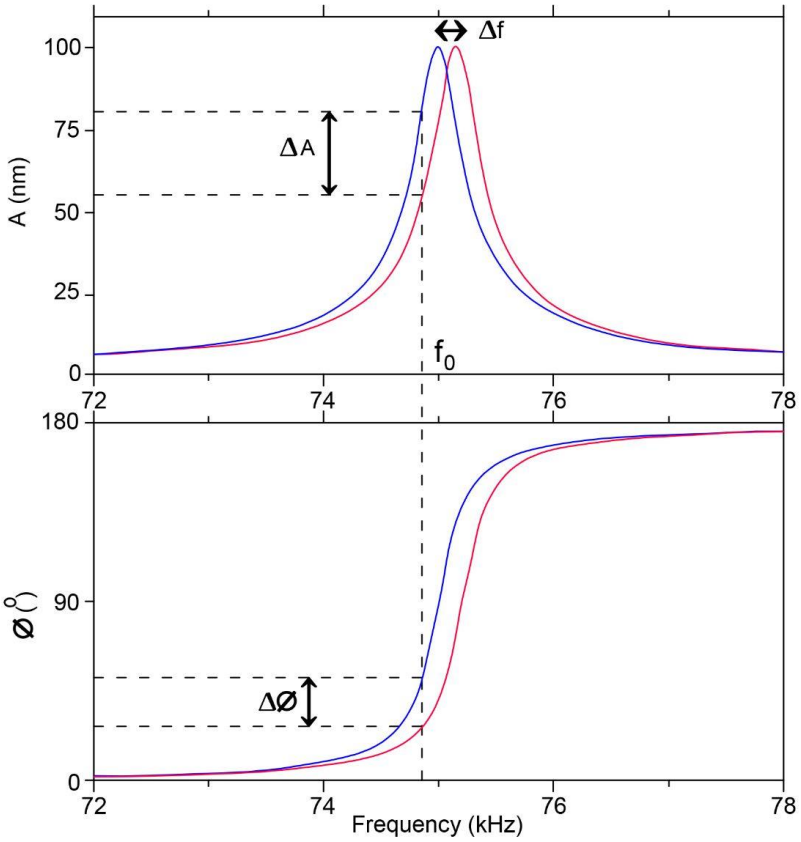

Figure 2. 7 The oscillation amplitude and phase versus frequency. The blue line indicates cantilever oscillation amplitude in the free status and the red line is in the condition which cantilever is brought to the surface and there is the force field interaction. The first plot shows the amplitude which is decreased by ΔA and the second plot corresponds to the phase shift $\Delta\emptyset$. [49]

2.2.2. Static Mode

Almost the probe is like a spring which in interaction with the surface could be bend. This force is explained by Hook's low.

$$\Delta Z = \frac{F_{ts}}{k} \tag{2.27}$$

Here ΔZ is the amount of the displacement, k is the cantilever spring constant and F_{ts} is the sample-cantilever interaction force. By measuring the cantilever deflection, accordingly, the force could be calculated. This method is not suitable for MFM measurements. In this mode, the cantilever always is in contact with the surface in contact with the sample surface and its sensitivity is poor.

2.2.3. Tip-Sample Magnetic Interaction

As it previously discussed MFM measurements is conducted between a magnetic sample and a magnetic cantilever, therefore, the total magnetostatics energy would be:

$$E = -\frac{\mu_0}{2}\left[\int \vec{M}_{tip}\vec{H}_{Sample}dV + \int \vec{H}_{tip}\vec{M}_{Sample}dV\right] \quad (2.22)$$

$$\vec{m} = \int \vec{M}\, dV \quad (2.23)$$

Where H is a stray field, M magnetization, m magnetic moment, and μ_0 Permeability of free space.

As the two integrals are equal, the energy equation would be:

$$E = -\mu_0\left[\int \vec{M}_{tip}\vec{H}_{Sample}dV\right] \quad (2.24)$$

Over the surface scan, the cantilever displaces only in the vertical direction, hence, we need to consider the vertical magnetic component of the force.

$$F_{ts}(z) = -\nabla \mathrm{E} = \mu_0 \int_{V_{tip}} \nabla(\vec{M}_{tip}\vec{H}_{Sample})dV_{tip} \quad (2.25)$$

$$F_{ts}(z) = \mu_0 \int_{V_{tip}} \vec{M}_{tip}\frac{\partial \vec{H}_{Sample}}{\partial z}dV_{tip} \quad (2.26)$$

$$\frac{\partial F_{ts}}{\partial z} = \mu_0 \int_{V_{tip}} \vec{M}_{tip}\frac{\partial^2 \vec{H}_{Sample}}{\partial z^2}dV_{tip} \quad (2.27)$$

2.2.4. Lennard-Jones Potential

A couple of natural atoms or molecules interaction can be mathematically modeled by Lennard-Jones Potential. Here this method is employed in Tip-Sample interaction.

$$V_{LJ} = 4\varepsilon\left[\left(\frac{\sigma}{r}\right)^{12} - \left(\frac{\sigma}{r}\right)^{6}\right] = \varepsilon\left[\left(\frac{r_m}{r}\right)^{12} - 2\left(\frac{r_m}{r}\right)^{6}\right] \quad (2.28)$$

where r, σ, ε, and r_m are the distance between the particle, the finite distance at which the potential of inter-particle is zero, the potential well depth, and the distance which the potential reaches its minimum respectively. At the r_m the potential would be $-\varepsilon$. (Figure 2.8)

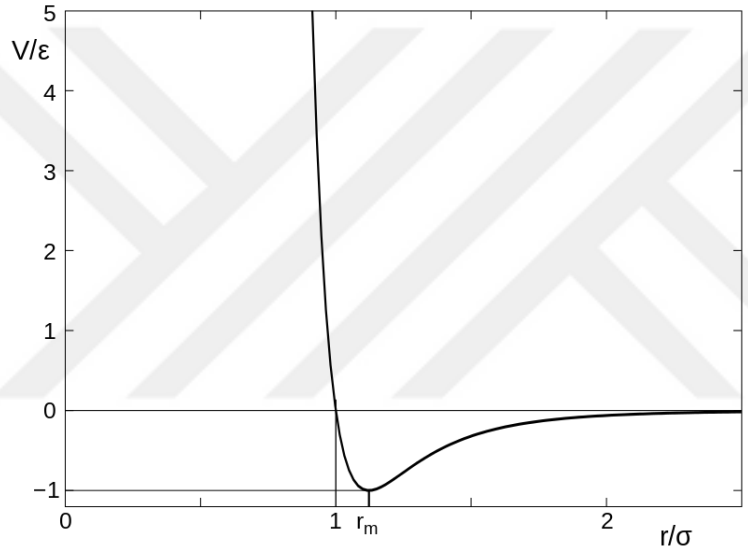

Figure 2. 8 Lennard-Jones potential, strength vs distance

The repulsive force term is defined by the term r^{-12} ; the Pauli repulsion when electron orbitals overlap in the short, and attractive long-term range is defined with the term r^{-6} to depict long term attractions like dispersion or Van der Waals force. [49]

The form which is simplified for software simulations is:

$$V_{LJ} = \frac{A}{r^{12}} - \frac{B}{r^{6}} \quad (2.29)$$

Where $A = 4\varepsilon\sigma^{12}$ and B= $4\varepsilon\sigma^{6}$

In the tip-sample interaction, the r term is the same z in the vertical direction, coefficients A and B depends on the system. Consequently, the potential and the force turn to be:

$$V(z) = \frac{A}{z^{12}} - \frac{B}{z^{6}} \tag{2.30}$$

$$F(z) = -\frac{\partial v}{\partial z} = 12\frac{A}{z^{13}} - 6\frac{B}{z^{7}} \tag{2.31}$$

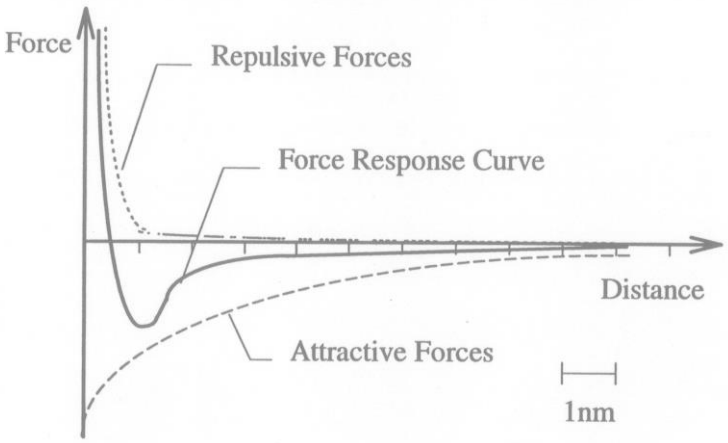

Figure 2. 9 The graph represents the attractive and repulsive regime in Lennard-Jones potential [50]

CHAPTER 3

MICROSCOPE INSTRUMENTATION

3.1. Microscope Instrumentation

3.1.1. Low-Temperature AFM/MFM Head

LT AFM/MFM is technically designed for extreme low-temperature operations like the millikelvin range. Therefore, the design should be considered according to the standard sample space of the cryostats from various vendors. And basically, cryostats sample space is around a few centimeters; hence, this limitation makes the head form with a 22.2 mm outer dimension (OD) and 100 mm length. Two centric Piezo employed for the main operation role: the inner piezo in order to scan the surface, and the outer piezo responsible for positioning the sample. The figure below shows the scanner piezo with 3" length that has the capability of operation in 4K with around 17 μm XY scan range and approximately 1.4 μm Z range. It is composed of the quadrant electrodes for XY and Z movement as well as a dither piezo on the top for oscillating the cantilever in dynamic modes. Sample Slider piezo is 1.5" long with the same quadrant and glass attached at the end. With the stick-slip method, the sample mounted on the sample holder (Puk) can be slid on the glass tube. The Puk itself is loaded on the glass and held with a leaf spring. The stick-slip motion has the capability to move the sample along the XYZ direction. Actually, this is the approach mechanism to reach the sample surface.

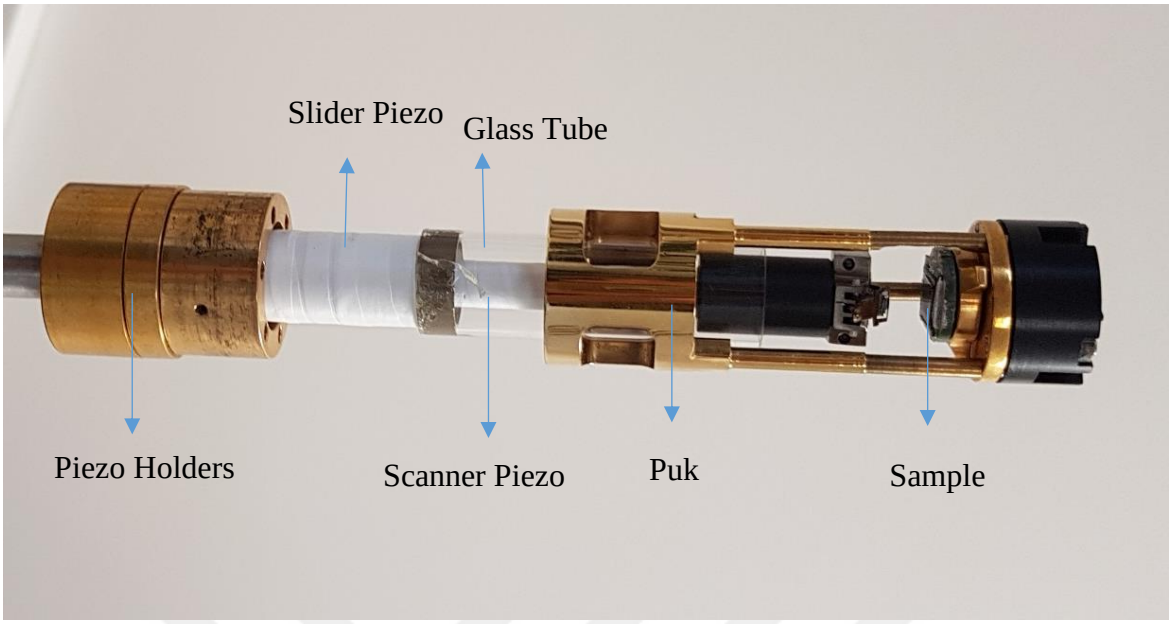

Figure 3. 1Low-Temperature Atomic/Magnetic Force microscope Head with the Puk and sample mounted.

3.1.2. LT-AFM/MFM head design optimization

The most crucial aspect here is the mechanism for aligning the fiber and cantilever as there is a particular danger of collisions during cooling due to thermal contraction. Here, a concentric design helps to prevent any failure. Furthermore, both the size and the thermal mass of the microscope head should be minimized to reduce the time required for cooling and to meet the rigorous space limitations inside the cryostat. Therefore, it is tried to reduce the thermal mass of the microscope head as much as possible. For instance, some pieces were made of plastic (Polyphenylene sulfide (PPS)) (Figure. 3.2, part 1). Furthermore, I increased the inertial mass of the brass weight (Figure. 3.2, part 3) that holds the zirconia tubing that acts as ferrule (Figure. 3.2, part 2) to improve the reliability of the Nanopositioner in the wide range of working temperatures from room temperature down to 1.3 K. Moreover, regarding the space limitations inside the cryostat, I have strived to design the microscope head to remain within 22.2 mm the outside diameter, and below 100 mm length to fit inside the 30 mm diameter standard helium cryostats. Thereby, our microscope head is compatible with various commercial cryostat designs.

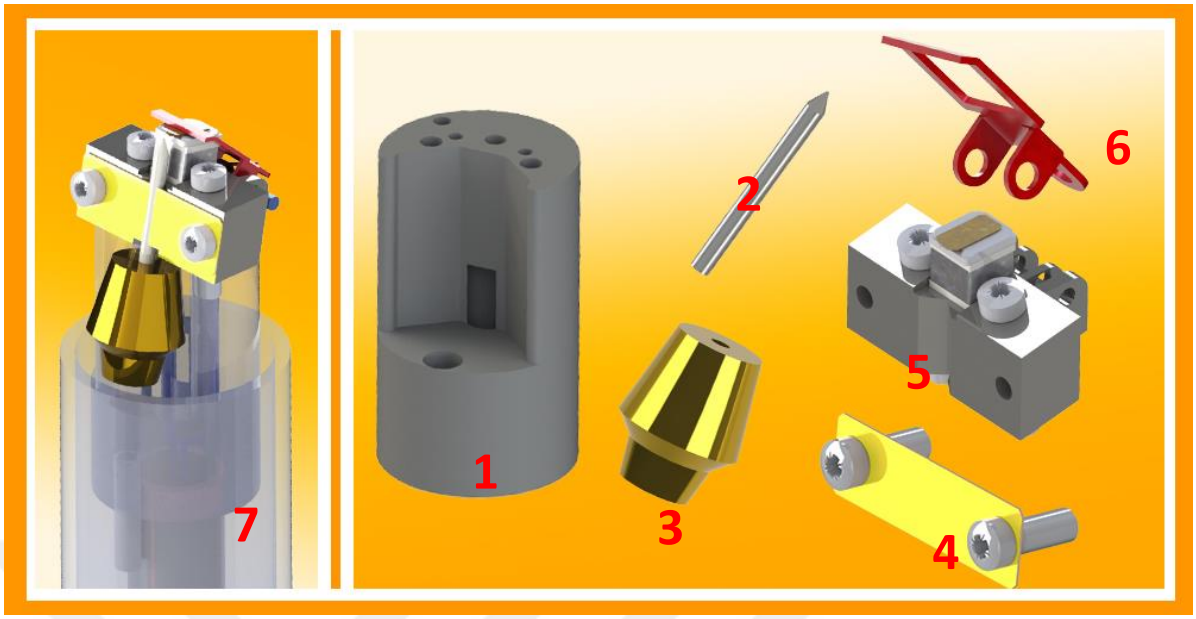

Figure 3. 2 1: holder, 2: zirconia tubing (ferrule) (0.050 g), 3: brass weight (1.5 g), 4: leaf spring to hold the tubing, 5: V-shaped MFM holder 6: leaf spring for the cantilever.

Technically all these designs are manufactured as a holder alignment and mounted on the top of the scanner piezo. Figure 3.2, part 7, shows the schematic design of all parts mounted together.

Therefore, the design is modified and results in improved reliability of the fiber Nanopositioner. This was achieved by (1) centering the AFM tip at the piezo tube; (2) improving the surface quality of the groves in which the ferrule is sliding; (3) increasing the inertial mass of the fiber holder.

3.1.3. Microscope Insert

The LT AFM/MFM is divided into two main part, the head and insert. The inset part is detachable from the docking part to the microscope head which provides the compatibility to various types of cryostats as well as using different heads like AFM, SHPM, STM, etc (Figure 3.3). The variable-length makes it possible to arrange the microscope in the center of the cryostat in order to adjust in the center of magnetic

field or cold part. The radiation shields applied on the stainless-steel insert length due to eliminating radiation originating from the environment.

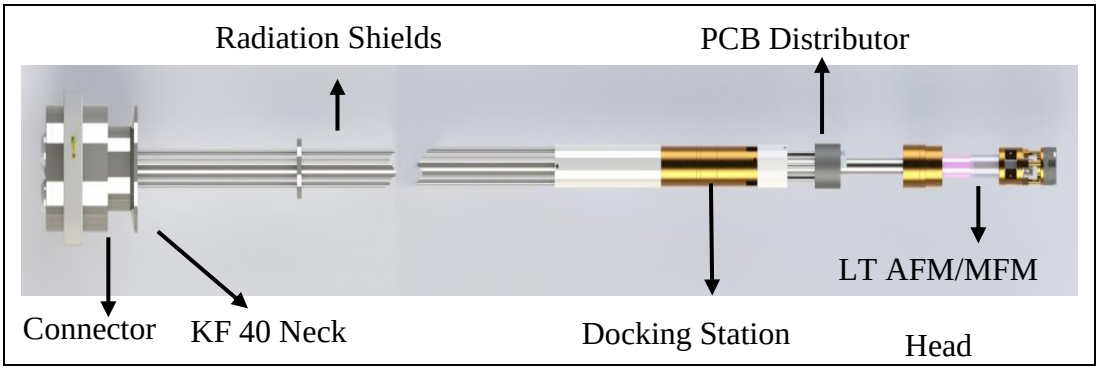

Figure 3. 3 LT AFM/MFM Insert and Head.

The other end of the insert has KF 40 connector to fit the cryostat variable temperature insert (VTI) with three vacuum seal connectors (LEMO Inc) and fiber passed through the insert and the sealed part (Figure 3.4).

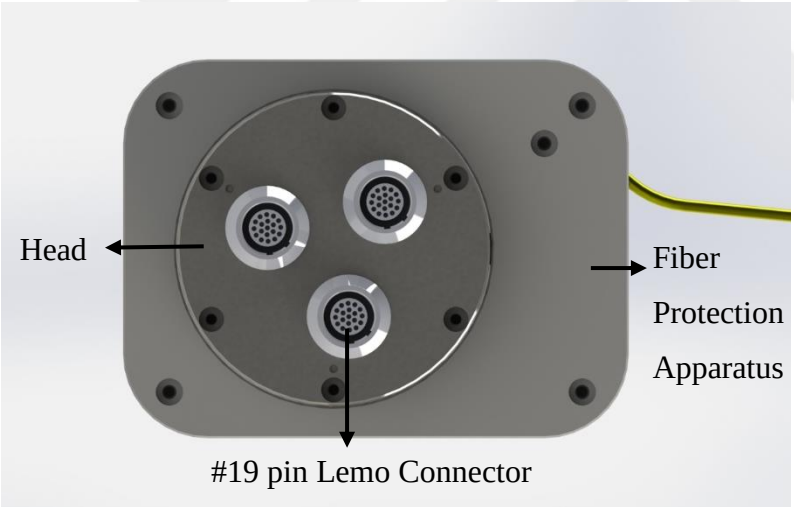

Figure 3. 4 The connector head.

3.1.4. Operation mechanism

Piezoelectric materials have a leading role in scanning probe microscope systems. These materials are electromechanical transducers, which can transform the electrical potential to the mechanical movement. They could be used in the opposite sense in other applications as well. Piezoelectrics occur naturally and can be amorphous,

polymeric, and crystalline. In AFM applications, mostly synthetic ceramic materials are used. Due to applied voltages to the opposite side electrodes of the piezoelectric devices, the geometry would alter based on the amplitude of the applied voltage, material, and device geometry. (Figure 3.5)

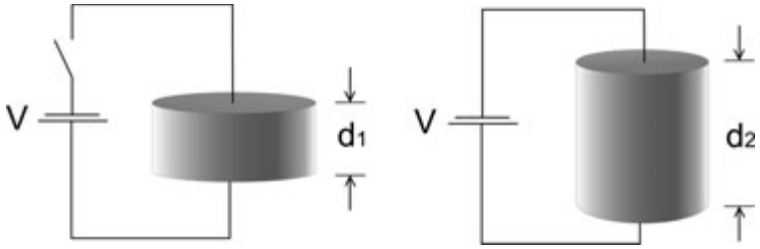

Figure 3. 5 Expansion of the Piezoelectric disk due to the applied voltage.

Technically, these materials have a specific coefficient of expansion with an order of around 0.1 nm by each drive volt, which makes entirely controllable tiny movements for AFM systems. When Piezo materials are under mechanical tension, the strength of the electric polarity would be altered. This phenomenon is called the 'direct' effect of piezoelectric. In reverse, if an electric field is applied due to unit cell distortion, material changes its shape, which is called 'transverse' piezoelectric effect. As it is mentioned, the piezoelectric ceramics ideally should expand in a linear regime and contact in a direct proportion to the applied voltage, but unfortunately, all these materials show some non-linear behavior. The first problem is hysteresis, in which the piezo tube tends to maintain the previous shape. And on the other hand, imposing the sudden impulse such a voltage step function to the ceramic makes creep.

The piezo tube used in LT AFM/MFM microscope is made by lead zirconium with four-quadrant electrodes outside the wall and one single electrode inside. When two reciprocal quadrants with grounded inner electrodes are under the opposite applied voltage, the piezo tube will bend in X-Y planes (Figure 3.6). Accordingly, applying the reverse voltage to all four quadrants, regarding the inner electrode, provides Z

direction motion which is used to keep the constant height to the surface throughout the scan.

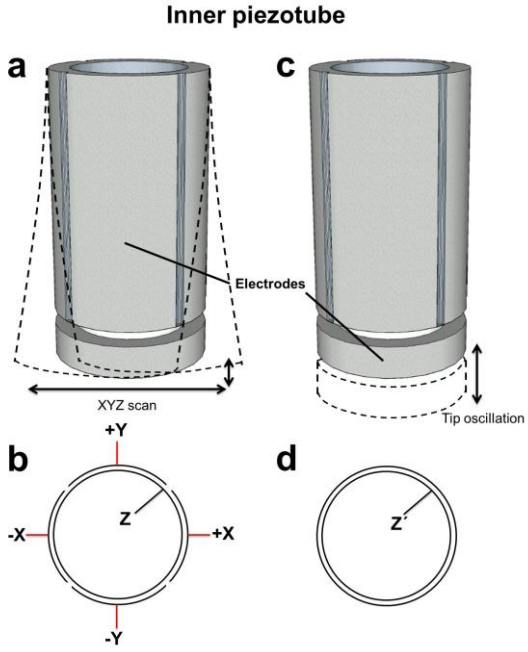

Figure 3. 6 schematics of the Inner piezo tube with the electrode contacts. The dash lines represent the piezo motion. (a) describes the four quadrants outside the tube wall and motion in the x-y plane. (b) shows the five contacts which are conducted within the inner piezo tube due to the scanning procedure in x, y, and Z directions. (c) represents oscillatory motion for cantilever oscillation with a single electrode on the top of the piezo tube. (d) the electrical contacts of a single oscillatory motion electrode, given by Z'. [51]

Piezoelectric is such sensitive materials which can be collapsed when subjected to various voltage values and operation under different temperatures during long term use.

The equation below represents the vertical displacement of the piezo tube scanner.

$$\Delta l = \frac{d_{31} l U_z}{s} \tag{3.1}$$

Here the $d_{31}$is transverse coefficient, l tube length, U_zThe electrodes employed voltage and s the tube wall thickness. Values for d_{31} @ 300 $K\ is$ − 1.73 Å/V, U_z is 100 V, l is 3 inch, and s is 0.5 mm.

Also, the piezoelectric lateral displacement can be calculated:

$$\Delta x = \frac{2\sqrt{2}\, d_{31} l^2 U_z}{\pi D t} \tag{3.2}$$

D denotes the otter dimension of the piezo tube with 6.35 mm.

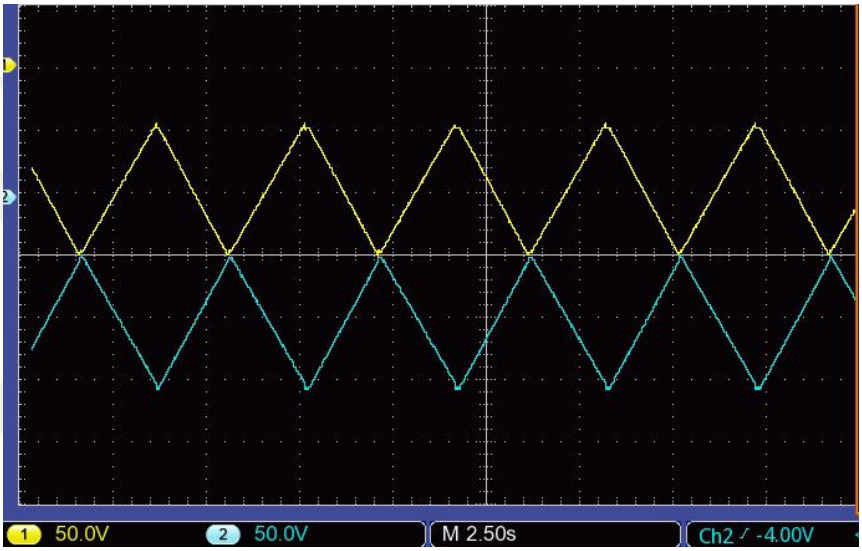

Figure 3. 7 The amount of the applied voltage to the scanner piezo tube quadrant. The maximum voltage is between ± 100V.

Scanner piezo is being manufactured in different length due to the various design. Table 3.1 shows the scanning range values for different length piezo at different temperature.

Here Based on the used piezo length, the piezo operation should be calibrated, which generally the microfabricated grating can be used for this purpose.

Table 3. 1 Scanner piezo tube scanning capacitance value in different temperature. [49]

Type and size of scanner piezo (EBL#2)	4K		77K		300 K	
	x- y	z	x- y	z	x- y	z
3 inch	18 µm	1.44 µm	39 µm	2.4 µm	108 µm	7.08 µm
2 inch	6 µm	0.80 µm	15 µm	1.40 µm	57 µm	4.80 µm
1 inch	3.5 µm	0.40 µm	6 µm	0.74 µm	17 µm	2.26 µm

Also, the capacitance value of the scanner piezo due to the change in the temperature is changing. Technically, reducing the heat make the capacitance drop; typically, with the same ratio in the scan range.

Table 3.2 gives the 3-inch scanner piezo tube capacitance value at different temperature.

Table 3. 2 Scanner Piezo tube capacitance values

Type (EBL#2)	300K	200K	77K	3K
3” Scanner	~12	~8	~4	~3

As already mentioned, calibration eliminates artifacts and keeps imaging with a right scale. But there are such drawbacks in the piezo tube scanner which coefficient of X-axis differs from Y-axis. Therefore, piezo should be calibrated carefully and separately for different axis. (Figure 3.7)

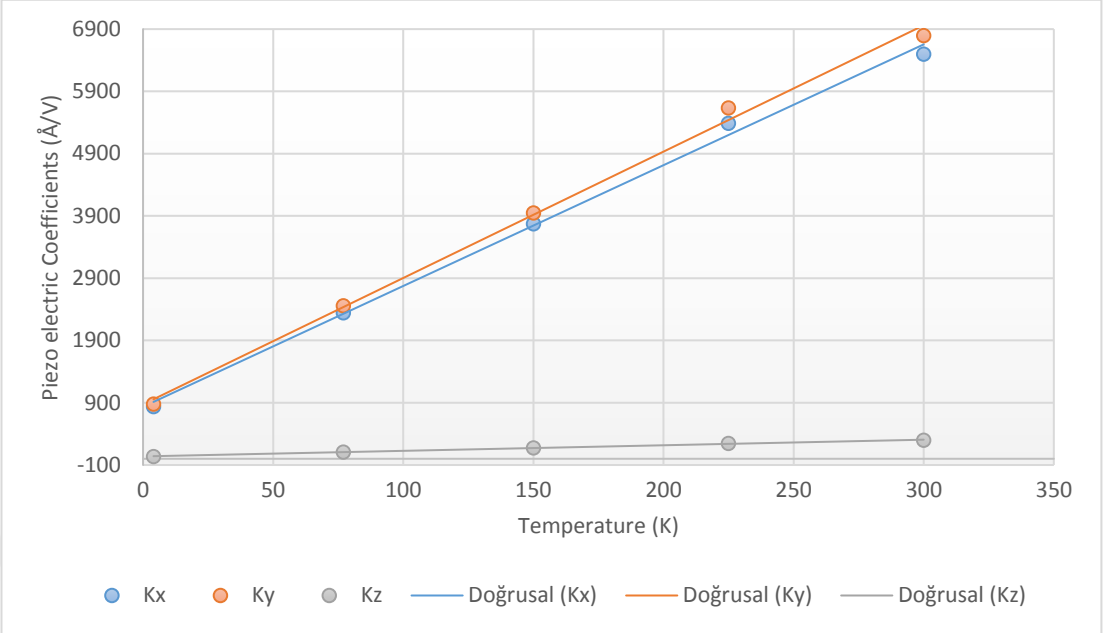

Figure 3. 8 3" scanner piezo tube calibration coefficients in different temperatures.

3.1.5. Approach and Retract Mechanism

Approaching and retracting movement of the sample respect to the probe is performed by the outer piezo tube and the quartz tube glass attached to the end, which so-called stick-slip method [52].

The schematic of the stick-slip principle shown in the figure below (Figure 3.8). Firstly, the sample holder mounted on the quartz tube and tightened with a leaf spring; then a voltage ramp should be applied to the outer piezo tube (technically extending /contracting the piezo around a few ms). During this period, the sample holder and the quartz tube move together because of the existence of the friction. And finally, the voltage is changed to be zero in a micro s (the outer piezo is contracted/extended). As a result, the sample holder can be slid on the quartz tube.

Piezo is capable of sliding hundreds of gram of mass in low temperature like 4K with this mechanism. The critical issue in this method is keeping an equilibrium between the friction force, and the inertia of the sample holder, which can be controlled by the leaf spring pressure on the quartz tube.

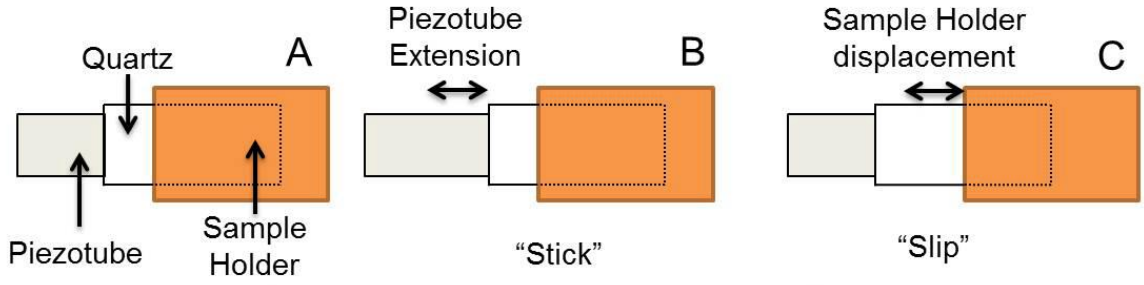

Figure 3. 9 Schematic design of the slip-stick mechanism. [51]

This scheme is a representation of the LT-AFM/MFM, showing the quartz tube, outer piezo tube, and sample holder (Puk). The three steps, A, B, and C, describe the holder displacement. In A, the holder is mounted on the quartz tube; then between A and B, the applied voltage pulse makes an extension or contraction in the piezo tube. In the end, the voltage goes to be zero, and the holder moves on the glass tube.

The real image of the pulse with the three steps on an oscilloscope is presented in Figure 3.10.

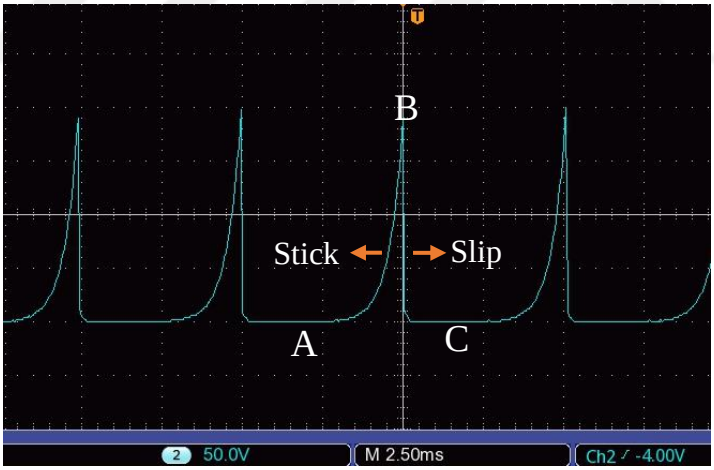

Figure 3. 10 Exponential pulses applied to the slider piezo in order to displace the holder.

3.1.6. Sample Positioning in the X-Y direction

Sample displacement in X-Y direction is the crucial issue, especially in low temperature. The Puk (sample positioner) design is capable to displace the sample

holder in a 3 mm diameter. The holder is responsible for holding the sample which is loaded via five pins on the Puk. One pin is for sample bias, and the rest are spare. The holder itself fiber-cantilever on the two couple parallel Zirconia rales, which one couple is in the X direction and another one is in the Y direction. These rails are placed on V-shape grooves beneath the sample holder and let the holder move in X and Y directions.

The sample holder displacement at the orthogonal directions is handled by the slider piezo. An applied high voltage to two neighbor quadrant couples concerning the opposite couples' quadrant provides the expected motion.

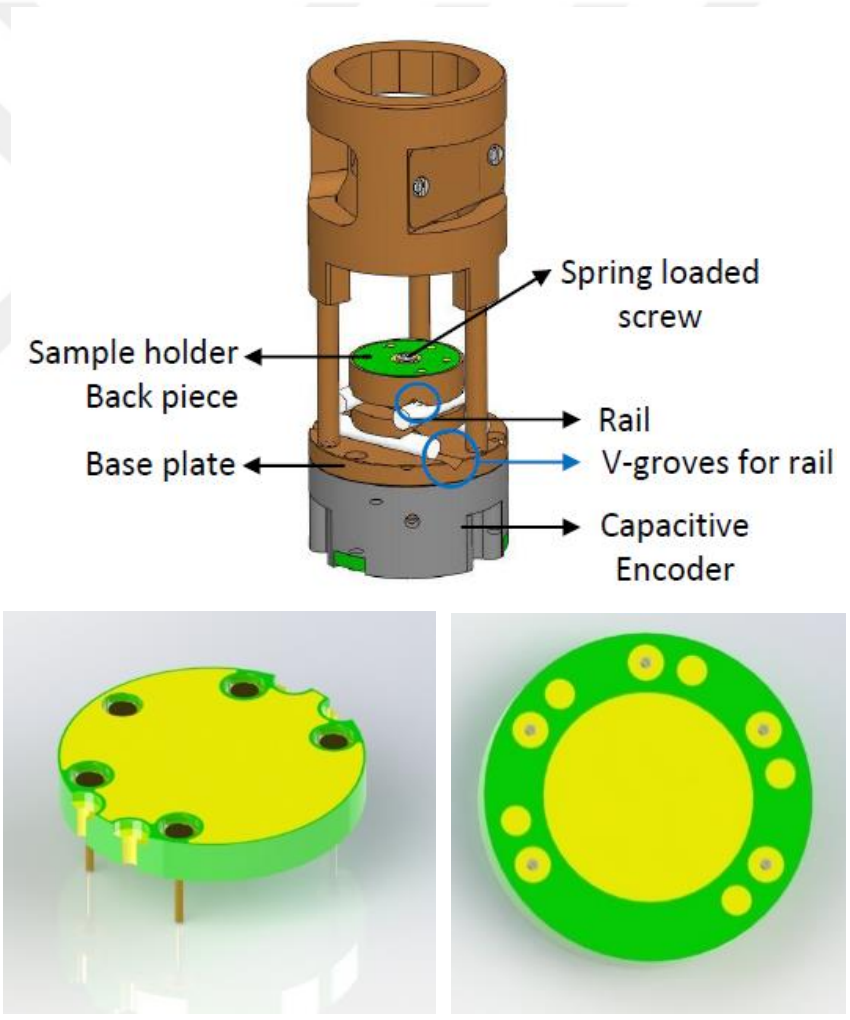

Figure 3. 11 Sample positioner and holders. [49]

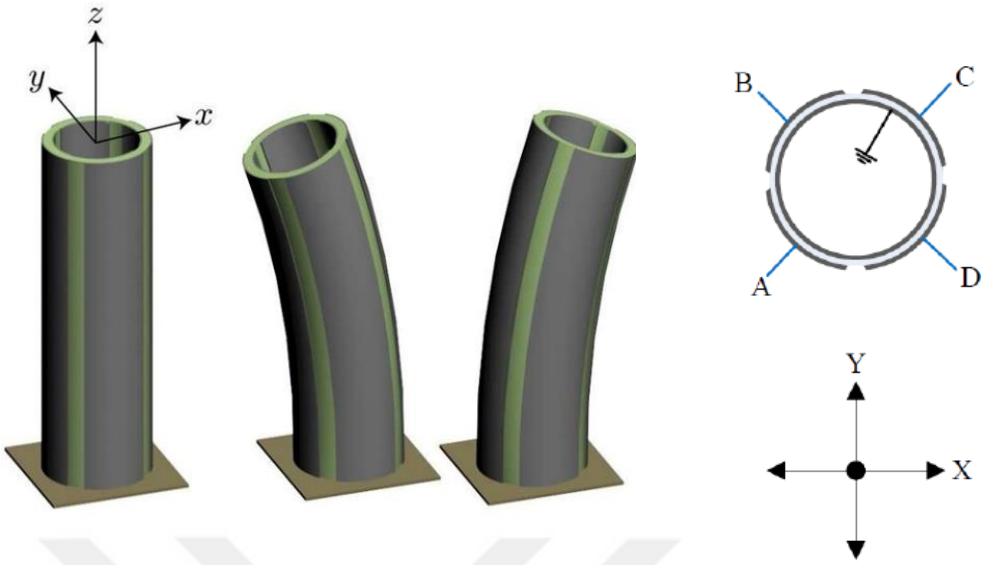

Figure 3. 12 Mechanism for sample movement in X-Y direction with slider piezo for sample positioning. The applied pulses to the AB-CD scanner piezo electrodes make the sample displace in X-axis, and AD-BC electrode makes it move in Y-axis [53]

3.1.7. Fine Approach Mechanism

The fine approach mechanism means landing the probe precisely controllable to the sample surface. In order to obtain this, the slider, as well as the scanner piezo, should be operated together. Firstly, the scanner piezo is retracted from the surface with a specific applied voltage. Then via the given pulse, the slider piezo approaches toward the surface one step. Moreover, the final step approaching the slider piezo through the sample slightly. During this procedure, to find out the interaction, the system controls the feedback and check any interplay among the sample and the deflection sensor. In case there is no interaction, the process continues until reaches the surface.

3.2. MFM Alignment Holder

3.2.1. Alignment Holder Design

The low-temperature AFM/MFM head is capable of operating in low temperature and positioning the cantilever in three-axis XYZ regarding the fiber with a self-aligned cantilever holder design.

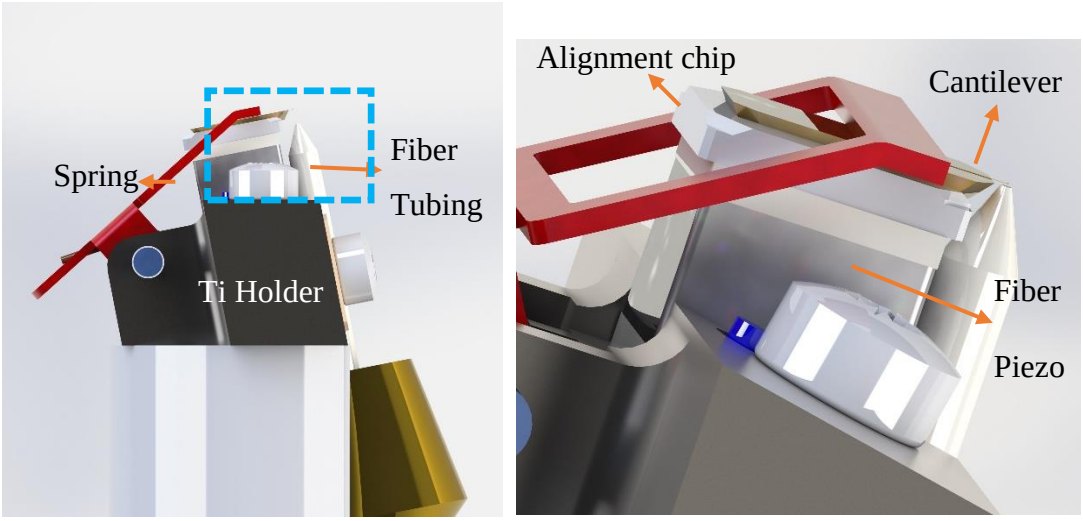

Figure 3. 13 Alignment holder schematic design.

The new modified design allowed us to improve the alignment holder. Changing the spring which pushes the cantilever. This helps to keep the cantilever more tighten on the chip holder and eliminate other noises interfering with the cantilever resonance frequency. Centralizing the probe tip precisely in front of the fiber which is moving in close vicinity of the tip. This achieved by providing the V-shape groove to embed the fiber and holding it with a leaf spring to move the fiber efficiently and accurately focused on the back of the tip. Also centralizing the fiber improves the slope value as well.

The main point which can be achieved by the self-aligned mechanism is compatibility for using a different type of cantilevers. Besides, the cantilever chip holder is machined with three protrusions, and cantilever back has groves in the same size of protrusions. This issue is a great advantage in fiber-cantilever alignment design in mounting the cantilever accurately.

Figure 3. 14 Cantilever Alignment holder chip and cantilever.

In the design, it is attempted to apply the similarly thermal contraction coefficient material. (Table 3.3) The body which is manufactured of the Titanium is screwed on the glued plastic holder (Polyphenylene sulfide (PPS)) on the top of the scanner piezo tube. Technically the titanium part is assembled by the fiber piezo, cantilever alignment chip, and the spring in the way that the fiber piezo sandwiched between two small ceramic parts to avoid high voltage leaks and on the top of the ceramic the cantilever alignment chip is positioned. All these parts are glued with a compatible epoxy to the low-temperature. And the assembly is designed to stay in around 11 degrees tilted using a titanium holder that allows just the cantilever tip to get in contact with the sample surface. In summary, the new alignment design is entirely reliable at the low temperature, working range of 1-300 K without any collapse.

Figure 3. 15 Alignment holder of the cantilever in front of the fiber tubing

Table 3. 3 The dimensions and contraction coefficients **α of** the utilized material at the design

Material	**Component**	**α (10^{-6}/K)**	**Size Z (mm)**	**Size XY/OD (mm)**
Alumina, Al_2O_3	Ceramic	8	0.5	3 x 4
Lead Zirconate Titanium	Fiber piezo	6	2	3 x 3
Silicon, Cr coated	Alignment chip	6	0.53	2.9 x 6.7
Titanium	Alignment holder	8.6	6	11 x 11
Silica, SiO_2	Fiber	0.75	7	0.125
Zirconium	Ferrule tubing	8	7	11

3.2.2. Fiber Cable

The standard single-mode, 1310 nm wavelength, fiber cable (TTAF Inc.-Turkey, OZ Optics-Canada) utilized to manufacture the microscope.

At first, the fiber is cleaved and then using the Zirconia ferrule tubing (Kientech Inc., USA), the fiber is inserted. It is attempted to position the fiber inside the ferrule tube respect to the cantilever back tip. Moreover, we tried to keep the fiber a few micrometers away from the ferrule tip to avoid any damage and reflectivity waste.

3.2.3. Cantilevers

Typically cantilevers which are manufactured by NanoSensors [60] are used in the design. Different types of cantilevers with their properties from NanoSensors Inc are listed in table 3.4. To increase the efficiency of the reflectivity, the backside of the cantilever is usually coating with Al. Moreover, MFM cantilevers are being coated by hard magnetic materials with various coercivity and magnetic moment, suitable for the imaging sample to restrict any damage to the sample magnetization. One of the significant parameters in enhancing the MFM resolution is the usage of a sharp tip. There are various ways in the fabrication of the MFM cantilever, like CoFe coating of carbon nanotubes[54], Fe-Filled carbon nanotubes [55], Co tips grown by electron beam [56], focused ion beam milled CoPt tips [57], Co spike tips by electron beam induced deposition [58], and paramagnetic material coating on the tip [59] which help to improve the MFM resolution around 20 nm.

Table 3. 4 cantilevers type with properties

Cantilever	Tip Radius of Curvature (nm)	fo (kHz)	k (N/m)	Dimensions (LxWxT) (μm)
PPP-FMR	<10	45-115	0.5-9.5	225x28x3
SSS-MFMR	<15	45-115	0.5-9.5	225x28x3
PPP-MFMR	<30	45-115	0.5-9.5	225x28x3

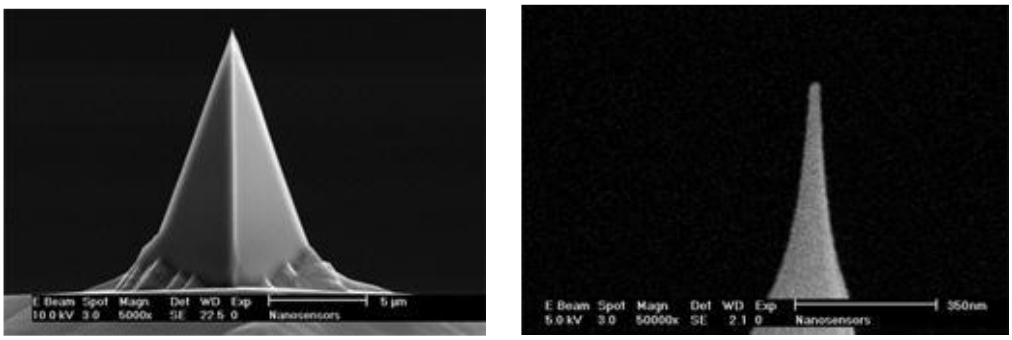

Figure 3. 16 the Silicon made MFM cantilever scanning electron microscopy image (SSS-MFMR). [60]

3.3. Optical laser Interferometer method

Optical Laser Interferometer method is being used for measuring the cantilever displacement in a way that the back of the cantilever is focused by a laser beam (I) through an optical fiber. At the end of the fiber, the surface will reflect the laser light partly (I_{rs}), and the remaining light will go toward the cantilever back. The cantilever will act as a mirror and reflect part of the laser (I_{rc}) through the same fiber to the source where they interfere. The interferometer pattern is a function of the optical path of each beam and hence the fiber-cantilever separation to represent the cantilever bending.

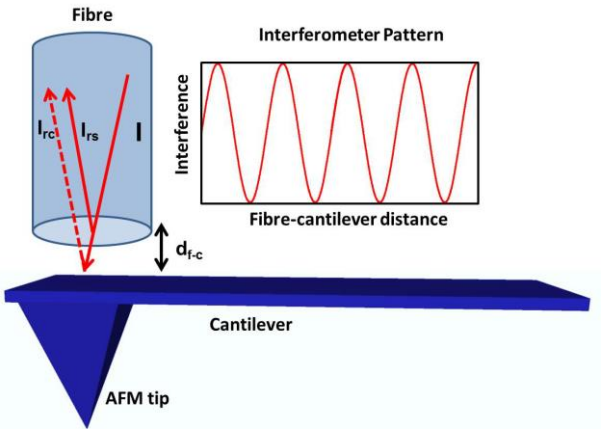

Figure 3. 17 Schematic design of the interferometry method. The laser beam (I) go through the fiber to the cantilever and part of that reflected from the fiber surface (I_{rs}), part of the rest beam again reflected from the cantilever (I_{rc}) back to the source. The $d_{f\text{-}c}$ is fiber- cantilever distance.[51]

3.3.1. Michelson Fiber Interferometer Principal and design

In order to measure the cantilever displacement, a low noise fiber interferometer with the Michelson principal is designed, which is similar to Rugar design [37-38]. A 1310 nm laser diode with a constant power is coupled into 2x2 single-mode 50% fiber splitter.

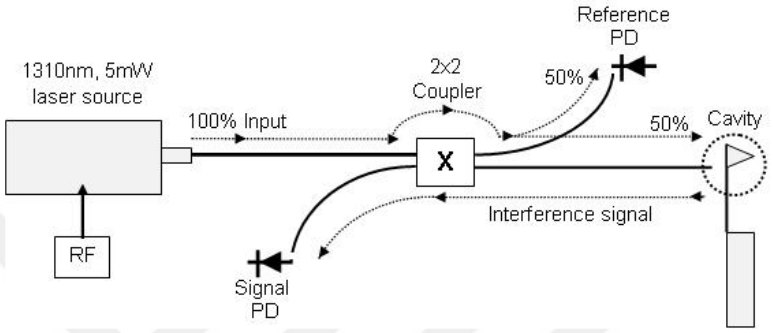

Figure 3. 18 Michelson fiber interferometer schematic design. [49]

After coupling the input laser, 50% goes through the fiber to the end of the cantilever and reflected through the same cleaved fiber. The other 50% is connected to the reference photodiode in order to monitor the laser power. Part of the reflection laser is reflected from the end of the fiber (usually around 3%), and the rest light passes to the cantilever. Both reflection light and light from reference photodiode is being directed to the signal photodiode to interfere. The photocurrent generated by the interference can be described as:

$$I_{inter} = I_0\left[1 - Vcos\left(\frac{4\pi d_{f-c}}{\lambda}\right)\right] \tag{3.3}$$

$$I_0 = \frac{I_{max} + I_{min}}{2} \tag{3.4}$$

$$V = \frac{I_{max} - I_{min}}{I_{max} + I_{min}} \tag{3.5}$$

$$R = \frac{V_{signal} - R_{F-signal}}{V_{Reference} + R_{F-Reference}} \tag{3.6}$$

Where I_0 is midpoint current, V is visibility, $d_{f\text{-}c}$ the fiber-cantilever separation, R the reflectivity, and λ the laser wavelength. The most sensitive positions in the interferometer are the quadratures, d= $\frac{\lambda}{8}, \frac{3\lambda}{8}, \frac{5\lambda}{8}$

Also, the slope of the interference can be calculated by:

$$m = \frac{\Delta I}{\Delta d} = 4\pi I_0 \frac{V}{\lambda} \tag{3.7}$$

Here respectively Δd and m are the displacements of the cantilever and interference pattern slope. The standard value for the interferometer interference slope is around 4 mV/Å. To maximize the precision of the measurement the equilibrium distance within the cantilever and the fiber is arranged to be maximum of the interferometer slope pattern. The max slope, which is the quadrature point on the interferometer could be defined by mapping the pattern of the interference via displacing the cantilever with the stack fiber piezo underneath it. The applied voltage to the fiber piezo in the two directions of the forward and backward regard to the fiber is 0-100 V.

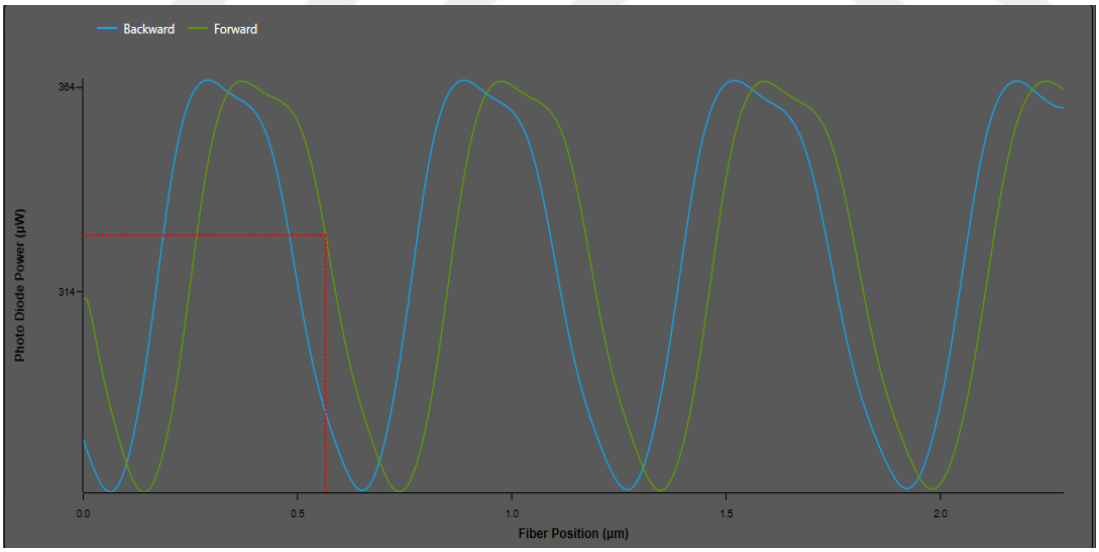

Figure 3. 19 Michelson Interferometer Interference pattern. The average slope is 4.27 mV/Å with visibility 0.27and at 327µWquadrature power.

3.3.2. LT-AFM controller

As already is explained, the interferometer measures the bending of the cantilever which is received by Phase Lock Loop (PLL) card that is responsible to excite the cantilever and the resonance frequency. Moreover, measuring the phase and amplitude of the output signal from the cantilever.

A power supply system with very low noise is provided for the LT-AFM/MFM controller which has a high voltage amplifier with four channels that drives the piezo. An exponential pulse up to 400 V is generated to run the stick-slip mechanism from the slider card.

The control mechanism description for LT-AFM/MFM microscope is presented in the figure below.

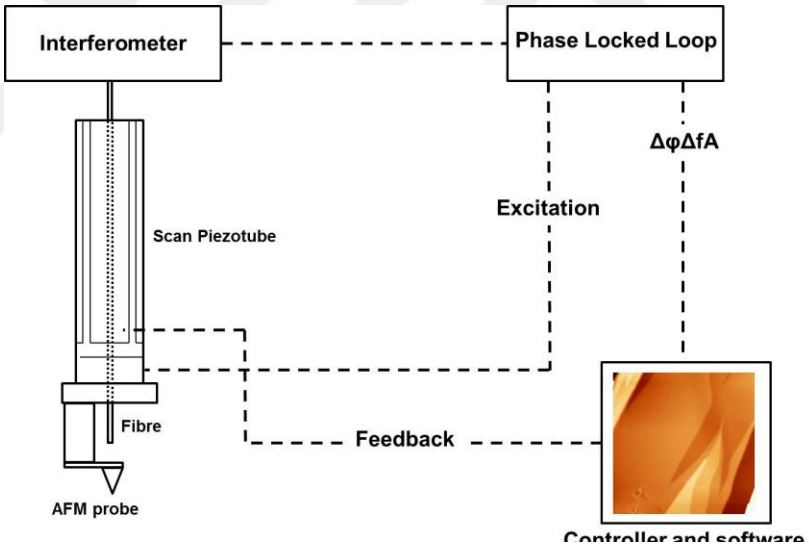

Figure 3. 20 LT-AFM control scheme.[51]

Dash lines represent the connection between the microscope and different elements in the controller. The interferometer records the information of the AFM probe displacement and then transmits to the Phase Locked Loop card. Both the frequency or amplitude shift is utilized for the feedback in the controller operation.

CHAPTER 4

LOW-TEMPERATURE EXPERIMENTS

4.1. Low-Temperature alignment mechanism Tests

Possibly the thermal contraction in the Z-direction could be calculated using the interferometer directly. During the cool down the system, usually, at the interferometer pattern 6 periods ($\lambda/2$) shifts are measured. mathematically, this shift resembles around 3.93-micron Z-direction displacement.

The drift in the XY direction can be measured via the laser spot size. Technically, the fiber core diameter is 10 micrometers and its value of a nominal numerical aperture (NA) is 0.14 and the cantilever width is 28 micrometers.

The spot size made by the fiber on the cantilever can be measured with the following equation:

$$NA = n \sin \theta \qquad 4.1$$

n is the medium reflective index; the air numerical value is 1 and θ is the half-angle of the light maximum cone.

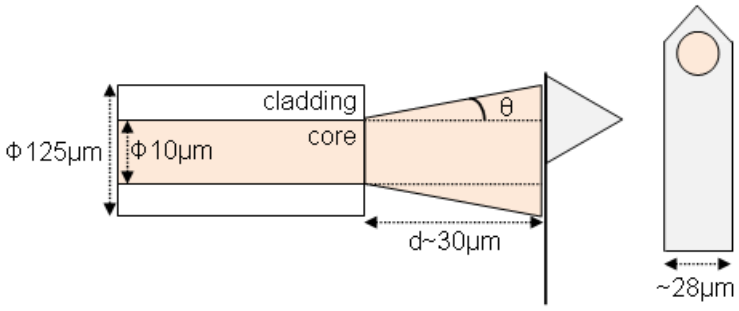

Figure 4. 1 schematic calculation size of the laser spot. [49]

Figure 4.2 represents the spot sizes based on the gap among the cantilever and fiber aperture which falls on the backside of the cantilever. In the Fabry-Perot LT microscope, the gap between the fiber and the cantilever is usually 1 micron or less, accordingly, the spot size is calculated to be around 10 microns. The typical drift in XY direction is less than 5 microns in variable temperature from room temperature to hundreds of millikelvin.

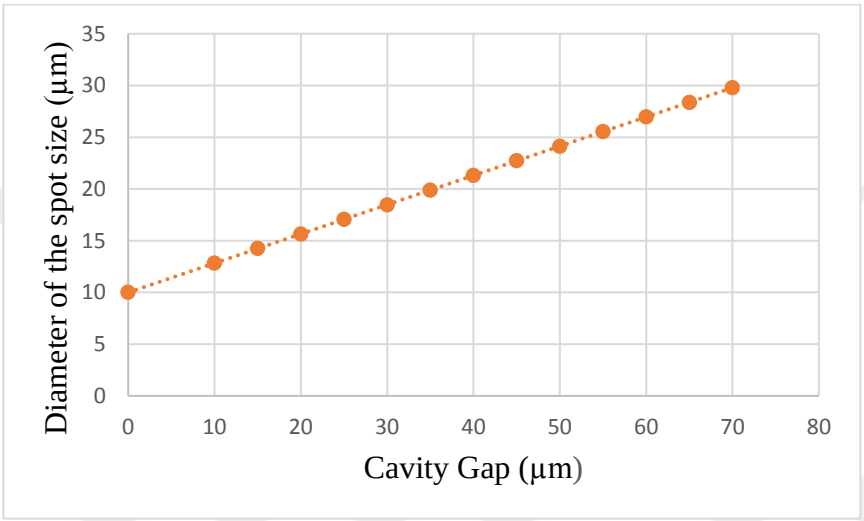

Figure 4. 2 Cavity gap vs spot size diameter.

Figures below depict the interference pattern in 300K and 3 K. The maximum power value in both patterns is 3 mW. At the 3 K, the piezo displacement will be about 400 nm with 150 V_{DC}. (Figure 4.3 b)

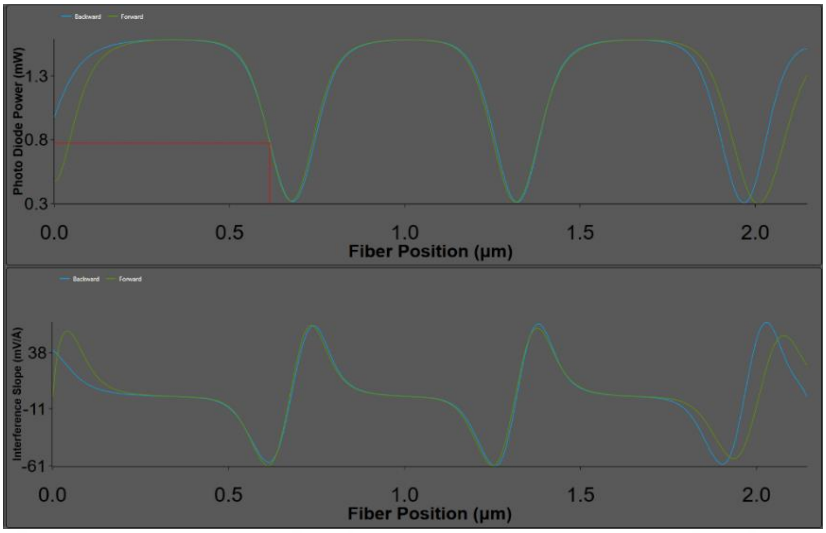

(a)

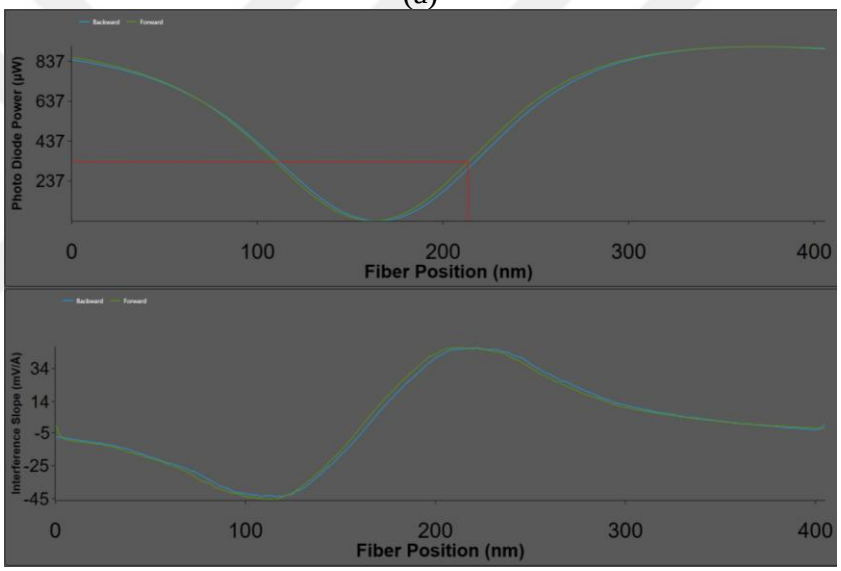

(**b**)

Figure 4. 3 sustaining the interference pattern in different temperatures represents the durability of cantilever-tip durability (a) 300K, (b) 3K

As the capacitance is proportional to the piezo displacement, due to cooling the microscope, the piezo capacitance will decrease from around 85 nF to around 15 nF.

The piezo displacement is proportional to its capacitance, hence, due to cooling the microscope, the piezo capacitance will decrease from around 85 nF to around 15 nF.

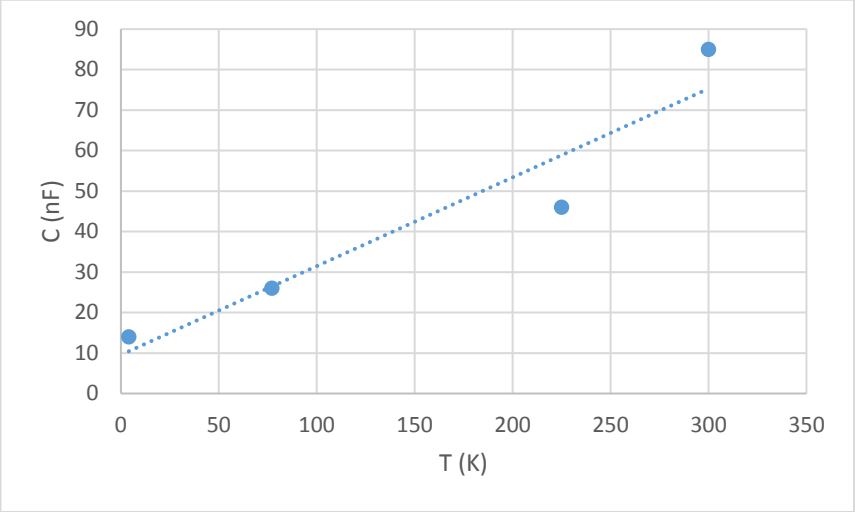

Figure 4. 4 Fiber Piezo capacitance change at the different Temperatures.

4.2. Noise Analysis

There are three main categories of noises that are affecting the fiber interferometer deflection sensor, namely, laser noise, shot noise, and electrical noise. The electrical noise itself is divided to Johnson noise, voltage noise, and current noise.

Table 4. 1 Noise sources affecting the deflection sensor.

Total Noise	1. Shot Noise		
	2. Electrical Noise	I.	Johnson Noise
		II.	Voltage Noise
		III.	Current Noise
	3. Laser Noise		

4.2.1. Laser Noise

The random fluctuations of various output parameters are summarized in a short term of Noise in the laser. This is a frequently encountered aspect that has an intense influence on various applications in photonics, especially in the area of accurate measurements. Consider e.g. variations of the transmission spectroscopic measurements or optical phase can affect interferometric position measurements,

where fluctuations of intensity restrict the feasible sensitivity. Furthermore, noise issues at least partially limit the data rate and the transmission distance for fiber-optic links.

Based on the different impact of the quantum noise and fluctuation of the several technical origins, the output of a laser noise constantly includes some noise. In a single-frequency laser, there are intensity or amplitude noise and phase noise.

The origins of the laser noise can be classified in quantum noise, in particular, correlated with the spontaneous emission in the gain medium and technical noise such as the excess noise if the pump source, or vibration of the resonator, or from temperature changes.

Moreover, the laser intensity is affected by many intrinsic noise sources of the laser diodes. The laser intensity noise can be described as:

$$\overline{v^2}_{intensity} = S_{PD}^2 P^2 R_F^2 \times 10^{-13} \left(\frac{V^2}{Hz}\right) \qquad 4.2$$

Here S_{PD} is the photodetector responsibility, P is the optical power of the incident beam, and R_F is, the feedback resistor to the photodetector I-V converter.

The laser phase noise also depends on the cavity gap between the cantilever and fiber. The laser noise can be defined as :

$$\overline{v^2}_{phase} = S_{PD}^2 P^2 R_F^2 4\pi\Delta v\, \tau^2 \times 10^{-13} \left(\frac{V^2}{Hz}\right) \qquad 4.3$$

The τ is the length difference of the optical path in the cavity gap which is divided by the light speed, and Δv is the laser diode bandwidth.

4.2.2. Shot Noise

Poisson or Shot noise is a sort of noise that could be determined with a Poisson process. The shot noise arises from the discrete feature of the electric charge. The electronic current random fluctuations are the origination of the shot noise in the DC

mode electronic circuits. This occurs due to the consistency of the flow of discrete electron charge and originally defines as arising from the random occurrence of photon absorption events in a photodetector. Shot noise is independent of the temperature and frequency.

4.2.3. Electrical Noise

4.2.4. Johnson Noise

The thermal noise is the general form of the electronic natural noise in circuits, that is produced by thermal motions of the electrons within any conductive and semiconductive materials. The thermal noise would cease to exist in the absolute zero (0 K). It is also known as Johnson noise. Due to the fact that the power spectral density of thermal noise across the full frequency spectrum is flat, that is also defined as White noise. The white noise voltage spectral density is given by:

$$\overline{v^2}_{Johnson} = \sqrt{4k_B T R_F}\ \left(\frac{V}{\sqrt{Hz}}\right) \qquad 4.4$$

4.2.5. Current and Voltage noise

These two noises are organized within the amplifiers intrinsic features which are employed for the fiber interferometer.

4.2.6. Total Noise

The total noise is the contribution of all these discussed noises which is already calculated to be around 11 fm/Hz$^{1/2}$ [61].

4.2.7. Noise measurements

All noise sources which are discussed above can be measured as the cantilever thermal noise or the deflection sensor spectral noise density. The noise is measured by the Rohde-Schwarz spectrum analyzer when the fiber interferometer is locked at the quadrature, and the dither and scanner piezo are grounded.

The spectral noise density can be calculated mathematically and fitted to the experimental data [62]:

$$S = \sqrt{\frac{2k_B T}{\pi f_0 k Q} \frac{1}{\left(1 - \left(\frac{f}{f_0}\right)^2\right)^2 - \left(\frac{f}{f_0} Q\right)^2}} \qquad 4.5$$

Where f_0, f, T, Q, k and K_B respectively are resonance frequency, frequency, temperature, Q-factor, cantilever spring constant, and Boltzmann constant.

The experiment was done in 300 K with the normal tapping, non-contact mode cantilever from NanoSensors Inc (PPP-NCLR) which has a spring constant of 21-98 N/m. Mathematically, the cantilever spring constant is calculated to be 70 N/m using the thermal noise spectrum.

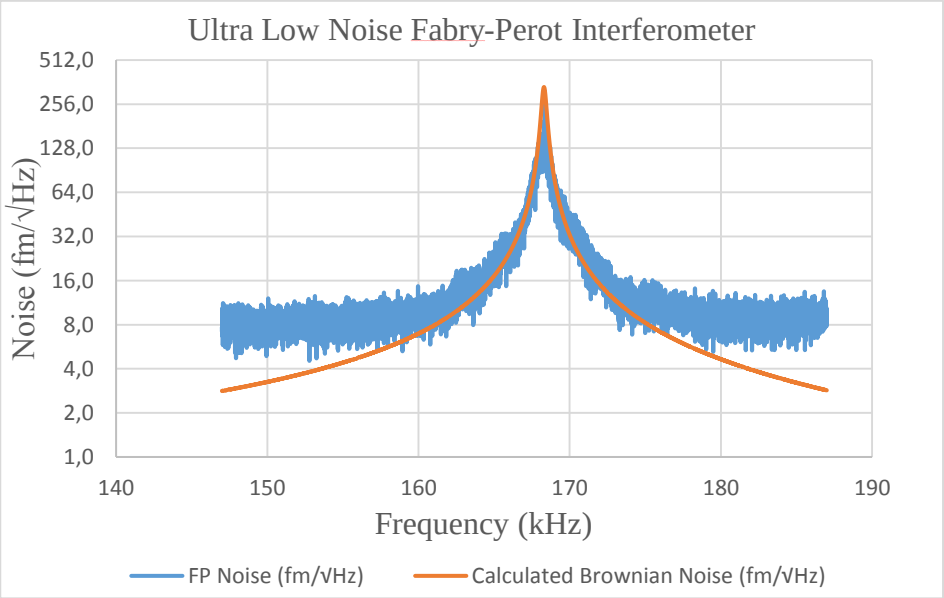

Figure 4. 5 The fiber interferometer spectrum noise density at 300 K.

Also, the graph is fitted by the theoretical calculation with f_0 168 kHz, Q factor 500, k is 70 N/m.

The laser power also has an effect on the deflection sensor. Decreasing laser power makes extreme noise. The main reason for this dramatic noise is shot noise.

The figure below shows the noise level of the interferometer in various laser power.

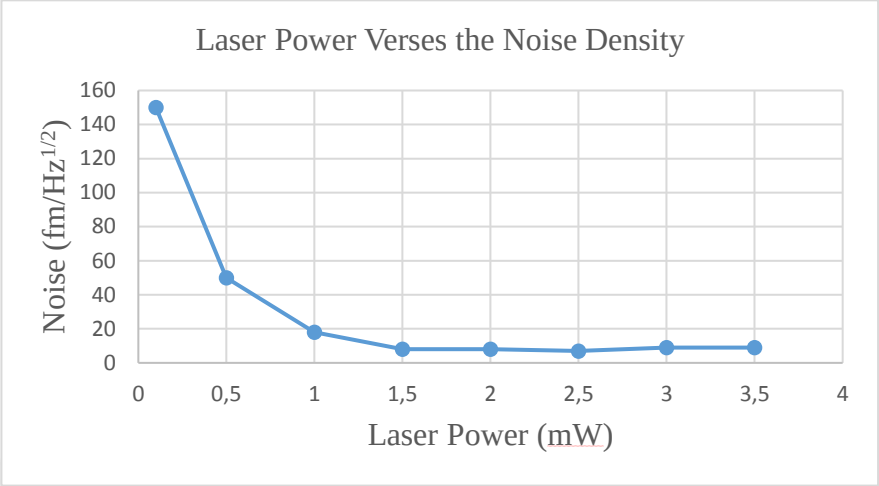

Figure 4. 6 The laser power versus the noise density conducted in 300 K.

The laser power of 2.5-3 mW is determined to be an optimum value in all operation and measurements.

4.3. Images

4.3.1. Tapping Mode AFM Image

Tapping mode AFM [27] technique maps the topography with smooth taps on the sample surface by and a sharp AFM probe tip when it oscillates at its own resonance frequency. In this mode, a scanner piezo excites the cantilever substrates vertically and generates the vertical oscillation of the cantilever. Principally the cantilever reflects the laser beam from the backside in a regular pattern over a photodiode array which generates a sinusoidal electronic or detector signal.

Typically, the cantilever oscillates close to the resonance of its frequency at the air and before engaging to the sample surface. When the probe approaches and finds the surface, the oscillation amplitude decreases and by controlling the changes in the amplitude and continuously feeding back on an amplitude setpoint, the tip maps the surface by moving up and down to maintain constant oscillation amplitude. By this,

we can reach the high-resolution three-dimensional image of the sample surface topography.

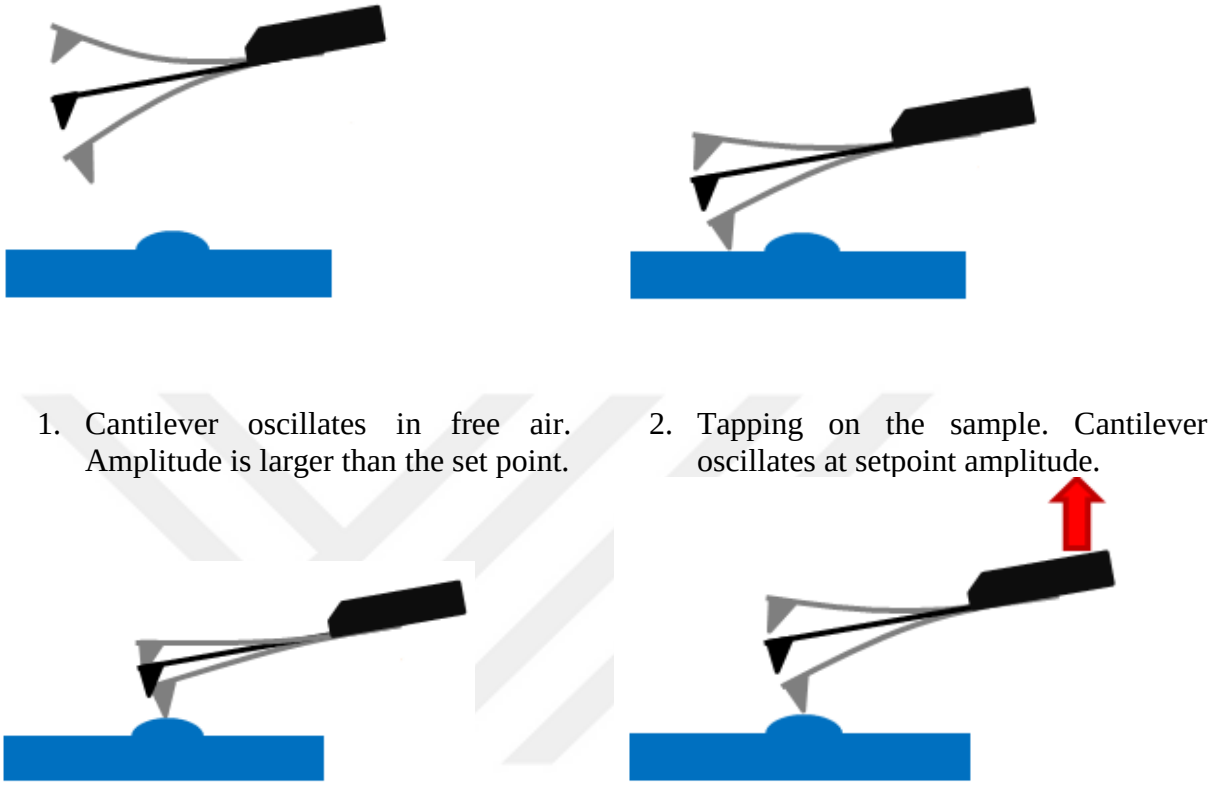

1. Cantilever oscillates in free air. Amplitude is larger than the set point.
2. Tapping on the sample. Cantilever oscillates at setpoint amplitude.
3. Tip encounters a particle. Cantilever oscillation amplitude drops
4. The piezo lifts due to the feedback to returns the Amplitude to the setpoint.

Figure 4. 7 cantilever motion in tapping mode. [63]

The tapping mode technique is one of the important methods in scanning probe microscopy as it overcomes some of the restrictions in contact mode AFM by eliminating the lateral forces to the surface which can distort or damage the sample. The capability of working in both air and the fluid environment as well as routine imaging of the soft and delicate samples, or samples which are weekly attached to a substrate which are difficult to be operated in contact mode AFM are the vital features of tapping mode AFM.

When the drive frequency is at or close to the resonance frequency of the cantilever, the shacking of the piezo can provide a large cantilever oscillation around 2-100 nm in free air. Though, drive frequency away from the cantilever resonance frequency results in the amplitude drop immediately. This is because the cantilever's natural response is out of phase and the piezo shaking energy is less efficiently transfer to the cantilever. Therefore, driving the cantilever at its resonance frequency results in the constant oscillation amplitude. And when the cantilever is brought close to the surface the force gradient between the tip and the sample effects to the resonant frequency and potentially makes the shift and the amplitude of the oscillation reduces. The attractive forces make the resonance frequency shift get lower, and repulsive forces, make the frequency shift higher.

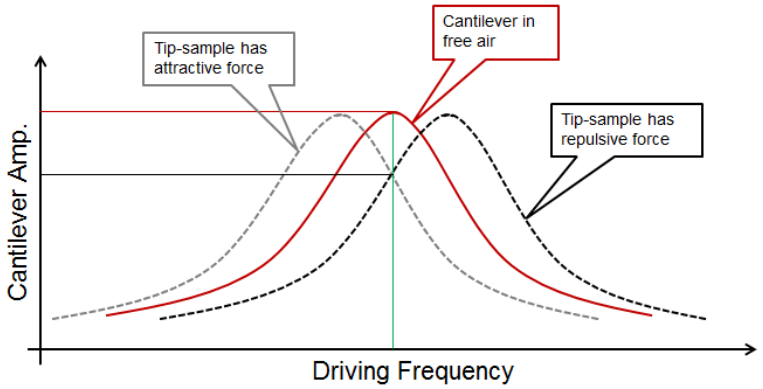

Figure 4. 8 Cantilever oscillation amplitude vs. drive frequency. [63]

Additionally, to the topography image, the phase image can be recorded by the tapping mode. The phase image provides data about the material hardness, both charge or magnetic field distribution within precise measurements and composition. Also, the tapping mode is utilized for MFM measurements in the way that forward scans with the same principal present the topography image and the backward scans give the phase shift as well as magnetic image.

Figure 4.9 shows the atomic steps of the Mika layers imaged with the tapping mode technique. For the sample preparation, firstly the Mika is cleaved by scotch tape and etched with a 49% HF solution for 4 hours. Then washed with the deionized water and

dried with dry nitrogen. principally the atomic layer of the Mika is 1 nm at different temperatures. Imaging the single layers of materials with the LT Fabry-Perot microscope shows the great capability of reaching to high-resolution operation specifically in low temperatures.

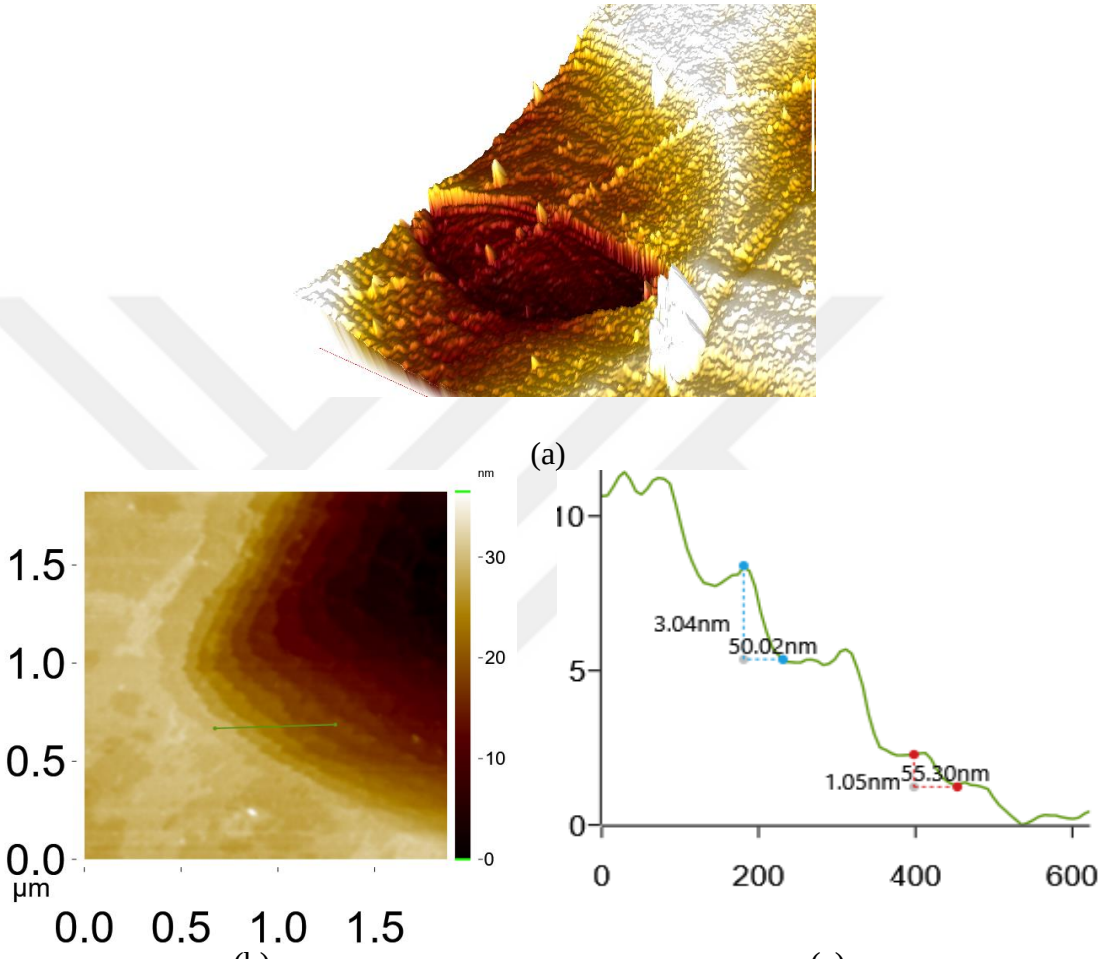

Figure 4. 9 (a) 3D image of Tapping mode Mika sample topography which is HF etched and recorded at 3 K. (b) tapping mode topography image. (c) cross-section of the image depicts the atomic single layer and multilayers steps.

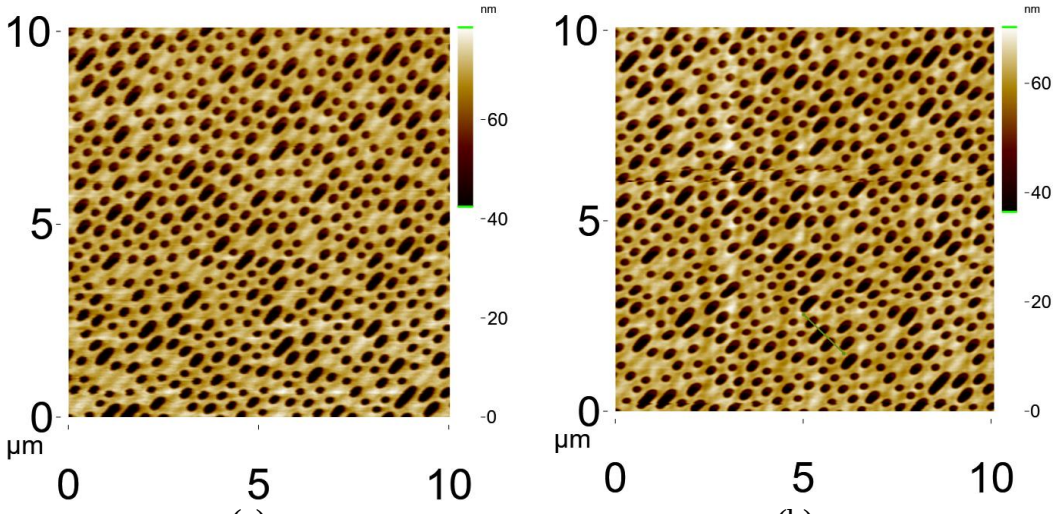

Figure 4. 10 The Bluray disk sample topography image in tapping mode (a) at 300 K (b) at 3 K

4.3.2. MFM Images

4.3.3. Magnetic Poles

The oppositely magnetized domains on the sample produce different domain magnetic poles which would result in the stray field on the surface. This stray field can be detected by the magnetic tip. For example, in such this setup, moving the MFM probe across the sample surface will experience two various forces on the domain wall caused by the different magnetic poles. Therefore, the two repulsive and attractive forces can cause different oscillations on the tip between the different regimes during imaging and conclusively the image representing the state of the stray field can be recorded.

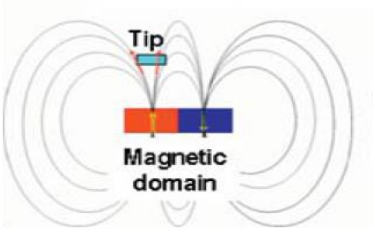

Figure 4. 11 Magnetic stray field produced on the sample surface. [64]

4.3.4. Lift-Height Adjustment

The other force sources like Van der Wall forces aside from the magnetic force influence on the tip, therefore it is necessary that the probe kept in a specific distance through imaging. Here the importance of the two-pass technique is obvious, recording the topography image in forwarding and magnetic image in backward in specific lift height. The lift-amount is so critical to image an ideal magnetic image. This provides the chance to keep the tip in a specific height to interact with magnetic stray field better and away from other interactions. In case the lift amount is not sufficient, the magnetic image can be contained with the topographic features as the tip still under the effects of the short-range forces.

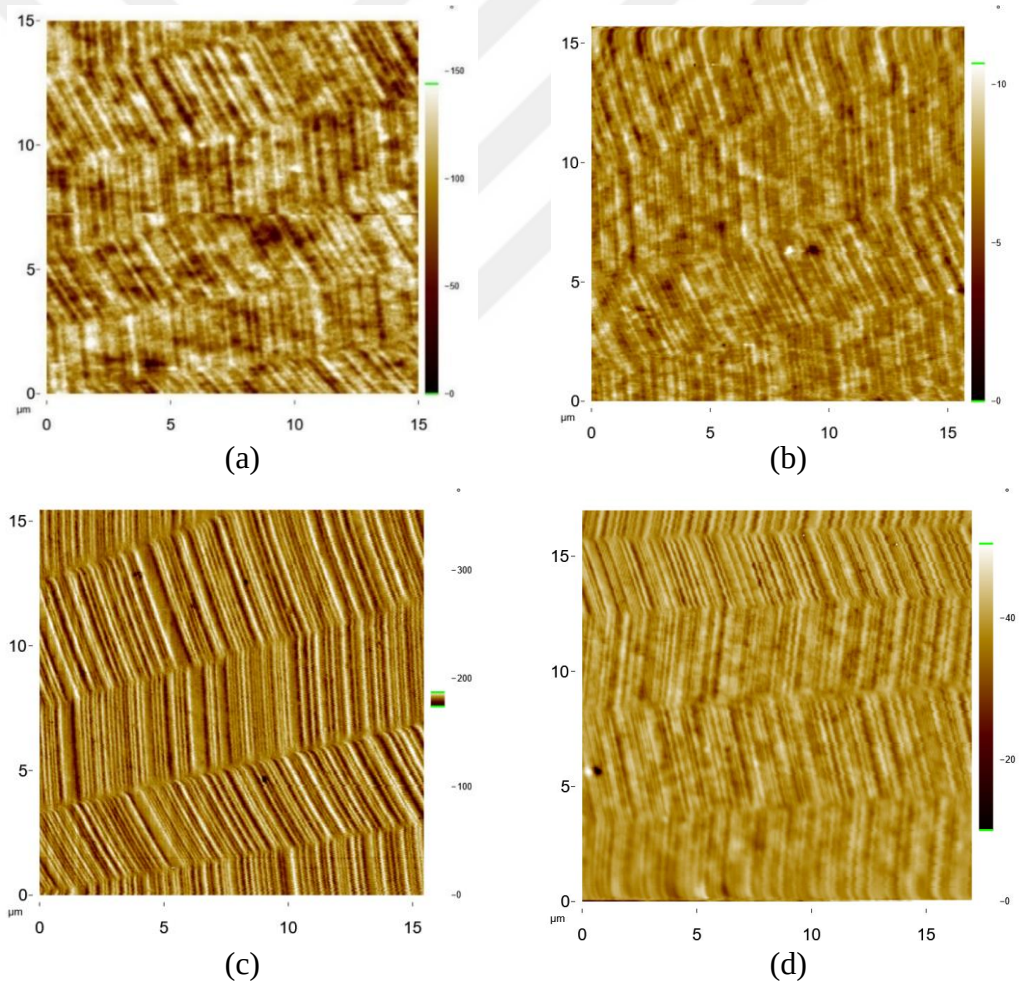

Figure 4. 12 Sony hi8 tape MFM images with different lift height parameters. (a) 80 nm, (b) 100 nm, (c) 120nm, (d) 150 nm

In Figure 4.12 (c) with the 120 nm, lift-off value seems an ideal value and there is no artifact. Besides, the resolution is much higher and clear compared to other images. The artifacts of the sample topography on the image (a) is apparent.

Also, increasing the lift amount makes the resolution get worse. This is due to decreasing the magnetic stray field strength with a factor of $1/r^3$. And mathematically, increasing the lift height decrease the phase shift as well.

4.3.5. The MFM tip Size

One of the significant roles in determining the high-resolution magnetic image is utilizing the optimized size magnetic tip. Although increasing the coating material due to increasing the magnetic moment of the tip helps to record a better resolution image, increasing the tip size is such a disadvantage for a high-resolution image. Moreover, the signal contrast, and resolution spontaneously influence the MFM image quality. This means that lateral resolution decays when the tip diameter increase. On the other hand, the contrast will drastically improve by increasing the tip diameter, until the optimized diameter size. This fact can be contributed to two outcomes: firstly, increasing the effective diameter would increase the number of actual magnetic poles. The stronger interaction will happen between the tip and magnetic domains of the sample surface because of more magnetic poles on the tip. This fact enhances contrast. Secondly, The intrinsic feature of the magnetic lines. Figure 4.13 shows the behavior of the interaction between the tip and magnetic domain according to the tip diameter. Based on the magnetic field lines the interaction can be defined. The smaller tip diameter, less magnetic field passes and vice versa the tip can feel more magnetic field as the diameter increases. However, when the tip size reaches in a certain value the opposite magnetic field lines also interact with the tip and complementarily reduce the force gradient. This fact implies the adequate tip size helps to obtain a better quality MFM image.

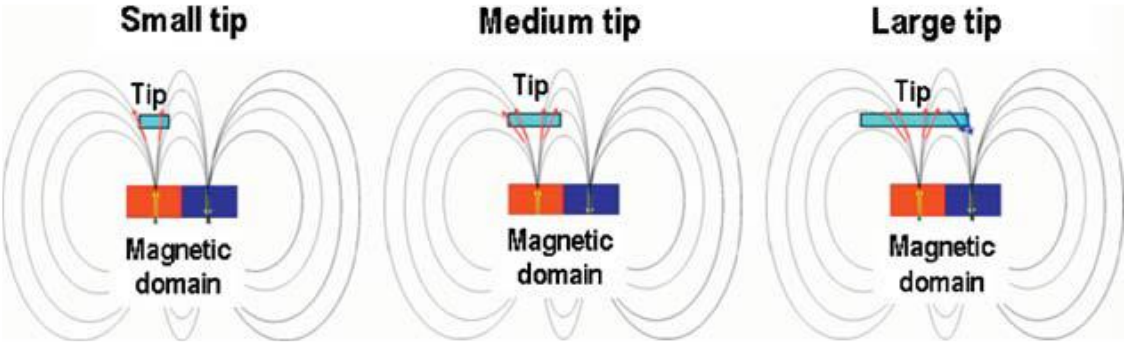

Figure 4. 13 Tip interaction in the magnetic field domain.[64]

CHAPTER 5

LOW TEMPERATURE

5.1. The Cryogenic temperature

The definition of the cryogenic temperature starts from -150 ºC to the absolute zero -273 ºC, which is the temperature that molecular movement becomes close to the theoretically possible to completely stop.

Principally, the cryogenic temperatures happen below the temperatures which are faced in the common physical processes. In that severe circumstances, the features of the materials such as ductility, strength, thermal conductivity, and the electric resistance are changed in both theoretical and commercial importance, as the heat is generated by the random movement of the molecules. Materials in the extremely low temperature are highly ordered and close to the static state.

In 1877, after cooling the oxygen to its liquid point for the first time (90 K), the cryogenics had begun. Then the theoretical development due to the development of the refrigeration systems started. In 1895, it was the possibility to reach to 40 K and liquified the air and separate into the main components. The helium liquified at 4.2 K, in 1908, and then after the attempt to supercooled materials and lose the resistance to electricity led to discover the superconductivity phenomenon. The absolute zero was reached in the 1920s and 1930s. And since 1960, laboratories are capable to experiment a millikelvin temperature.

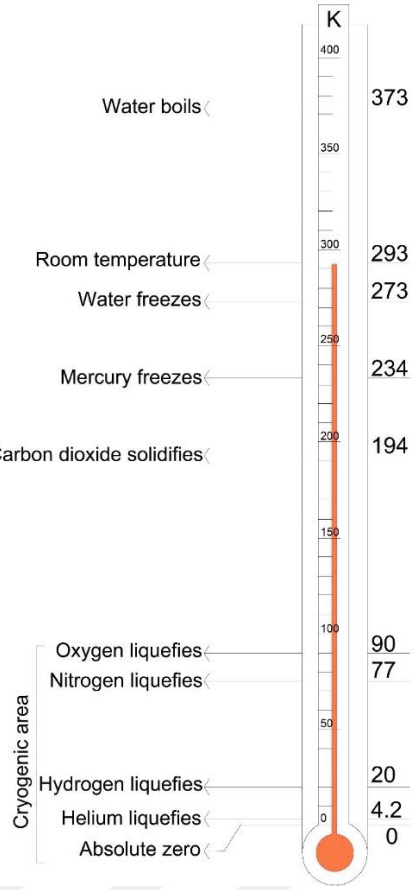

Figure 5. 1 The schematic description of the cryogenic temperatures.

5.2. Introduction to LT-AFM/MFM

The capability of the microscope working at a low temperature of around 300 mK carries vital significance in various areas of material science. This would be a great opportunity to investigate material properties.

Different kinds of cryostats provide various temperatures from a few kelvins' ranges to millikelvin. The cryostats which have a cooling ability to decrease the temperature down to 300 mK are called ^{3}He cryostats.

In this type of cryostats, two cryogens liquid Helium and ^{3}He are used. At the first step, the liquid Helium cooled the temperature of the sample down to ~1.5 K, and the ^{3}He gas is introduced to the system that liquefies at 3.19 K. In the high vacuum space of the cryostat, finally, the temperature drops below 300 mK.

5.2.1. Dry Cryostat

A cryogen-free design is meaning that no liquid cryogens are required to cool the system or during normal operation. The cooling system consists of a cold head mounted on the cryostat and an external compressor. The cold head cools both the magnet and radiation shields within the cryostat as well as the recirculating helium gas in the gas handling system (GHS). Respectively the radiation shield and magnet can arrive at their base temperatures of 40 K and 3.5 K.

The system uses helium gas in the gas handling system (GHS) to cool the variable temperature insert (VTI) as an exchange gas inside the sample space. Because of this, both the GHS and the sample space must be filled with helium gas before the system is cooled.

Without the gas recirculating, the VTI and sample will cool to about 150 K when the system reaches its base temperature. In the GHS, the helium gas is pumped into the cryostat connection lines and cooled as it passes through a series of heat exchangers attached to the cryocooler, before passing through a needle valve in the VTI. As the helium gas exits the needle valve, it expands and cools via the Joule-Thompson principal, and enabling the VTI to reach temperatures below 1.8 K. The expanded gas is then pumped back out of the cryostat and reinjected in a continuous cycle.

The sample itself sits in a helium exchange gas which is not part of the circulation loop. This greatly reduces any chance of contamination of the recirculation loop gas when changing samples.

The procedure can be operated by balancing the cooling and heating power, respectively with recirculating helium to cool and heaters, as a pair of cartridge heaters positioned on the tail of the VTI. The sample heater controls the sample temperature under normal conditions from 1.3 K to 300 K. Therefore, the cryostat provides the capability for all ranges of temperature for different experiments.

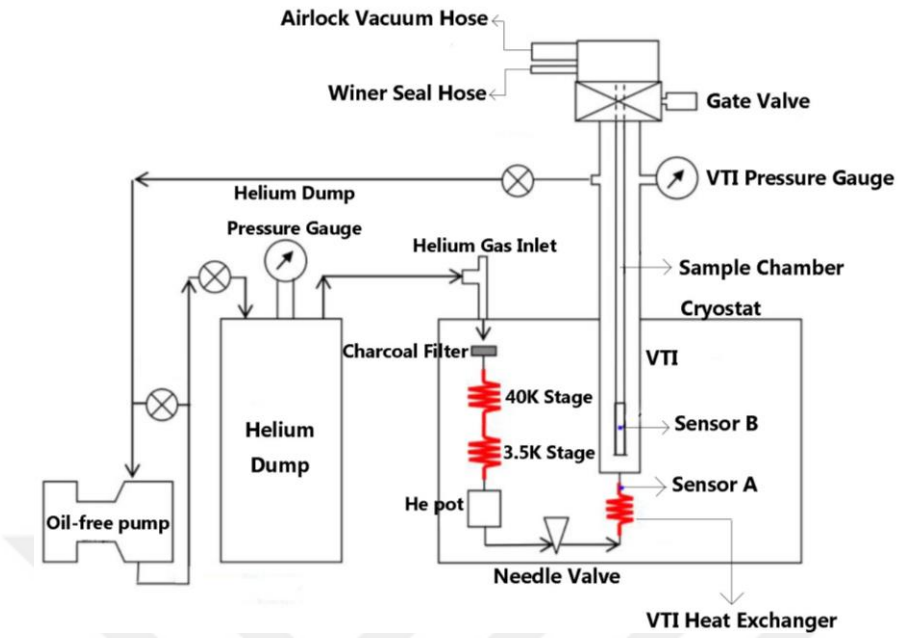

Figure 5. 2 The cryostat and gas handling system schematic design. [65]

5.3. Cryocoolers

A refrigeration machine which is the main part of the cryostats with the capability of cooling lower than123 K and a small refrigeration space is called the cryocooler. Principally, recuperative and regenerative are two types of cryocoolers. The former includes the Brayton and Joules Thomson type, and the latter involves Stirling and Gifford-McMahon type cryocooler. Mainly cryocoolers are utilized to cool the infrared sensors in the missile guided system and satellite-based surveillance, the cooling of superconductors and semiconductors, as well as applications such as in cryopumps, liquefying natural gases, cooling of radiation shields, SQUID (superconducting quantum interference device), Magnetometers, Semiconductor fabrication, etc.

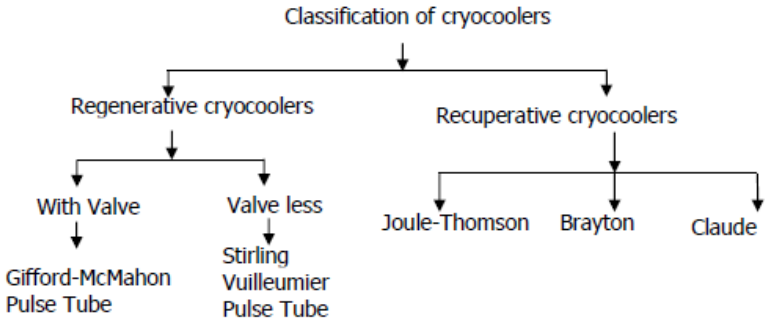

Explicitly the high usage demand for cryocoolers, small size, long lifetime, performance efficiency, reliability, low vibration, and weight become important aspects in the development of cryocoolers. The smaller heat transfer loss and higher efficiency of the Stirling and Gifford-McMahon (G-M) type cryocoolers bring them to a widely used in many applications. Due to the construction simplicity by eliminating the moving part at the cold end, pulse tube cryocoolers have more advantages over other cryocoolers and reliable in operation. Generally, there are two types of pulse tube cryocoolers. The table below represents the overall comparison of these two systems.

Table 5. 1 Stirling and G-M type Cryocoolers Comparison.

G-M type cryocooler	**Stirling type cryocooler**
Use of oil-lubricated compressor	Use of dry compressor
Working at Low frequency (1-5Hz)	Working at high frequency (20-120Hz)
A compressor connected to the expander through a valve	Compressor directly connected to the expander
Pressure ratios are high	Pressure ratios are low
Low Coefficient of performance	High Coefficient of performance
Compressors are bulky (capacity is in kW)	Compressors are small (capacity is in few hundreds Watts)
Can a below 2K using two stages of cooler	Can attain 20K using two stages of cooler

Pulse Tube cryocoolers or Refrigerators are pulsing the pressure from one end of a hollow tube and observing cooling effect from the other end for the first time is recognized by Gifford and Longsworth in the early sixties. This was the initiation of the most promising cryogenics refrigerators Comparison which is classified as basic pulse tube refrigerators (BPTR). This type of refrigerators is more in the attention because of enhanced reliability, long lifetime, and simplicity because of the absence in the moving part at the cold temperature region.

The pulse tube refrigerators (PTR), unlike the other typical refrigerators which are using the vapor compression cycle based on the classical thermodynamics, is achieved by the oscillatory compression theory and gas expansion within the enclosed volume to reach the desired refrigeration. Based on being oscillatory, a PTR is not a steady system that demands the time-dependent solution. However, PTRs are a quasi-steady periodic state (steady-periodic mode). Principally, a periodic steady system is a cycle that will reach the same state in the next cycle and so on. The PTRs are working in a closed system with using the oscillation pressure which is regularly provided by an oscillatory piston in one end to generate a flow of oscillating gas in the rest of the system. Here the gas is responsible to carry the heat away from the point with low temperature (cold heat exchanger) to the hot end exchanger.

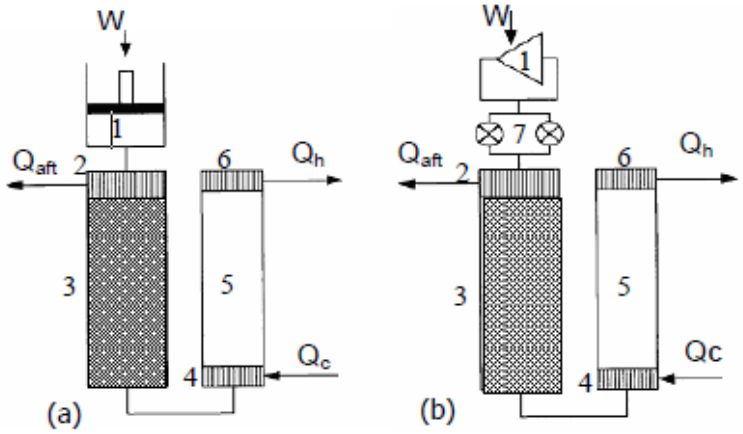

Figure 5. 3 (a) Stirling (b) G-M type BTR Schematics. 1.Compressor, 2. Aftercooler, 3. Regenerator, 4. Cold heat exchanger, 5. Pulse tube, 6. Hot heat exchanger, 7. Valve [66]

The heat of compressor compression in a Stirling type PTR is removed by the environment with a heat exchanger which is placed between the regenerator and compressor. The heat exchanger is known as an aftercooler or precooler. These principles are used in PTRs, present a capability to reach a temperature around 50 K. Although the Stirling type can produce higher cooling power due to the absence of the valve, the required rapid flow oscillation of the fluid heat exchange in this type limits the performance at the low temperatures, such 10 K and below.

The G-M type PTR by utilizing the valve, it can dispense low/high-pressure gas into the pulse tube. In this type of system, pulsation pressure is produced by the periodic opening/closing operation of the high/low-pressure valve.

The main components of the PTR are Compressor, aftercooler, regenerator, cold heat exchanger, pulse tube, and warm heat exchanger. Respectively each part are responsible for supplying the pressurized and depressurized gas to the closed chamber, ideally to extract all the heat which is produced in the compressor volume during the gas compression and release to the environment, as the most important component in the pulse tube refrigerators which is functionalized to absorb the heat during the forward stroke from the incoming gas and return that heat back to the gas in return stroke, the best resemblance to the evaporator in the vapor compression refrigeration cycle where the system absorbs the refrigeration load, to carrying the heat with enthalpy flow from the cold end to the warm end, and rejecting the generated heat from the gas.

The most recent invention is the inertance tube PTR. In the aforementioned type, the orifice valve is replaced by a long inertance tube which has a very small inner diameter and adds reactive impedance to the system. This modification generates a phase shift inside the pule tube and provides an enhanced enthalpy flow.

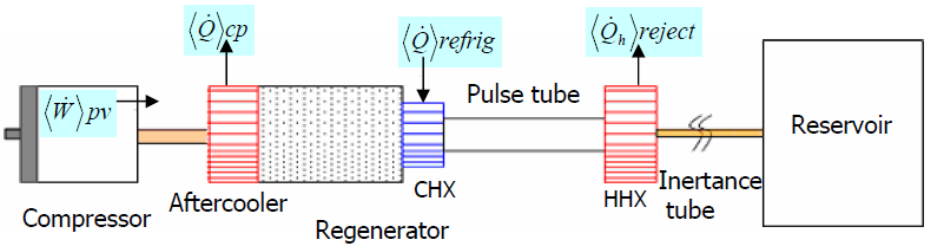

Figure 5. 4 The inertance tube PTR schematic diagram. HHX: hot heat exchanger, CHX: cold heat exchanger, $\dot{Q}$: $Heat\ rate,\ \dot{w}$: $Power\ [W]$, cp: Compressor, $\dot{Q}_h$: $Heat\ transfer\ from\ the\ hot\ end$. [66]

As it is impracticable to reach a very low temperature with a single PTR, the multistage PTR is introduced. Hence, one PTR can be used to pre-cool the other. For temperatures below the 30 K, the system is split into two. And finally, the three-stage PTRs are able to cool down to 1.78 k using the ^{3}He as a working fluid.

The rotation of the valve disk that opens the high pressure, starts the refrigeration cycle. At first, it releases the high-pressure helium gas to pass inside the regenerating material and the expansion space. Next, the pressure differential drives the displacer "up", enabling the gas at the bottom to expand and cool. And then, the rotation of the valve disk next opens the low-pressure path, allowing the cold gas to flow through the regenerating material and removing heat from the system. Eventually, the pressure differential returns the displacer to its original status, and the cycle is done.

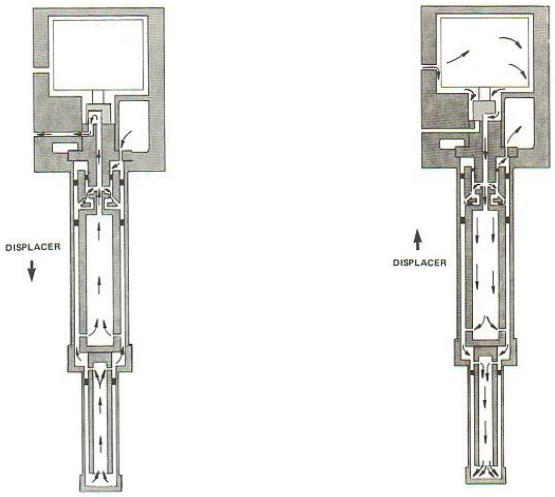

Figure 5. 5 The schematic of the cryocooler working principal. [67]

The cryostat system in all these experiments is the top-loading (TL) C-Mag from Cryomagnetics Instruments Inc. consists of a cold head mounted on the cryostat and an external compressor. The cold head has the capability of reaching 1.3 K. And the superconducting magnetic can provide 9 Tesla magnetic field which is integrated inside the cryostat.

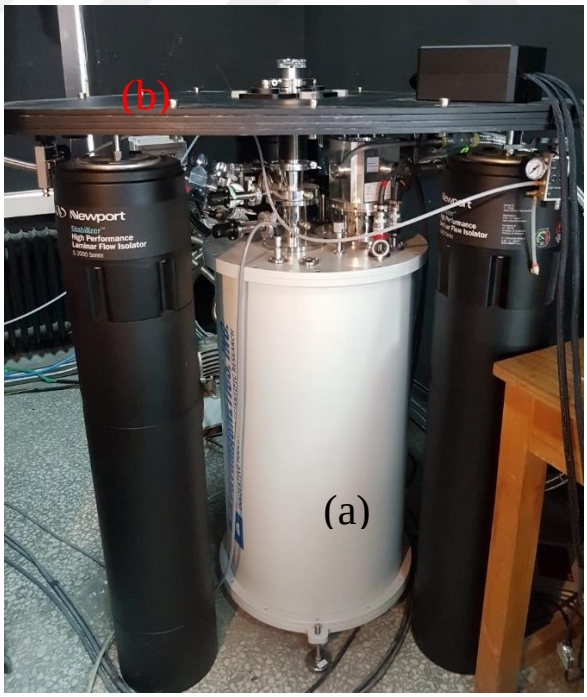

Figure 5. 6 (a) The cryostat, and (b) Isolation Vibration Platform.

5.4. Vibration Isolation

There are various factors coming from the environment which affects drastically the scanning probe microscopy (SPM) measurements. Technically, based on different environments in which the device has housed, these effects play a critical role. The vibration noise is the main issue that AFM measurements are highly susceptible to interference with. The two foremost types of vibration sense by AFM are mechanical and acoustic vibrations. Almost the acoustic nose could be eliminated by locating the instrument in an ideal place, far from the crowded place and audible activities as well as providing a sealed cabinet covered with soundproof material or damping one.

Transmission mechanical vibration to the AFM stage is more important as there are more sources of this strong type of vibration. Hence, all vibration sources in the laboratory should be considered particularly. For instance, the laboratory floor noises coming from the place that dry cryostat parts are positioned like cryocooler, pumping and connection lines, chiller, and etc.

The dry cryostats that are more common in scientific sections have affordable prices, easy to use, and elimination of He expense which is such advantages. The central drawback of this system is the vibration generated by the pulse tube transferring straight to the microscope. Here, the isolation vibration stage which specially designed for the cryostat can solve the mechanical noise problem by decoupling the pulse tube vibration. (Figure 5.6) In this design, the microscope is positioned on the vibration isolation stainless steel platform with around 300 Kg which is held on three air damping isolation legs [68].

Figure 5. 7 The vibration isolation table schematic design. (a), (b), and (c) are air damping isolation legs, (d) is an edge welded bellows, (e) platform.

The vibration table is connected with a cylindrical spring-type extension part to adsorb and separate the cryostat vibration from the microscope stage. Manufacturing the design with nonmagnetic material helps for high field application researches. Additionally, the compressor line connections are passed through a tighten concrete hole to decrease the noise coming from the circulation of the Helium gas.

Moreover, to diminish the noise pathing through the electronic connection cables, directly to the microscope, a heavy block of the 50 Kg is manufactured in the way that cables can sandwich in between two heavy block parts and then tighten with screws.

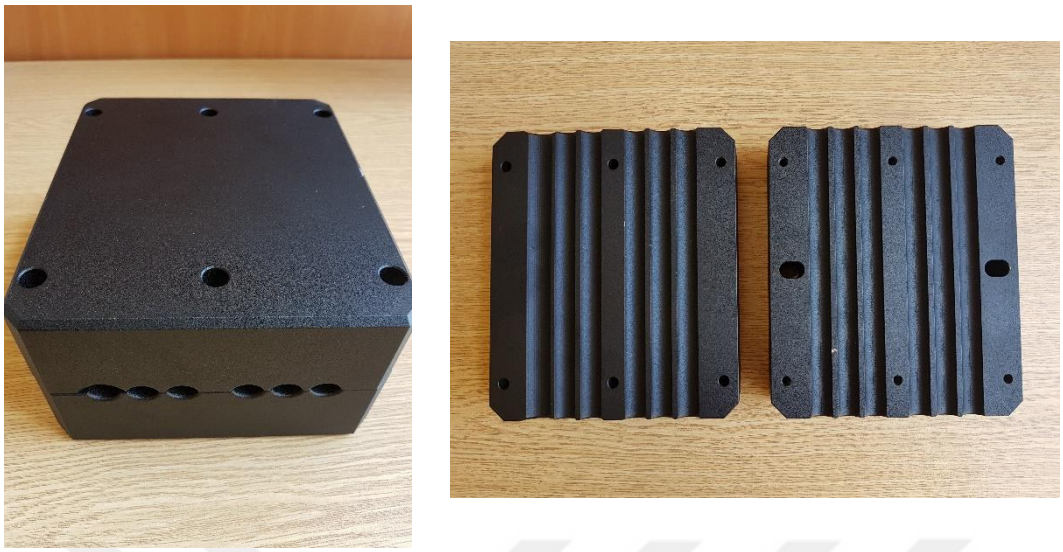

(a) (b)

Figure 5. 8 The cable noise-canceling block, (a) Screwed position and (b) Parts.

5.4.1. Vibration Isolation Performance:

In order to measure the vibration Isolation stage noise due to explaining the applicability of the stage in decreasing the noise, a HOPG sample scanned in a 10pm×10 pm scan range with a 20 nm scan speed in both status when the stage of off and on, and then the noise calculated.

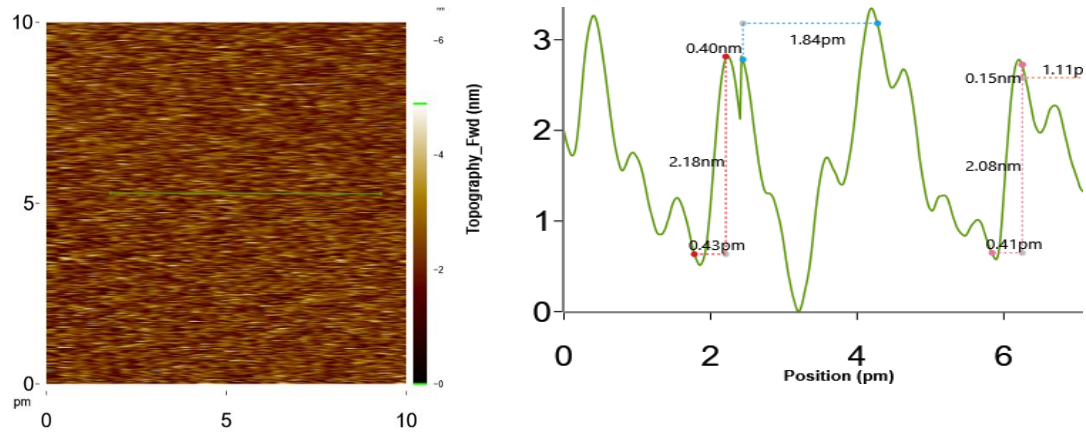

Figure 5. 9 10 pm x 10 pm HOPG scan image with the cross-section when the stage is off.

Roughness Parameters	
Coefficient	**Value**
Average (Ra)	0.98 nm
Root Mean Squre (Rq)	1.22 nm
Skewness (Rsk)	0.038
Kurtosis (Rku)	2.873
Maximum (Rp)	9.92 nm
Minimum (Rv)	0.00 nm
Peak To Peak (Rt)	9.92 nm
Ten Point Height (Rz)	9.71 nm

Figure 5. 10 Roughness parameters on the 10 pm x 10 pm HOPG image when the stage is off.

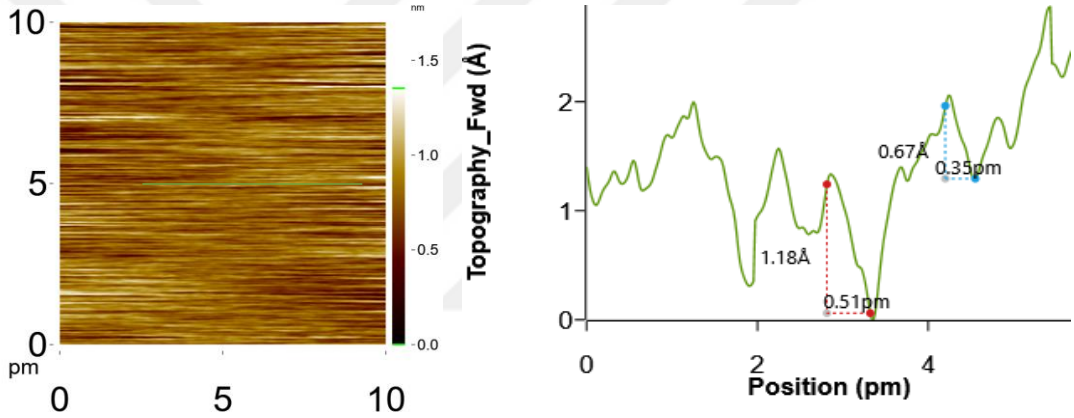

Figure 5. 11 10 pm x 10 pm HOPG scan image with the cross-section when the stage is on.

Roughness Parameters	
Coefficient	**Value**
Average (Ra)	0.12 nm
Root Mean Squre (Rq)	0.15 nm
Skewness (Rsk)	-0.064
Kurtosis (Rku)	4.012
Maximum (Rp)	1.70 nm
Minimum (Rv)	0.00 nm
Peak To Peak (Rt)	1.70 nm
Ten Point Height (Rz)	1.70 nm

Figure 5. 12 Roughness parameters on the 10 pm x 10 pm HOPG image when the stage is on.

The obtained the RMS noise in the existence of all noise around without utilizing the isolation platform was 1.2 nm while performing the isolation stage the noise level is reduced to 0.16 nm. This is suitable for most of the MFM applications using force microscopy as well as the atomic resolution imaging or manipulation. Furthermore, the histogram FWHM analysis claims the same level of the noise in both situations.

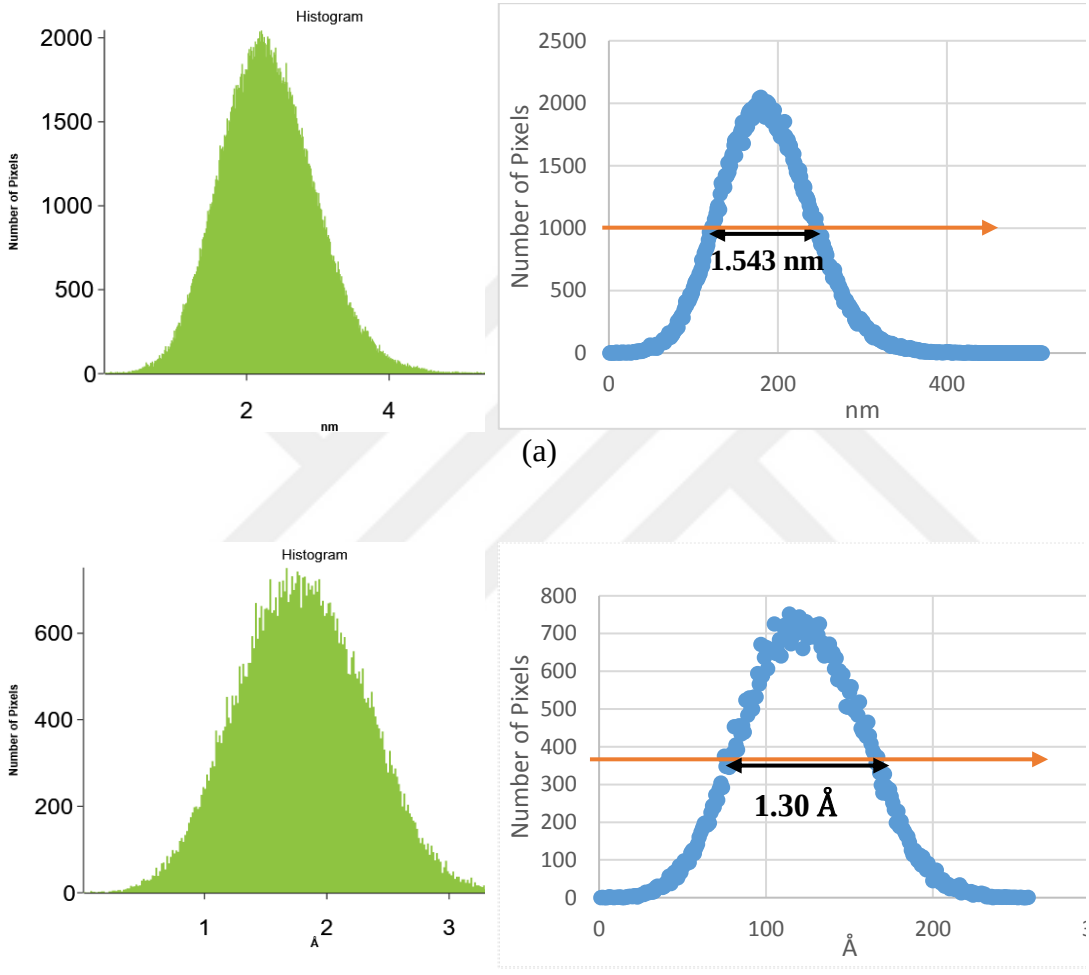

Figure 5. 13 histogram FWHM analysis of the scanned 10 pm x10pm HOPG (a) Vibration isolation platform is off, (b) Vibration Isolation platform is on.

5.5. Images

In order to examine the functionality of the microscope inside at the cold temperature, an iPhone camera chip was imaged by the AFM tapping mode in different

temperatures. Furthermore, the applicability of the vibration isolation platform is monitored by imaging the single layers of the graphene (0.34 nm).

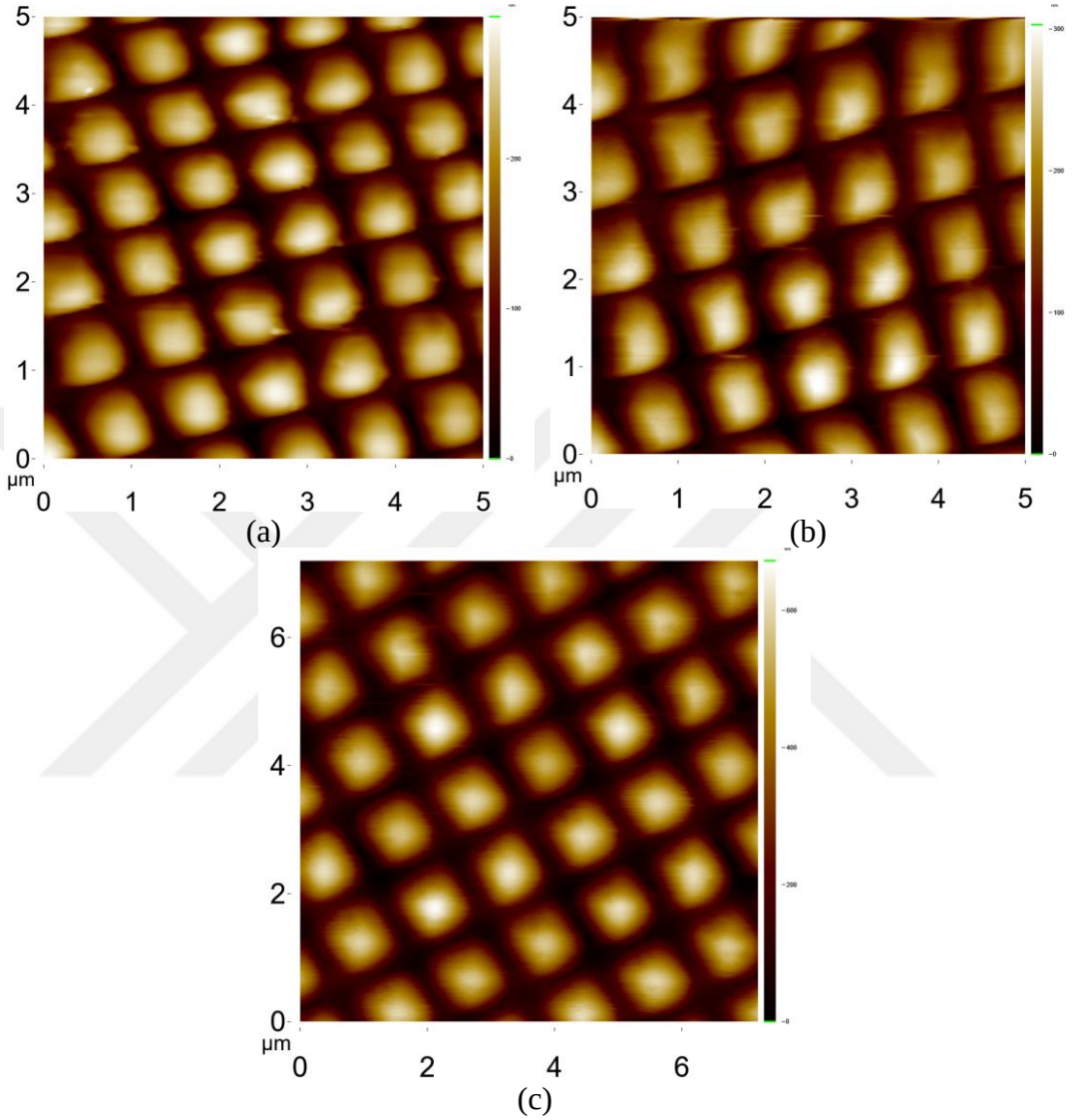

Figure 5. 14 AFM topography images of the iPhone camera chip in Tapping mode, (a) 225 K, (b) 77 K, (C) 1.3 K.

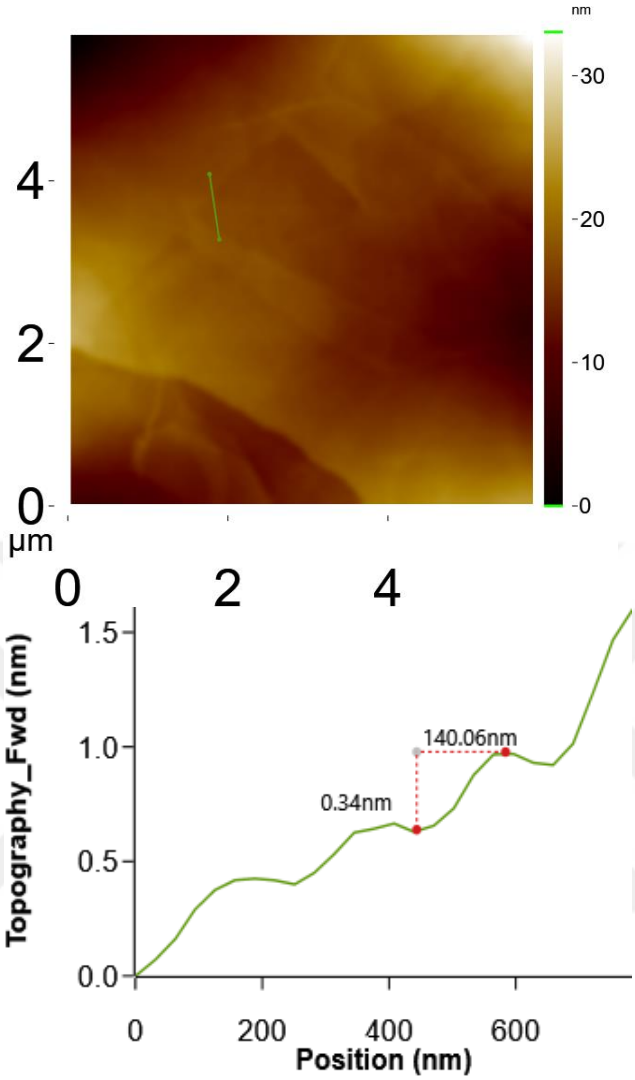

Figure 5. 15 Single-layer Graphene.

5.6. Conclusion

In this chapter, we demonstrate the reliability and functionality of the self-aligned LT-Fabry Perot AFM/MFM working at such a low temperature of 1.3 K in a newly installed cryostat. This is as well as a highly applicable isolation vibration platform design that eliminated the noises coming from the environment as well as the pulse tube refrigerator. Consequently, a better than 4 Å noise is obtained on the flat HOPG sample which represents the applicability of the isolation vibration platform design. This is sufficient for most MFM and AFM application which uses force microscope except the atomic resolution imaging or manipulation.

CHAPTER 6

FABRY PEROT INTERFEROMETER

6.1. Introduction

Technically Michelson fiber interferometer has such a limitation in obtaining the deflection with high sensitivity based on its intrinsic noise coming from shot noise. The laser shot noise is a kind of electronic noise that occurs by a finite number of photons that are carrying the energy and making statistical fluctuations in the measurements. The impact of striking the electrons on the photodiode is the generation of a photocurrent i.

$$i = S_{PD}P \tag{6.1}$$

i is proportional to the power P and S_{PD} is responsivity of photo photodetector. The average root-mean-squared variation of the current noise is given by:

$$\bar{i}_{shot} = \sqrt{2eS_{PD}P}\ \left(\frac{A}{Hz^{0.5}}\right) \tag{6.2}$$

e is the electronic charge, $1.6\text{x}10^{-16}$ C. If this current passes through a resistor, R_F, the average root-mean-squared variation of the voltage noise is given by:

$$\bar{v}_{shot} = \sqrt{2eS_{PD}PR_F}\ \left(\frac{V}{Hz^{0.5}}\right) \tag{6.3}$$

Obviously, increasing the optical power falling to the photodetector makes increase the signal sensitivity with the same ratio. Despite that, the shot noise will be increased by the ratio of the square root of the signal. Admittedly, the noise would be reduced by increasing optical power. As a result, the fiber Fabry Perot interferometer (FFPI) is developed according to this approach for the deflection sensor.

Principally, the FFPI is expected by two reflections, first from the fiber-air surface interface and then the backside of the cantilever. In order to have a reflection from the fiber surface, the end part of the fiber should be cleaved and then coated by TiO_2.

Coating the fiber provides multiple reflections and respectively the interference pattern in a much sensitive way that is detected by the photodetector.

There are few groups [69-74] that developed FFPI in the literature to obtain the high sensitivity deflection sensor for the atomic resolution image. Technically, coating the fiber end to increase the reflectivity and creating the parallel mirror system, adjusting the fiber in the best position regarding the cantilever as close as possible, as well as increasing the optical power falls on the photodetector are three critical points that are raised from FFPI design. To achieve these basics the end of the fiber is cleaved and then coated by suitable material, then a stick-slip approach mechanism is designed to adjust the fiber in the gap between the fiber and cantilever, and finally a fiber optic circulator in embedded inside the interferometer instead of a 2x2 coupler.

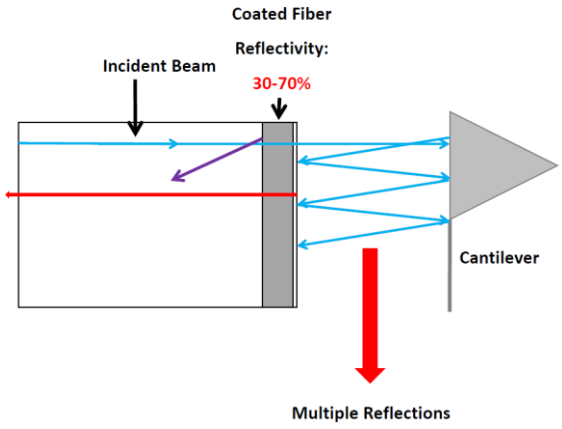

Figure 6. 1The fiber Fabry-Perot interferometer (FFPI) Schematic principal. To increases, the ratio of the internal reflection of the fiber and provides multiple reflections between two parallel mirrors the fiber end should be coated.

6.2. Fiber Coating

There are two major advantages of coating the fiber end from the optical view. Firstly, coating the fiber end increase the bare reflectivity from 3% to 39-70 %, and secondly, the cantilever and the fiber stays like two parallel mirror and multiple reflections can occur among these two plates. Consequently, utilizing the Fabry-Perot interferometer

helps to increase the finesse, visibility and slope values that contribute to high-resolution imaging.

6.2.1. Fiber coating with TiO_2

To achieve the higher interference slope as well as higher quality factor values the cleaved end of the fiber is coated with the reflectiveTiO_2 [75]. Firstly, to cleave the fiber end a high precision fiber cleaver (Fujikura CT-30) is used to get 2-3% bare reflectivity. The next step is dipping the fiber end for a few seconds in Titanium (IV) 2-ethylhexyloxide solution which is diluted by xylene with the ratio of one to five and then burning the fiber end with a propane torchlight. Within this process, the TiO_2 would be coated on the fiber and provides a reflectivity of 15-30%. [75]

6.3. Fiber Slider

The importance of the LT Fabry-Perot AFM/MFM is obtaining a higher slope of the interference pattern. This can be achieved by adjusting the fiber in the best position regarding the cantilever in a distance between the fiber and the cantilever. Normally in the design of the Michelson interferometer, the distance is fixed and around 30 μm with a Ø19 μm laser spot size which keeps a secure distance for the tip replacements.

As the fiber is adjustable, moving the fiber towards the cantilever makes a laser spot size smaller and be equal to the fiber core. Hence, the signal gain would be enhanced at the interferometer. This is where the misalignments of the fiber and cantilever which could be made by fabrication are such a drawback with causing a loss of the interferometer signal.

6.3.1. Fiber Slider Design for Low Temperature

To achieve this purpose with a certain functionality at low temperature, the MFM alignment holder is modified [49] in a way that fiber can slide toward the cantilever and vice-versa.

Therefore, the new design resulted in improved reliability of the fiber nano positioner that is established by three major impressions: (1) centralizing the cantilever tip at the

piezo tube; (2) enhancing the surface quality of the groves in which the ferrule is sliding; (3) increasing the inertial mass of the fiber holder.

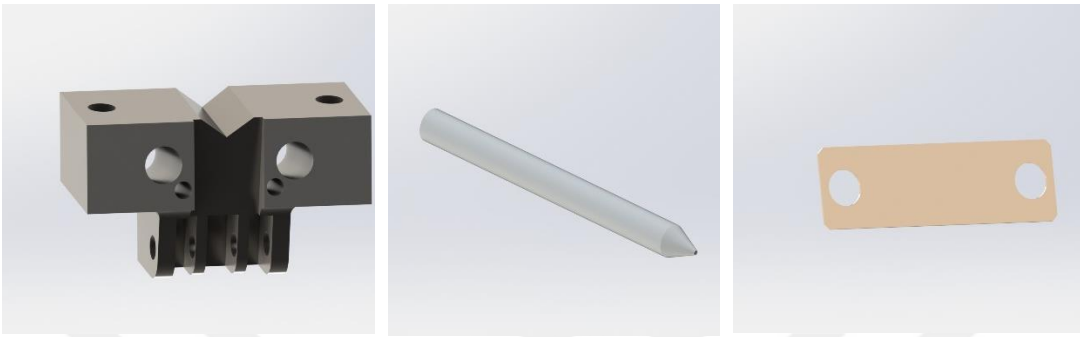

(a) (b) (c)

Figure 6. 2 Parts of the LT fiber slider. (a) MFM V-shaped holder, (b) ferrule tubing made of Zirconia, and (c) PhBr Leaf spring.

According to the design, the zirconia tubing with Ø1 mm which is polished, placed on the V-shape titanium holder part. Similarly, the titanium holder is perfectly polished to have a pure and smooth surface due to eliminating any struggle during the ferrule slid. The zirconia surface is sandwiched between the two-titanium surface and a leaf spring surface that press the tubing for replacement precisely in one direction toward the cantilever tip. All these processes have done under an optical microscope to have an absolute alignment and reach the minimum cavity gap as described earlier. The zirconia tubing has a 0.5 mm z-range gap to approach and retract to the cantilever. Obviously, the alignment maintains the same interferometer signal that obtains for repetitive motions.

The motion of the fiber is implemented by scanner piezo. Here the brass weight which is mounted on the zirconia tubing has a vital role in generating a momentum of the sliding part with an order of the magnitude. Without the additional weight on the ferrule, the fraction below the 125 K stops the ferrule motion. The PPS (Polyphenylene sulfide) part is designed to hold all the assembly and house the ferrule. Also, the ferrule

motion is restricted by the PPS design in retract motion and at the other end, the spring terminates the ferrule motion when the brass weight touches the leaf spring.

(a) (b)

Figure 6. 3(a) PPS holder, (b) Brass Weight (1.5 gr)

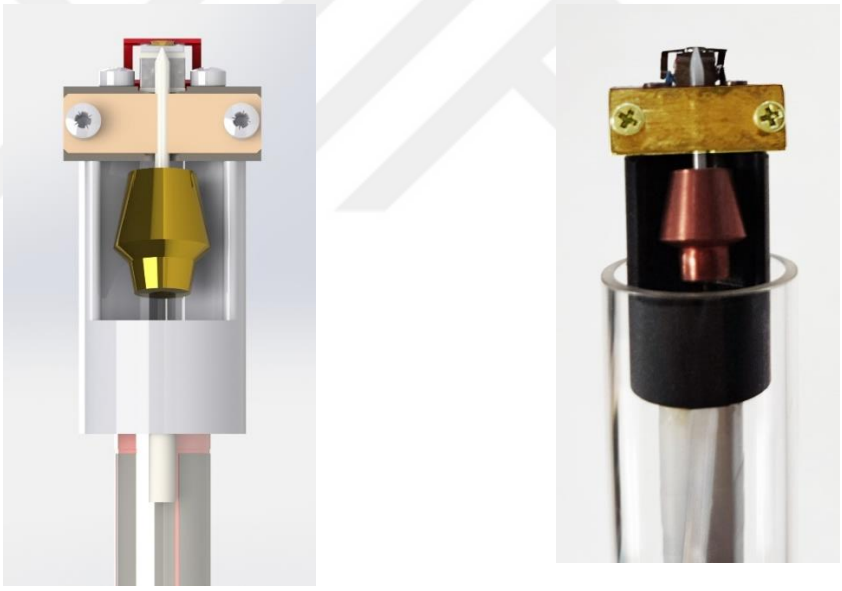

(a) (c)

Figure 6. 4 The V-shaped MFM holder schematic design which is assembled o top of PPS part at the end of the scanner piezo tube for sliding mechanism. (b) Scanner piezo, (c) Assembly of the microscope head.

6.3.2. Drive Mechanism of the Fiber Slider

The controller slider card applies the exponential slider pulse to the scanner piezo tube to retract and approach ferrule respect to the cantilever.

The figure below represents the ferrule tubing motion regarding the cantilever. Normally, the motion is continued till the fiber touches the cantilever, then the ferrule is retracted to find the maximum slope of the interference pattern.

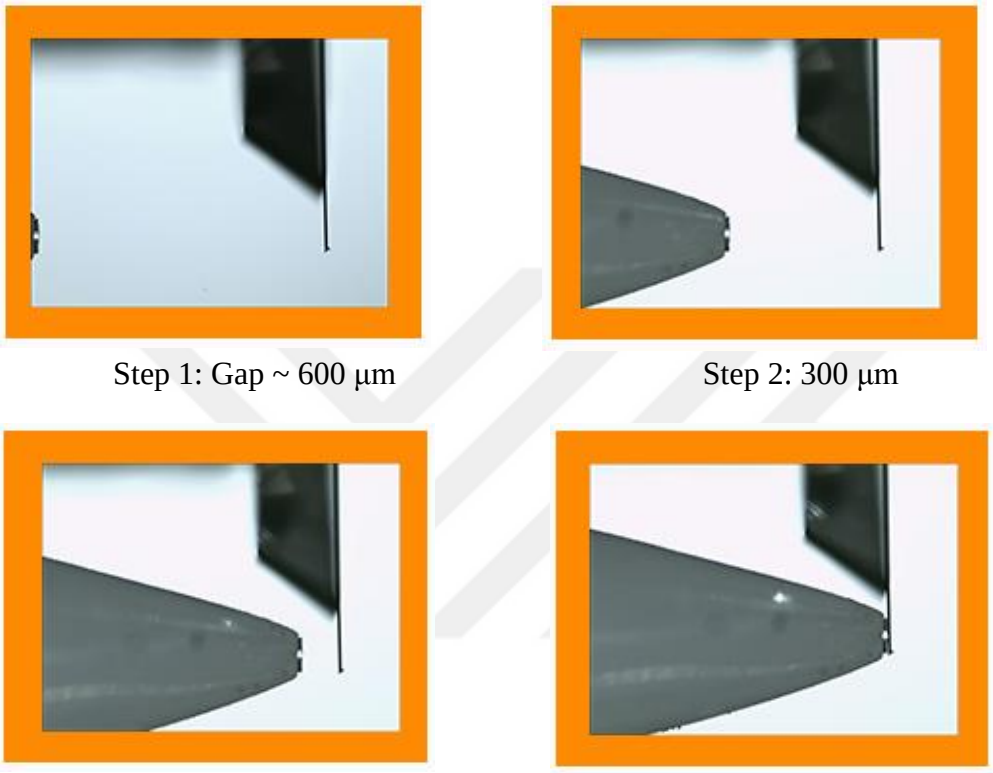

Figure 6. 5 Fiber Approach by Stick-Slip Approach Mechanism.

6.3.3. Testing the Slip-Stick Mechanism at Low Temperature

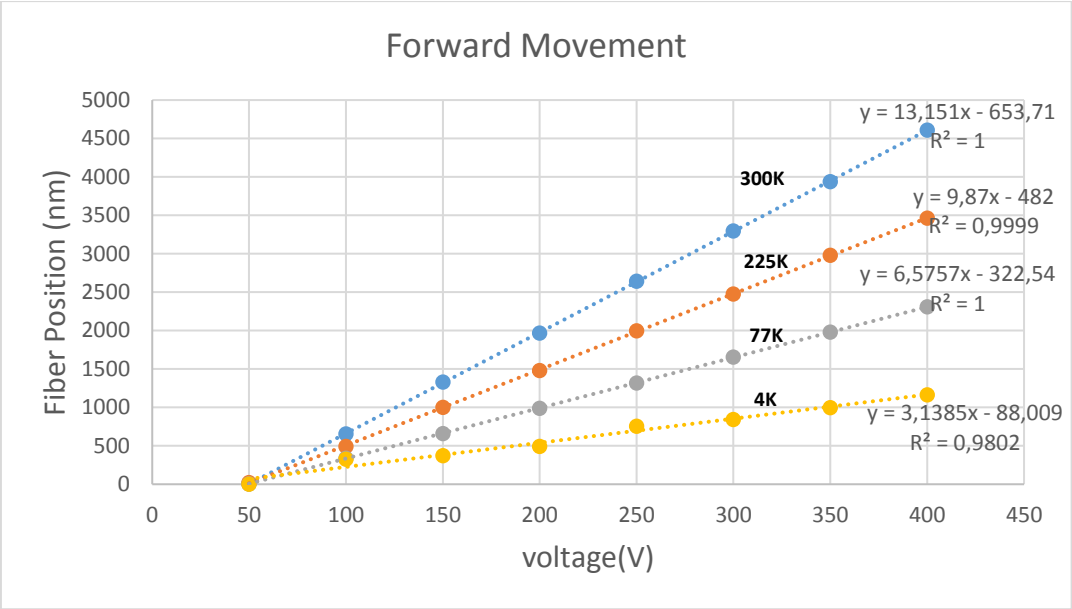

(a)

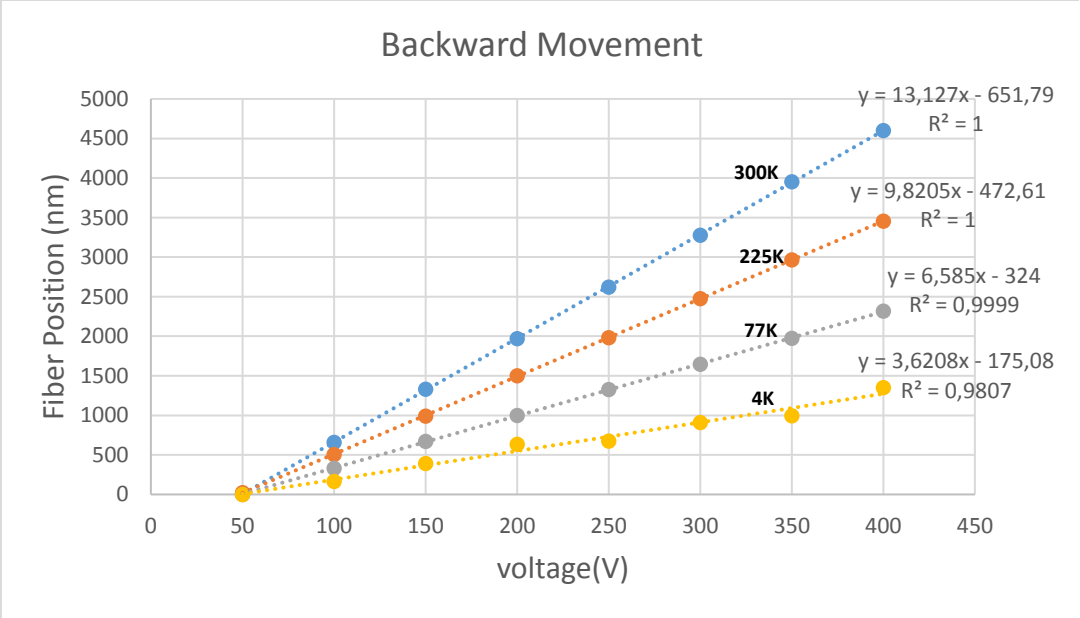

(b)

Figure 6. 6Slider Piezo Step Length in 300K, 225K, 77K, 4K. (a) Forward motion, (b) Backward motion.

The slider mechanism is examined and optimized in all operation temperature rages successfully and represents a fully linear motion. Normally the applied voltage to the

slider should be increased by decreasing the temperature as the piezo capacitance is dropping by the temperature drops.

The step sizes are tunable with adjusting the pulse height of the slider and controlling the applied voltage in the software. The figure below presents an example of the ferrule motion. The pattern was moved with a single approach step.

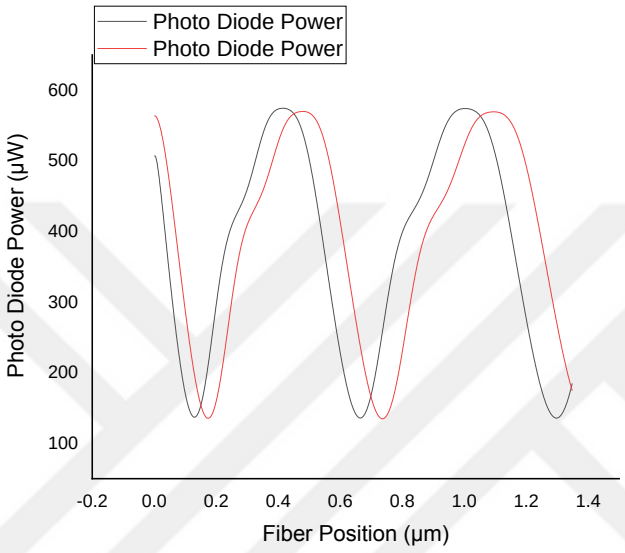

Figure 6. 7 Measuring fiber step on the interference pattern at 300 K. A single step with 300 V height slider pulse applied for approaching. The red plot is the interference pattern of the fiber position after one step moved toward the cantilever which is measured 74 nm displacement.

6.3.4. Slope and Visibility Behavior vs gap distance between the Cantilever and Fiber

As this is already mentioned, decreasing the gap makes the smaller laser spot and increased signal gain that aims to increase the slope value of the interference pattern. Here, the type of the cantilever is also important in increasing the reflectivity which results in the higher slope value. Hence, each cantilever can provide a specific maximum value of the slope. Besides, the visibility has unique behavior with a maximum of 1 that does not change depends on the cantilever.

According to the unique behavior of the visibility which is measured and plotted at 300 K, the gap distance can be determined based on the plot with visibility value. Therefore, in order not to damage the cantilever tip in cold temperature inside the cryostat, firstly, the visibility and also the max slope value was monitored and plotted, then during the approach toward the cantilever, the distance could be calculated and in a close distance where the slope is maximum, the scanning operation was started.

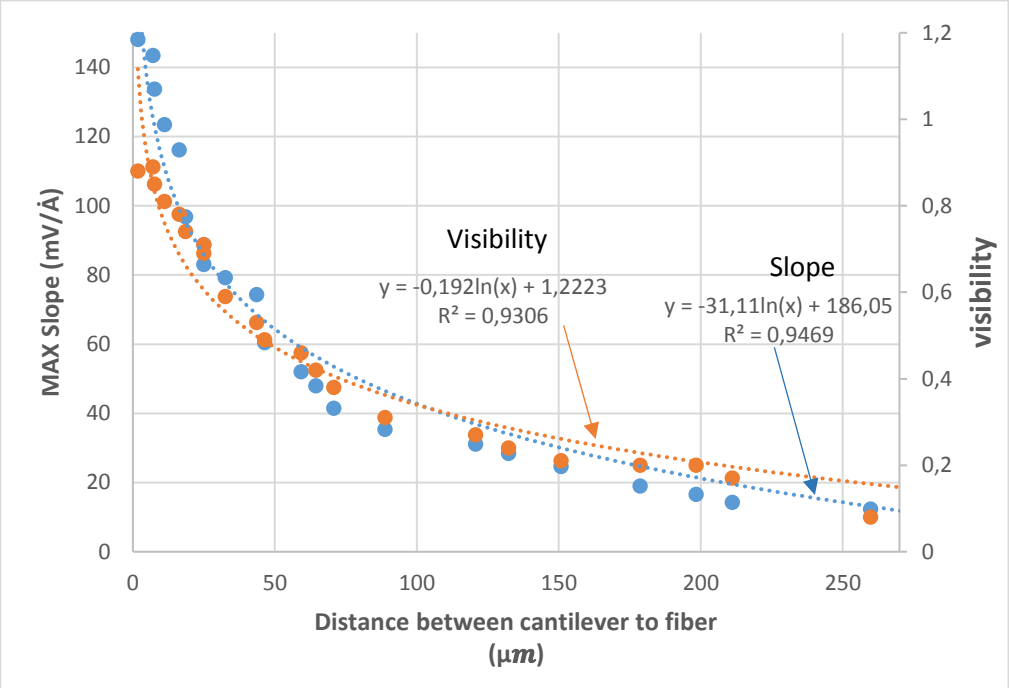

Figure 6. 8 Slope and Visibility behavior vs gap distance between the cantilever and fiber.

6.3.5. Fiber Optic Circulator

Ideally, to increase the measurement precision by means of increasing the power which is falling to the signal photodiode at the interferometer, it would be better to use most parts of the laser beam for measuring the cantilever deflection. Typically, the standard Michelson fiber interferometer uses 2x2 50% coupler to divide the laser beam. One is used as a reference at the photodiode to monitor the power and the second one is employed to measure the deflection.

To full fill this purpose the fiber optic circulator can be used which possibly utilizes 100% power. This is a non-reciprocal optical device with three ports that allow the light to travel just in one direction.

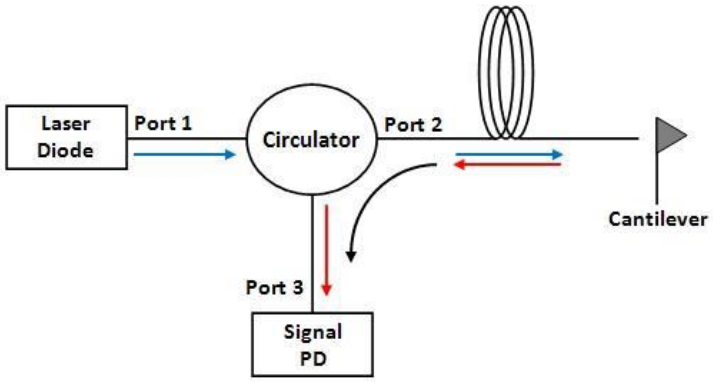

Figure 6. 9 fiber optic circulator diagram for fiber interferometer [64].

The entering laser to port 1 will exit port 2, and in the way back the entering signal to the port 2 will exit port 3.

Theoretically, utilizing the circulator [64] in the interferometer will enhance the optical power 4 times that falls into the signal photodetector. This issue increases the slope value, expectedly, in the same ratio.

Table 6. 1 The fiber optic circulator and the 2x2 coupler Comparison.

	Slope (mV/Å)	*Power in the Fiber (mW)*
Circulator	120	3.0
2x2 50% Coupler	30	1.5

6.4. Fiber Fabry-Perot interferometer

The cleaved and coated end of the single-mode fiber will normally reflect 30-70% of the laser light in the LT AFM/MFM system. The rest of the light passes the fiber end to hit the cantilever back surface. The multiple reflections occur between these two parallel mirrors. And increase the optical power on the photodetector as well as increasing the internal reflectivity.

By sending a laser beam (with electromagnetic field $\vec{E}_{inc}$) to fiber, part of the beam is reflected back from the fiber end ($\vec{E}_r$), and the rest passes the fiber end to the cantilever. Then the rest beam is reflected again from the cantilever back and goes through the fiber to photodetector ($\vec{E}_s$).

Consequently, the photodetector takes the absolute value of total electromagnetic fields as current.

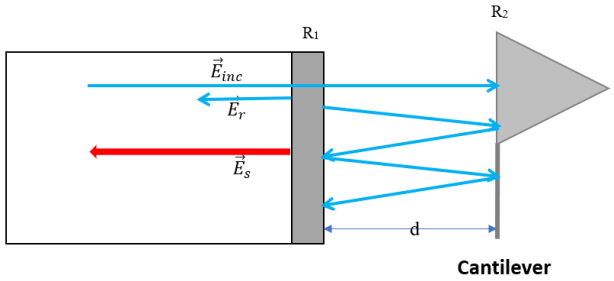

Figure 6. 10 schematic design of the fiber-cantilever reflectivity. $\vec{E}_{inc}$, $\vec{E}_r$, $\vec{E}_s$ are respectively the incident beam, the fiber surface reflected beam, the summation of the cantilever and fiber reflected beam, R_1 fiber surface reflectivity, R_2 cantilever Reflectivity.

$$\vec{E}_{inc} = \vec{E}e^{j(\omega t - kz)} \tag{6.4}$$

$$\vec{E}_r = \vec{E}e^{j(\omega t + kz)} \tag{6.5}$$

$$\vec{E}_s = \vec{E}e^{j(\omega t + kz + 2kd)} \tag{6.6}$$

$$\left\|\vec{E}_{tot}\right\|^2 = \left\langle \vec{E}_{tot} \middle| \vec{E}^*_{tot} \right\rangle \tag{6.7}$$

$$\rightarrow \left\|\vec{E}_{tot}\right\|^2 = \vec{E}_s^2 + \vec{E}_r^2 + 2\vec{E}_r\vec{E}_s\cos(2kd) \tag{6.8}$$

$$\left\|\vec{E}_{tot}\right\|^2 \propto I \tag{6.9}$$

$$\xrightarrow{\text{As a result}} I = I_r + I_s + 2\sqrt{I_r I_s}\cos(2kd) \tag{6.10}$$

$$\begin{cases} I_{max} = I_r + I_s + 2\sqrt{I_r I_s} \\ I_{min} = I_r + I_s - 2\sqrt{I_r I_s} \end{cases} \tag{6.11}$$

The I_r, I_s are the current generated by fiber surface reflected beam, and fiber surface and the cantilever surface reflected beam.

We can define visibility and the average of the current:

$$V = \frac{I_{max} - I_{min}}{I_{max} + I_{min}}, \tag{6.12}$$

$$i_0 = (I_{max} + I_{\min})/2 \tag{6.13}$$

On the other hand, considering P_0, fiber optical power, with fiber surface reflectivity of R_1, and cantilever surface reflectivity R_2, we can obtain that :

$$P_r = P_0 R_1 \quad , and \quad P_s = P_0(1 - R_1)^2 R_2 \tag{6.14}$$

Additionally,

$$I_r \propto P_0 R_1 \quad , and \quad I_s \propto P_0(1 - R_1)^2 R_2 \tag{6.15}$$

P_r, P_s are optical power of fiber surface reflected beam, the optical power of the fiber surface and the cantilever surface reflected beam.

As a result, the visibility can be written as:

$$V = \frac{2(1 - R_1)\sqrt{R_1 R_2}}{R_1 + (1 - R_1)^2 R_2} \tag{6.16}$$

And define the sensitivity:

$$sensitivity = \frac{4\pi}{\lambda} V \tag{6.17}$$

Based on the reflection coefficient of the Fabry-Perot interferometer we can model the signal and find the most sensitive position which is the quadrature points d= λ/8, 3λ/8, 5λ/8 and the slope is much greater than the Michelson one.

$$Reflection\ Coefficient = \left(\frac{4\mathrm{R} \sin^2 \frac{2\pi}{\lambda} d}{(1 + R^2) + 4R \sin^2(\frac{2\pi}{\lambda} d)} \right) \tag{6.18}$$

Defining F, the coefficient of finesse:

$$F = \frac{4R}{(1 - R)^2} \tag{6.19}$$

The reflection coefficient ould be:

$$Reflection\ Coefficient = \left(\frac{\mathrm{F} \sin^2 \frac{2\pi}{\lambda} d}{1 + F \sin^2(\frac{2\pi}{\lambda} d)} \right) \tag{6.20}$$

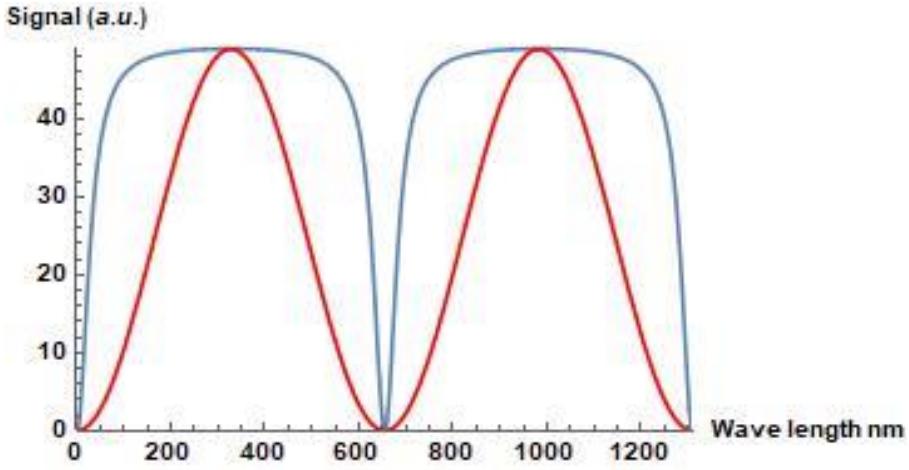

Figure 6. 11 The Fabry-Pérot interferometer (Blue) and Michelson (Red) Modeling for 1,310 nm wavelength.

Figure 6.11 shows the modeled interference signals of both interferometer types. Here the value of V is around 0.9 and finesse of 50. Obviously, the Fiber Fabry-Pérot interferometer has a higher slope value and higher sensitivity at the deflection sensor.

6.5. Experimental Results

6.5.1. Fabry-Perot Interferometer signal

The signal of the Fabry-Perot interferometer with fiber optic circulator in different drive laser power is presented in Figure 6.12 Ideally, the circulator will enhance the power at the signal PD about 4 times. The relationship of the laser power at the quadrature point in the signal PD is presented in Figure 6.13. As it is exposed there is a linear relationship between the drive laser power and the quadrature point power.

The maximum slope of the 2x2 fiber optic coupler which is achieved is ~30 mV/Å while fiber-optic circulator reaches ~140 mV/Å.

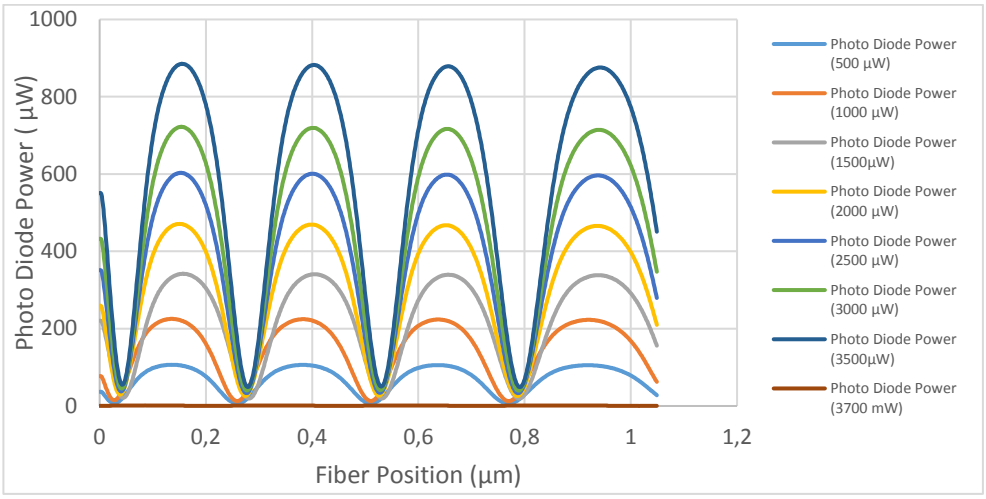

Figure 6. 12 Different drive laser power in the Fibre Fabry-Perot interferometer at 300 K.

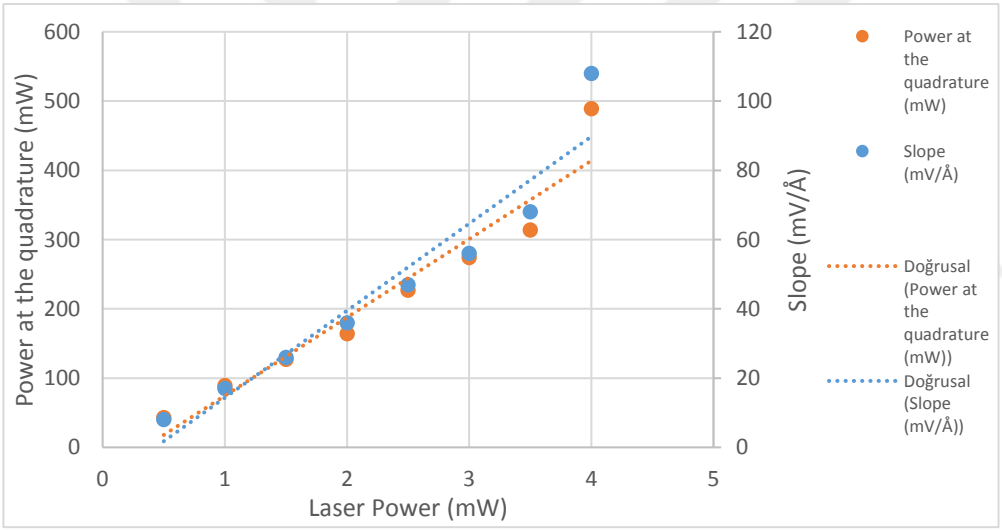

Figure 6. 13 Representation of the Linear relationship between the interference slope & Average power at quadrature point Vs drive laser power @ 300K.

The table below represents the difference interference slope obtained by different interferometers.

Table 6. 2 Fabry-Perot and Michelson interferometers Comparison

	Slope (mV/Å)	*Visibility*	*Power (mW)*	*Finesse*
Fabry-Perot	148	0.9	3.5	4.4
Michelson	30	0.73	3.5	2.74

6.5.2. AFM Images:

To check the functionality of the microscope different samples in various temperatures were recorded. Initially, the AFM image of the calibration grating Figure 6.14 is recorded in 300 K. The interference pattern with a slope value of ~60 mV/Å was used for this experiment. And the Q factor is 234.

In Figure 6.15, 6.16 depicts the tapping mode AFM image of the Graphite in both 300 K and 77 K with interference slope value of 52 mV/Å and Q factor of 482.

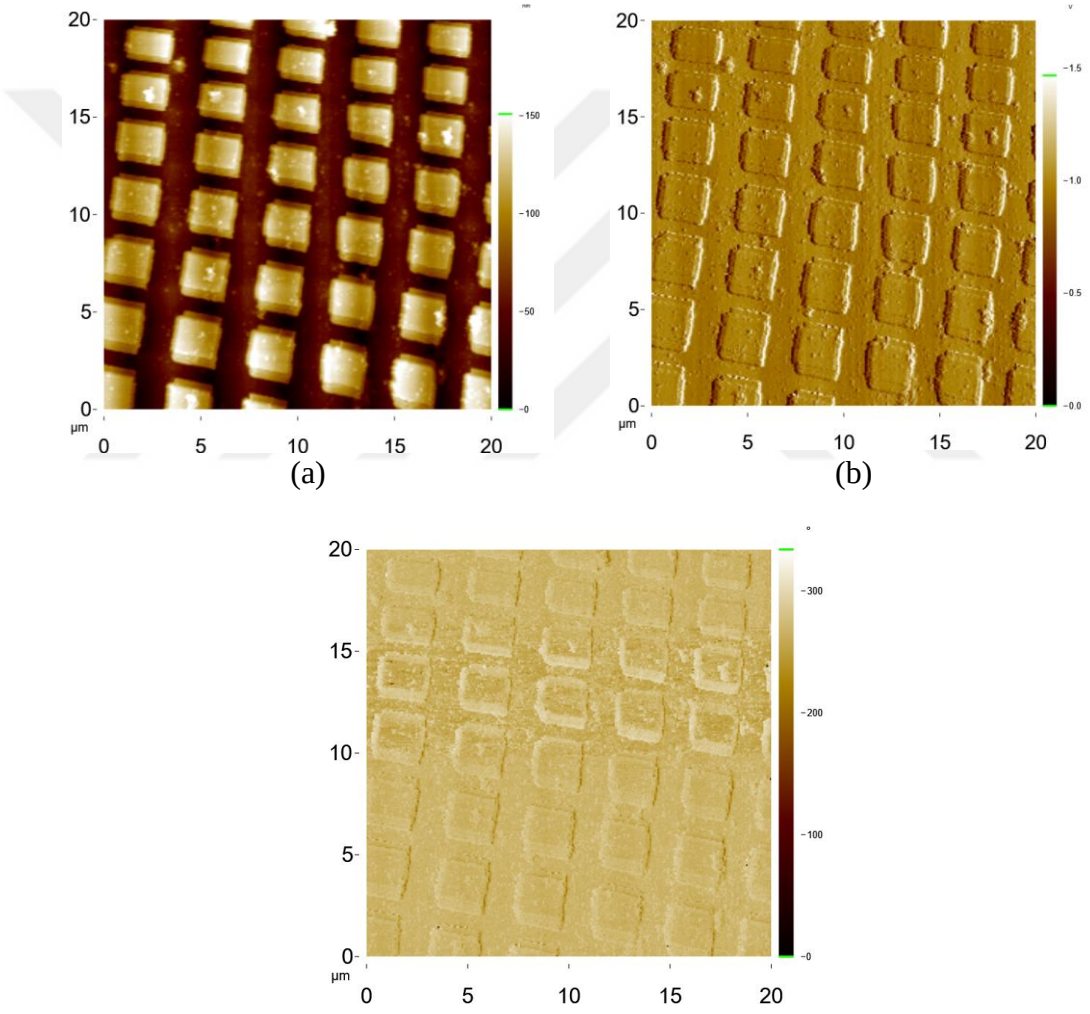

Figure 6. 14 AFM image of the grating sample in Tapping mode at 300 K. (a) Sample Topography, (b) Amplitude (Feedback) and, (c) Phase images.

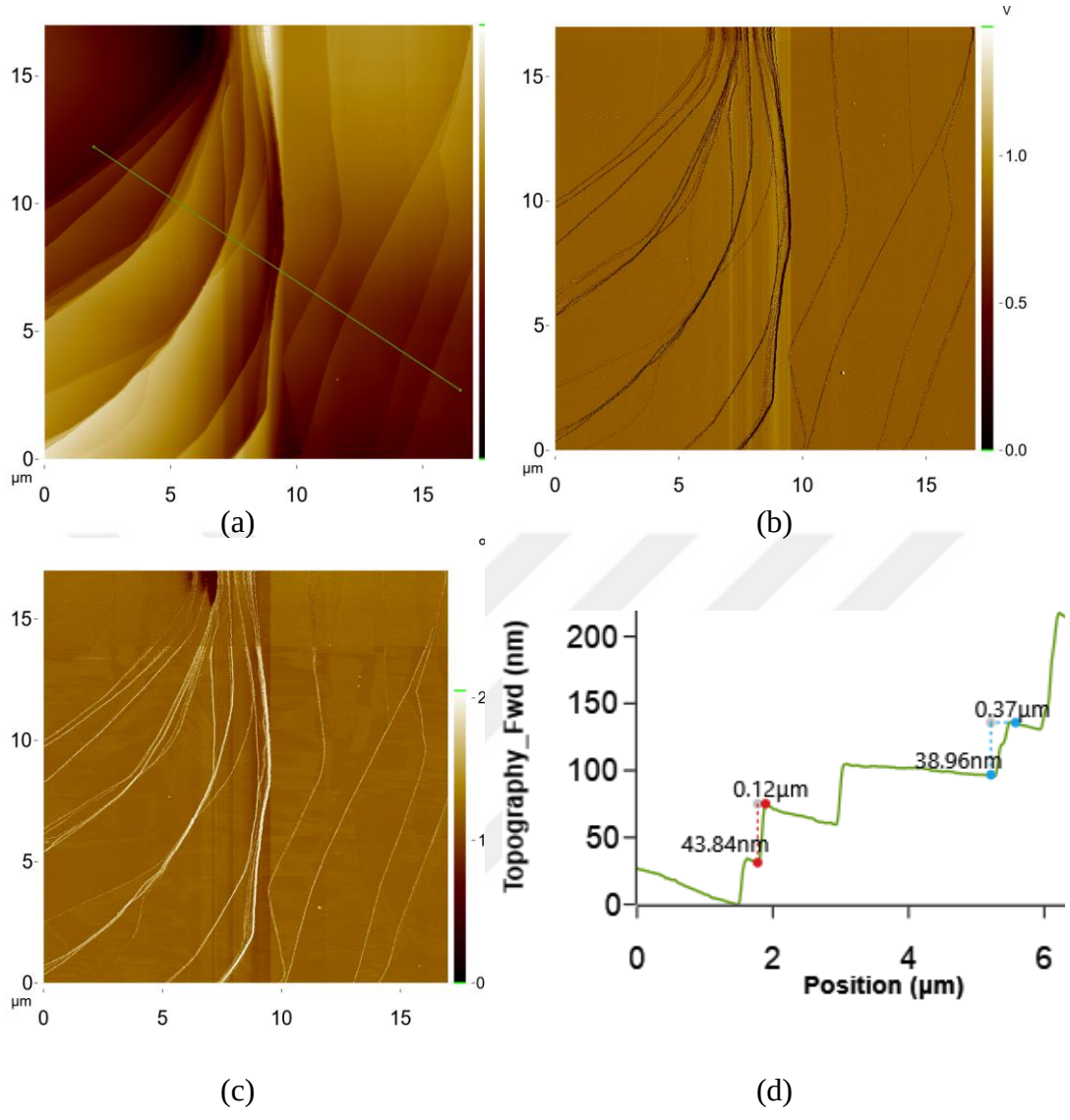

Figure 6. 15 AFM image of the Graphite in Tapping mode at 300 K. (a) Topography, (b) Amplitude (Feedback). (c) Graphite layers size.

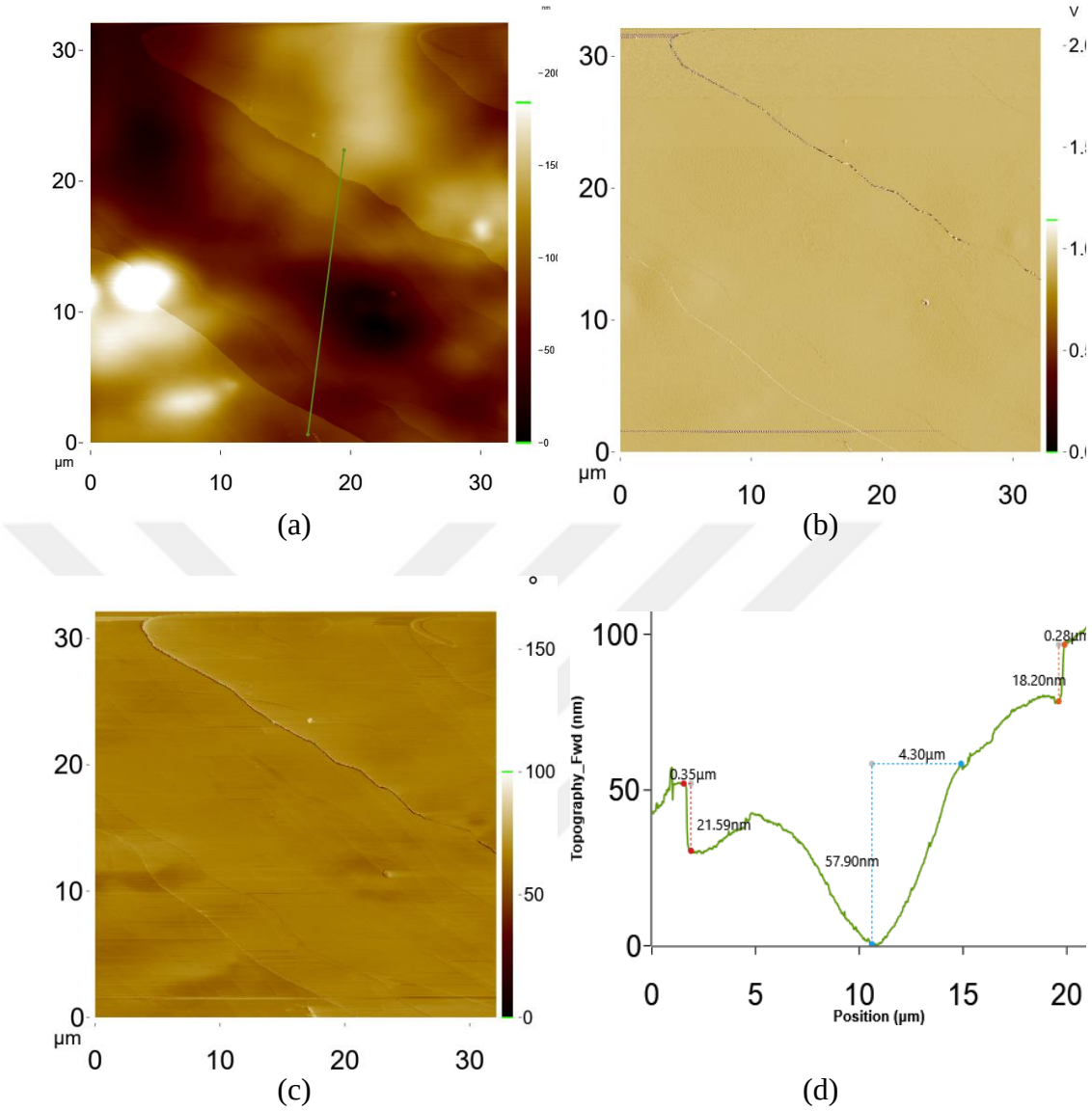

Figure 6. 16 AFM image of the Graphite in Tapping mode at 77 K. (a) Sample Topography, (b) Amplitude (Feedback). (c) Graphite layers size.

Figure 6.17 also is the tapping mode AFM image of the Mika which shows the single layers in 300 K.

Reaching to the Mika single layer image represents the high resolution as well as the functionality of the microscope in AFM mode.

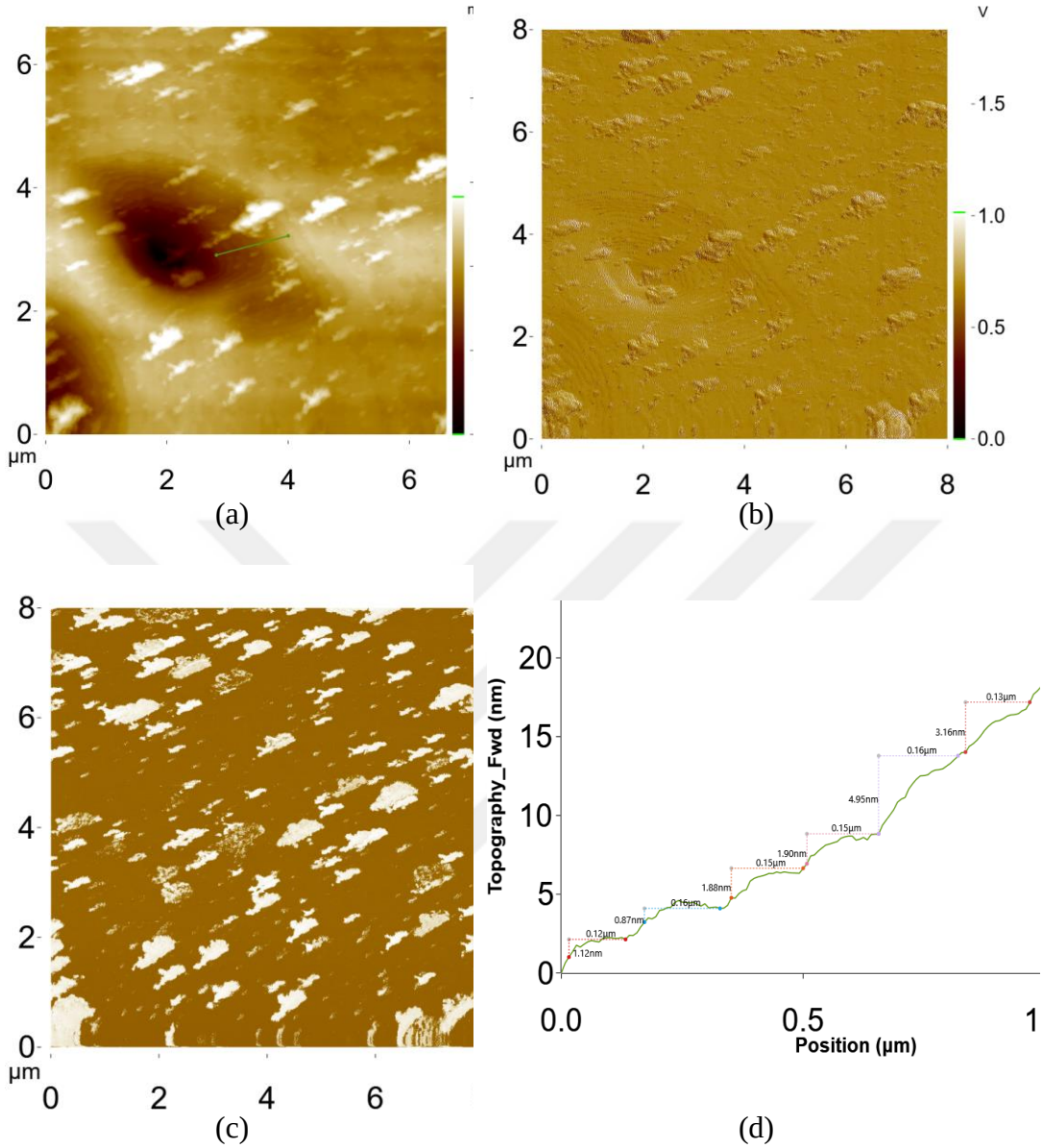

Figure 6. 17 Tapping mode AFM image the Mika at 70 K. (a) Topography, (b) Amplitude (Feedback). (c) Mika single layers.

6.5.3. MFM Images

The ability of the microscope in measuring the magnetic materials is tested at various temperatures. For the MFM application, we recorded the magnetic properties of the Sony hi8 tape as well as the 80 GB hard disk sample.

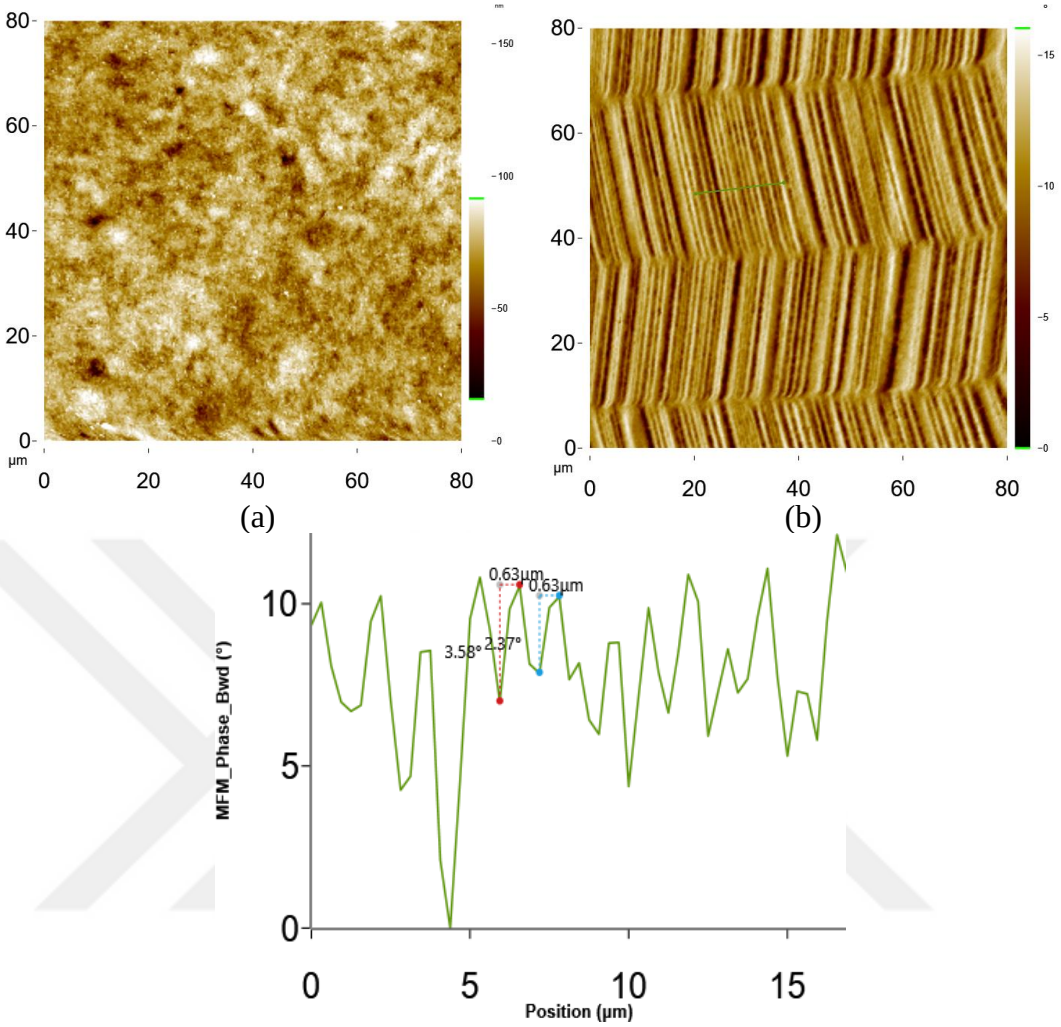

Figure 6. 18 MFM image of the Sony hi8 type sample at 77 K: (a) Topography and (b) Magnetic image. Lift-off amount was 100 nm. (c) Cross-section of the magnetic image.

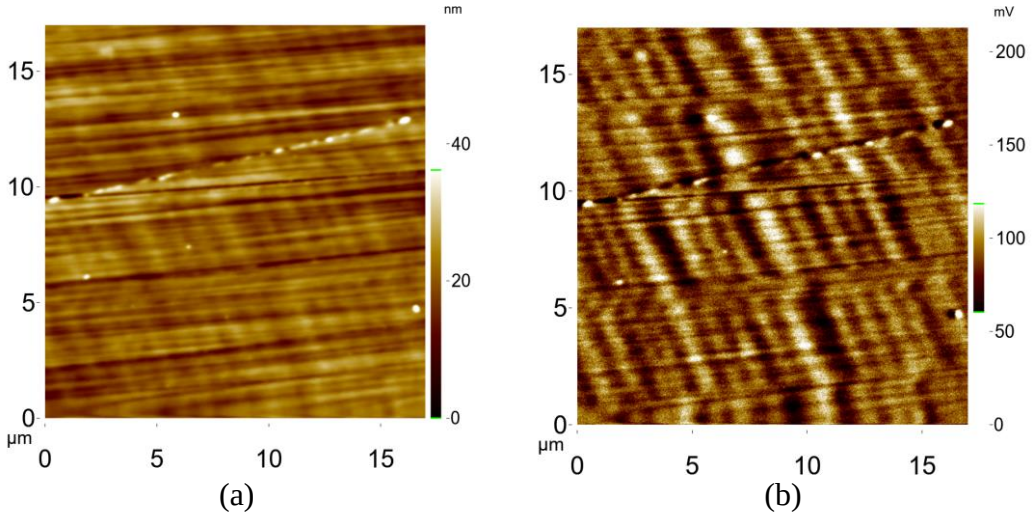

Figure 6. 19 MFM image of the 80 GB/Platter hard disk sample at 300 K: (a) Topography and (b) Magnetic image. Lift-off amount was 85 nm.

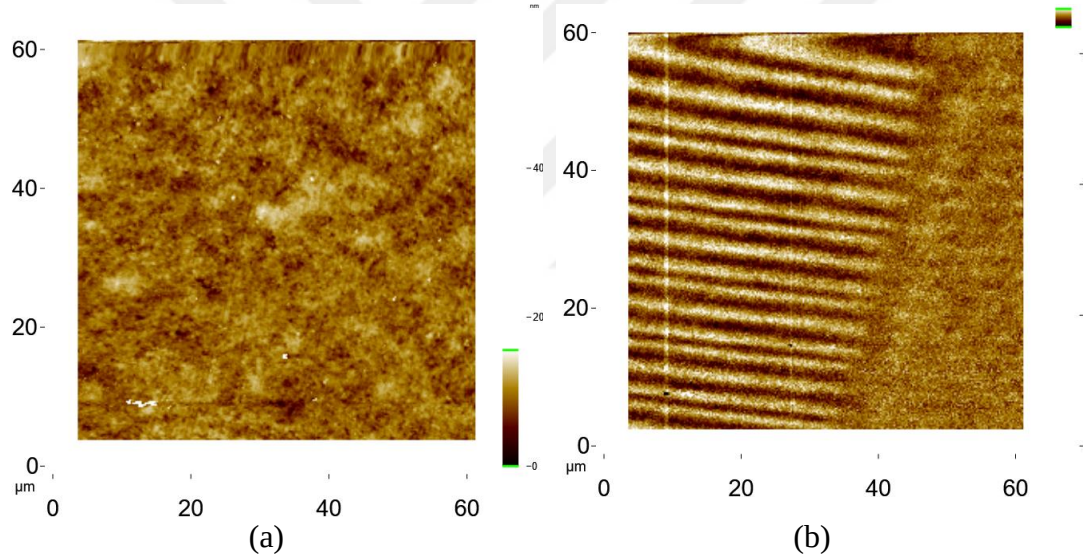

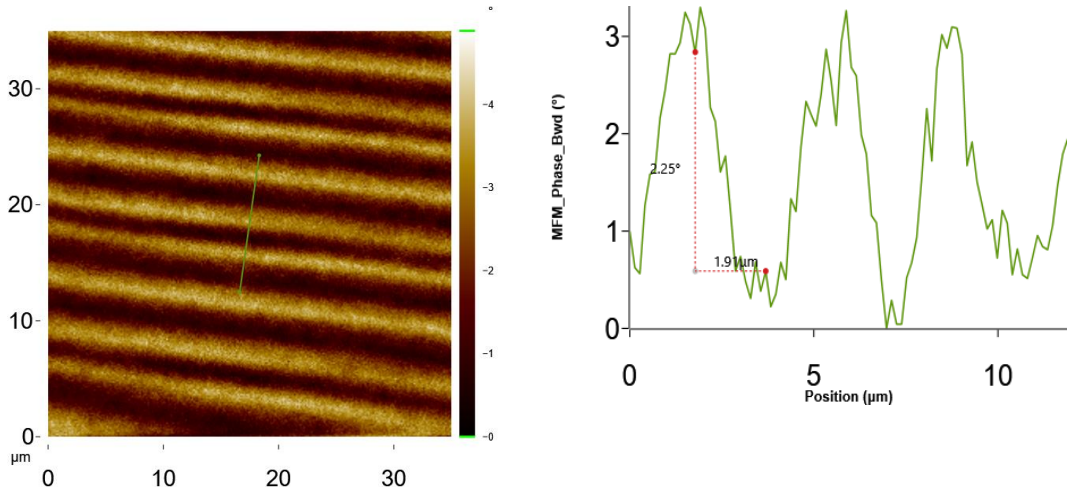

(c) (d)

Figure 6. 20 MFM image of out of plane magnetic field on the floppy disk surface (a)Topography, (b) MFM image with 300 nm Lift-off value at 300K, (c, d) Cross section of magnetic image measurements.

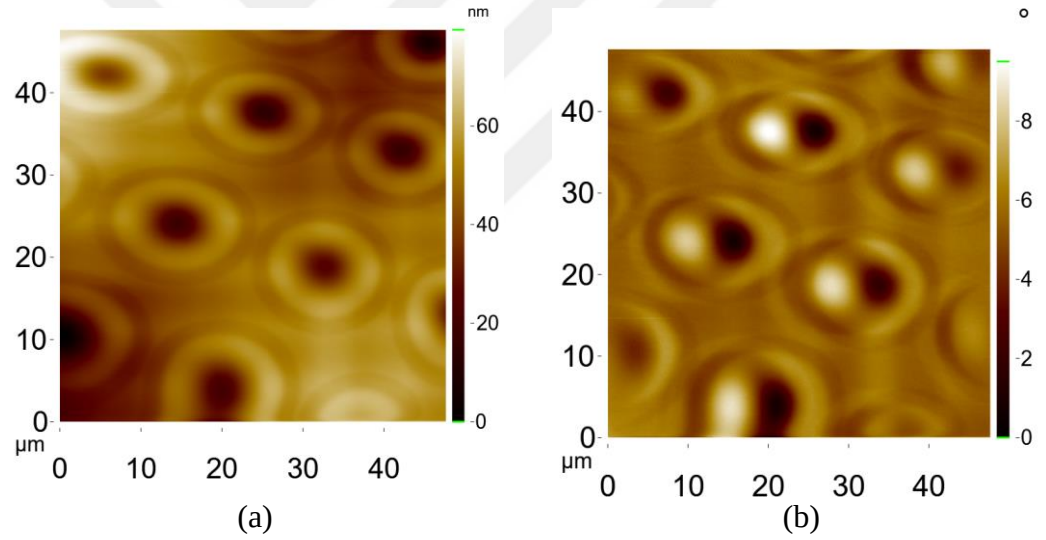

(a) (b)

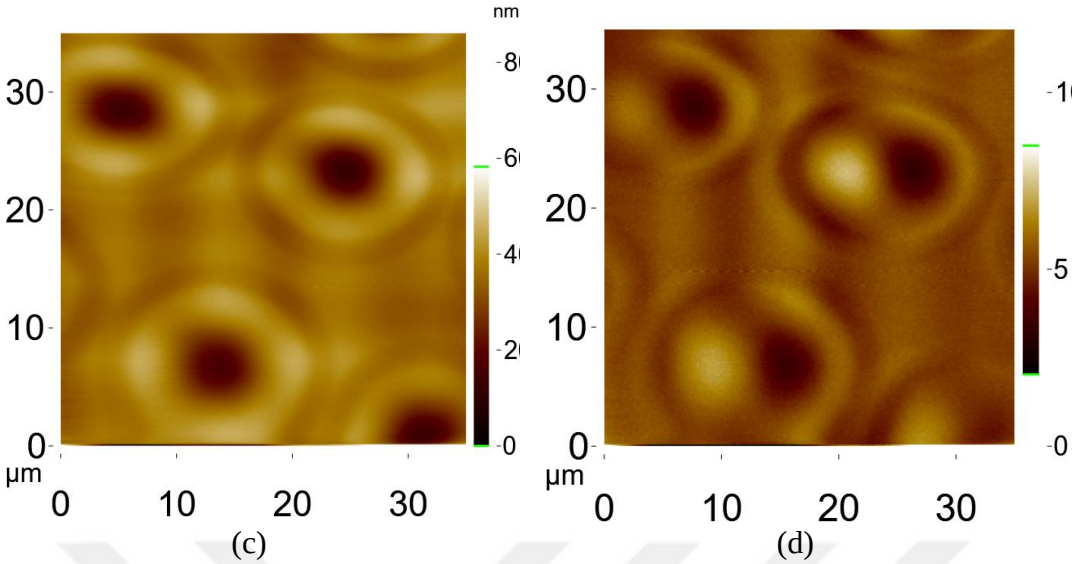

Figure 6. 21 Large laser bumps at the no load- unload ramps on the hard disk surface also known as the landing zone for the head of the hard disk. (a, b) Topography, and MFM image at 300 K, (c, d) Topography and MFM image at the 77 K.

6.5.4. Conclusions

We redesign and improve the LT Fabry-Perot AFM/MFM head by means of increasing the reliability of fiber tubing movement in various temperature ranges of 300 K to 1.3 K. The functionality of slip-stick fiber slider is established and the new design provides a better resolution with obtaining the higher interference slope value. The new coating material benefits to enhance the reflectivity from the fiber surface and implementing the mirror-like surface between the fiber end and cantilever in order to increase the laser gain and lose much less. This is as well as utilizing the circulator in the interferometer which contributes much less loss of the laser.

CHAPTER 7

CONCLUSION

In this thesis, we demonstrated a self-aligned low-temperature Fabry-Perot atomic force/ magnetic force (LT-AFM/MFM) microscope with the ability of operation in different temperatures from 300 K to 1.3 K. The alignment-free design provides the compatibility of using different types of cantilevers as well as eliminating time-consuming procedure for aligning the cantilever respect to the fiber with complicated alignment setup. This microscope is exclusively designed for low-temperature experiments and tried to reduce the outer dimension to be completely compatible with various cryogenic systems.

For enhancing the reliability of the microscope operation, the head is redesigned and modified. To achieve higher performance of fiber movement specifically in low temperatures, the parts are altered and fully optimized. And the fiber end is coated by TiO_2 in order to increase the initial reflectivity from the fiber end and the laser gain in the photodetector.

Redesigning the fiber nano positioner, enhancing the accuracy and optimizing the parts provides reliable slip-stick operation in various temperatures and increased fiber reflectivity to gain a higher slope value of the interference pattern.

The table below represents the critical Slope, Visibility and Finesse value where the fiber positioned in a 1μm to the cantilever.

Table 7. 1 Slope, Visibility and Finesse value of old design Microscope

Old Design	Power in the Fibre (mW)	Slope (mV/Å)	Visibility	Finesse
Michelson Interferometer	3.5	6	0.43	1.81
Fabry-Perot Interferometer	3.5	120	0.89	4.31

After developing and enhancing the microscope design, with the newly manufactured parts, we were able to reach the higher values and increase the lateral resolution. The table below shows the enhanced values by the new design where the fiber stands in 1μm to the cantilever.

Table 7. 2 Slope, Visibility and Finesse value of old design Microscope

New Design	**Power in the Fibre (mW)**	**Slope (mV/Å)**	**Visibility**	**Finesse**
Michelson Interferometer	3.5	19	0.73	1.74
Fabry-Perot Interferometer	3.5	148	0.90	4.40

To decrease the floor noise and pulse tube vibration during the low-temperature experiments inside the cryostat, the isolation vibration platform is designed to decouple the noise. With this design, we eliminate the noise to Å range. And reaching the single layer, Graphene denotes the higher resolution and functionality of the microscope.

Additionally, the Fabry-Perot interferometer was employed to measure the cantilever deflection with remarkably high sensitivity. This interferometer has ultra-low noise around 8 fm/$Hz^{1/2}$ at room temperature and around 1 fm/$Hz^{1/2}$ at 1.3 K which allows measuring the cantilever spring constant with the help of spectral noise density. The ultra-low noise of the deflection sensor is a magnificent feature to measure the magnetic media down to a few nm magnetic resolution.

Measuring the cantilever spring constant with fitting the calculated Brownian noise plot with spectral noise density is an important and new method that provides precision to estimate cantilever spring value.

REFERENCES

[1] Hoffmann, R.; Baratoff, A.; Hug, H. J.; Hidber, H. R.; von Lohneysen, H.; Guntherodt, H. J. G.,Mechanical manifestations of rare atomic jumps in dynamic force microscopy. Nanotechnology 2007, 18 (39), 395503.

[2] Crampton, N.; Yokokawa, M.; Dryden, D. T. F.; Edwardson, J. M.; Rao, D. N.; Takeyasu, K.; Yoshimura, S. H.; Henderson, R. M., Fast-scan atomic force microscopy reveals that the type III restriction enzyme EcoP151 is capable of DNA translocation and looping. Proceedings of the National Academy of Sciences of the United States of America 2007, 104 (31), 12755–60.

[3] Ando, T.; Uchihashi, T.; Kodera, N.; Yamamoto, D.; Taniguchi, M.; Miyagi, A.; Yamashita, H.,High-speed atomic force microscopy for observing dynamic biomolecular processes. Journal of Molecular Recognition 2007, 20 (6), 448–58.

[4] Yokokawa, M.; Yoshimura, S. H.; Naito, Y.; Ando, T.; Yagi, A.; Sakai, N.; Takeyasu, K., Fast scanning atomic force microscopy reveals the molecular mechanism of DNA cleavage by Apal endonuclease. IEE Proceedings – Nanobiotechnology 2006, 153 (4), 60–66.

[5] Becker, H.; Bender, O.; Bergmann, L.; Rost, K.; Zobel, A. Apparatus for measuring surface irregularities. United States Patent number: 2728222, 1955.

[6] EATON, Peter; WEST, Paul. *Atomic force microscopy*. Oxford university press, 2010.

[7] Young, R.; Ward, J.; Scire, F., The topografiner: an instrument for measuring surface microtopography. Review of Scientific Instruments 1972, 43 (7), 999–1011.

[8] G. Binning, H. Rohrer, Ch. Gerber and E. Weibel, Tunneling Through a Controllable Vacuum Gap, *Applied Physics Letter*, 40, 178, **1982.**

[9] G. Binning, H. Rohrer, Scanning Tunneling Microscopy, *Helvetica Physica Acta*, 55, 726-735, **1982.**

[10] G. Binning, H. Rohrer, Ch. Gerber and E. Weibel, Surface Studies by Scanning Tunneling Microscopy, *Physical Review Letter*, 49 (1), 57-61, **1982**.

[11] Y. Yin, M. Zech, T. L. Williams and J. E. Hoffman, Scanning Tunneling Microscopy and Spectroscopy on Iron-Pnictides, *Physica C: Superconductivity*, 469 (9-12), 535-544, **2009.**

[12] Kano, S., Tada, T., & Majima, Y. (2015). Nanoparticle characterization based on STM and STS. *Chemical Society Reviews*, *44*(4), 970-987.

[13] Binnig, G.; Rohrer, H., Scanning tunneling microscopy. Helvetica Physica Acta 1982, 55 (6), 726–35.

[14] Binnig, G.; Rohrer, H., Scanning tunneling microscopy. Surface Science 1983, 126 (1–3), 236–44.

[15] F. F. Abraham, I. P. Batra, Theoretical Interpretation of Atomic Force Microscope Images of Graphite, *Surface Science*, 209, **1989.**

[16] R. G. Miller, P. J. Bryant, Atomic Force Microscopy of Layered Compounds, *Journal of Vacuum Science & Technology A*, 7, 2879, **1989.**

[17] T. R. Albrecht, P. Grütter, D. Horne and D. Rugar, Frequency Modulation Detection Using HighQ Cantilevers for Enhanced Force Microscope Sensitivity, *Journal of Applied Physics*, 69 (2), 668-673, **1991.**

[18] Q. Zhong, D. Innis, K. Kjoller, V. B. Elings, Fractured Polymer/Silica Fibre Surface Studied by Tapping Mode Atomic Force Microscopy, Surface Science, 290 (1-2), L688-L692, **1993.**

[19] S. N. Magonov, V. Elings, M.-H. Whangbo, Phase Imaging and Stiffness in Tapping-Mode Atomic Force Microscopy, *Surface Science Letters*, 375, L385-L391, **1997.**

[20] Y. Martin and H. K. Wickramasinghe, Magnetic Imaging by Force Microscopy With 1000 Å Resolution, *Applied Physics Letter*, 50 (20), 1455-1457, **1987**.

[21] C. Israel, W. Wu and A. de Lozanne, High-Field Magnetic Force Microscopy as Susceptibility Imaging, Applied Physics Letters, 89, 032502, **2006**.

[22] A. Moser, H. J. Hug, I. Parashikov, B. Stiefel, O. Fritz, H. Thomas, A. Baratoff, H. -J. Güntherodt and P. Chaudhari, Observation of Single Vortices Condensed into a 125 Vortex-Glass Phase by Magnetic Force Microscopy, *Physical Review Letters*, 74**(**10), 1847-1850, **1995.**

[23] A. Volodin, K. Temst, A. Van Haesendonck, Y. Bruynseraede, M. I. Montero and I. K. Schuller, Magnetic Force Microscopy of Vortices in Thin Niobium Films: Correlation Between the Vortex Distribution and Thickness-Dependent Film Morphology, *Europhysics Letters*, 58(4), 582-588, **2002.**

[24] U. H. Pi, Z. G. Kim, D. H. Kim, A. Schwarz, M. Liebmann and R. Wiesendanger, Dynamic Force Spectroscopy Across an Individual Strongly Pinned Vortex in a Bi2Sr2CuCa2O8+δ Single Crystal, *Applied Physics Letters*, 85 (22), 5307-5309, **2004.**

[25] M. Roseman and P. Grütter, Determination of Tc, Vortex Creation and Vortex Imaging of a Superconducting Nb Film Using Low-Temperature Magnetic Force Microscopy, *Journal of Applied Physics*, 91(10), 8840-8842, **2002.**

[26] T. Shapoval, V. Neu, U. Wolff, R. Hühne, J. Hänisch, E. Backen, B. Holzapfel and L. Schultz, Study of Pinning Mechanism in YBCO Thin Films by Means of Magnetic Force Microscopy, *Physica C*, 460-462, 732-733, **2007**.

[27] E.W. J. Straver, J. E. Hoffman, O. M. Auslaender, D. Rugar, and K. A. Moler, Controlled Manipulation of Individual Vortices in a Superconductor, *Applied Physics Letters*, 93, 172514, **2008.**

[28] O. M. Auslaender, L. Luan, E. W. J. Straver, J. E. Hoffman, N. C. Koshnick, E. Zeldov, D. A. Bonn, R. Liang, W. N. Hardy and K. A. Moller, Mechanics of Individuals Isolated Vortices in a Cuprate Superconductor, *Nature Physics*, 5, 35-39, **2008**.

[29] L. Luan, O. M. Auslaender, D. A. Bonn, R. Liang, W. N. Hardy and K. A. Moler, Magnetic Force Microscopy Study of Interlayer Kinks in Individual Vortices in the Underdoped Cuprate Superconductor YBa2Cu3O6+x, *Physical Review B*, 79, 214530, **2009.**

[30] A. Schwarz, M. Liebmann, U. Kaiser and R. Wiesendanger, Visualization of the Barkhausen Effect by Magnetic Force Microscopy, *Physical Review Letters*, 92(7), 077206, **2004**.

[31] M. Liebmann, A. Schwarz, U. Kaiser, R. Wiesendanger, D.-W. Kim, and T. W. Noh, Magnetization Reversal of a Structurally Disordered Manganite Thin Film with Perpecdicular Anisotropy, *Physical Review B*, 71, 104431, **2005**.

[32] W. Wu, C. Israel, N. Hur, S. Park, S. W. Cheong, and A. de Lozanne, Magnetic Imaging of a Supercooling Glass Transition in a Weakly Disordered Ferromagnet, *Nature Materials*, 5, 881-886, **2006**.

[33] A.Lakhani, P. Kushwaha, R. Rawat and P. Chaddah, Magnetic Force Microscopic Study of the Magnetic Field Induced Antiferro to Ferrimagnetic Transition in Mn1.85Co0.15Sb, *Applied Surface Science*, 256(2), 404-406, **2009**.

[34] P. Milde, D. Köhler, J. Seidel, L. M. Eng, A. Bauer, A. Chacon, J. Kindervater, S. Mühlbauer, C. Pfleiderer, S. Buhrandt, C. Schütte, A. Rosch, Unwinding of a Skyrmion Lattice by Magnetic Monopoles, *Science*, 340, 1076-1080, **2013**.

[35] A. Schwarz and R. Wiesendanger, Magnetic Sensitive Force Microscopy, *Nanotoday*, 3(1-2), 28-39, **2008**.

[36] H. J. Hug, B. Steifel, P. J. A. van Schendel, A. Moser, S. Martin, and H.-J. Güntherodt, A Low Temperature Ultrahigh Vacuum Scanning Force Microscope, *Review of Scientific Instruments*, 70(9), 3625-3640, **1999.**

[37] D. Rugar, H. J. Mamin and P. Guethner, Improved Fibre Optic Interferometer for Atomic Force Microscopy, *Applied Physics Letter*, 55, 2588-2590, **1989.** 127

[38] D. Rugar, H. J. Mamin, R. Erlandson, J. E. Stern and B. D. Terris, Force Microscope Using a Fibre-Optic Displacement Sensor, *Review of Scientific Instruments*, 59 (11), 2337-2340, **1988.**

[39] A. Moser, H. J. Hug, Th. Jung, U. D. Schwarz and H-J. Güntherodt, A Miniature Fibre Optic Force Microscope Scan Head, *Measurement Science and Technology*, 4, 769-775, **1993**.

[40] Martin, Y.; Wickramasinghe, H. K., Magnetic imaging by force microscopy with 1000-A˚resolution. Applied Physics Letters 1987, 50 (20), 1455–57.

[41] Martin, Y.; Rugar, D.; Wickramasinghe, H. K., High-resolution magnetic imaging of domains in TbFe by force microscopy. Applied Physics Letters 1988, 52 (3), 244–46.

[42] Mamin, H. J.; Rugar, D.; Stern, J. E.; Terris, B. D.; Lambert, S. E., Force microscopy of magnetization patterns in longitudinal recording media. Applied Physics Letters 1988, 53 (16), 1563–65.

[43] Abelmann, L.; Porthun, S.; Haast, M.; Lodder, C.; Moser, A.; Best, M. E.; van Schendel, P.J. A.; Stiefel, B.; Hug, H. J.; Heydon, G. P.; Farley, A.; Hoon, S. R.; Pfaffelhuber, T.; Proksch, R.; Babcock, K., Comparing the resolution of magnetic force microscopes using the CAMST reference samples. Journal of Magnetism and Magnetic Materials 1998, 190 (1–2), 135–47.

[44] Lin, C. W.; Fan, F.-R. F.; Bard, A. J., High resolution photoelectrochemical etching of n-GaAs with the scanning electrochemical and tunneling microscope. Journal of the Electrochemical Society 1987, 134 (4), 1038–39.

[45] Hosaka, S.; Kikukawa, A.; Honda, Y.; Hasegawa, T., Just-on-surface magnetic force microscopy.Applied Physics Letters 1994, 65 (26), 3407–9.

[46] Mamin, H. J.; Rugar, D.; Stern, J. E.; Terris, B. D.; Lambert, S. E., Force microscopy of magnetization patterns in longitudinal recording media. Applied Physics Letters 1988, 53 (16), 1563–65.

[47] Porthun, S.; Abelmann, L.; Lodder, C., Magnetic force microscopy of thin film media for high density magnetic recording. Journal of Magnetism and Magnetic Materials 1998, 182 (1–2), 238–73.

[48] Schreiber, S.; Savla, M.; Pelekhov, D. V.; Iscru, D. F.; Selcu, C.; Hammel, P. C.; Agarwal, G.,Magnetic force microscopy of superparamagnetic nanoparticles. Small 2008, 4 (2), 270–78.

[49] Karcı, Ö. (2015). Design of A Self-Aligned, High Resolution, Low Temperature (30 Mk-300 K) Magnetic Force Microscope.

[50] Wittborn, J. (2000). Nanoscale studies of functional materials using scanning probe microscopy (Doctoral dissertation, Materialvetenskap).

[51] Correa Orellana, A. (2018). Magnetic Force Microscopy study of layered superconductors in vectorial magnetic fields.

[52] Peng Pan, Feiyu Yang, Zhenhua Wang, Bowen Zhong, Lining Sun, and Changhai Ru. *A Review of Stick–Slip Nanopositioning Actuators*, pages 1–32. Springer International Publishing, Cham, 2016.

[53]"PiezoelectricTubeScanners."*PiezoDrive*,2019,www.piezodrive.com/actuators/piezoelectric-tube-scanners/.

[54] H. Kuramochi, T. Uzumaki, M. Yasutake, A. Tanaka, H. Akinaga and H. Yokoyama, A Magnetic Force Microscope Using CoFe-Coated Carbon Nanotube Probes, *Nanotechnology*, 16, 24-27, **2005**.

[55] A. Winkler, T. Mühl, S. Menzel, R. K.-Koseva, S. Hampel, A. Leonhardt and B. Büchner, Magnetic Force Microscopy Sensors Using Iron-Filled Carbon Nanotubes, *Journal of Applied Physics*, 99, 104905, **2006**.

[56] I. Utke, P. Hoffmann, R. Berger and L. Scandella, High-Resolution Magnetic Co Supertips Grown by a Focused Electron Beam, *Applied Physics Letters*, 80(25), 4792-4794, **2002**.

[57] L. Gao, L. P. Yue, T. Yokota, R. Skomski, S. H. Liou, H. Takahoshi, H. Saito and S. Ishio, Focused Ion Beam Milled CoPt Magnetic Force Microscopy Tips for High Resolution Domian Images, *IEEE Transactions on Magnetics*, 40(4), 2194-2196, **2004**.

[58] L. M. Belova, O. Hellwig, E. Dobisz and E. D. Dahlberg, Rapid Preparation of Electron Beam Induced Deposition Co Magnetic Force Microscopy Tips with 10 nm Spatial Resolution, *Review of Scientific Instruments*, 83, 093711, **2012**.

[59] O. Teschke, Micromagnetic Structure Images Taken Using Platinum Coated Tips, *Applied Physics Letters*, 79(17), 2773-2775, **2001**.

[60] Nanosensors Inc., Rue Jaquet- Droz 1, Case Postale 216, CH-2002, Neuchatel, Switzerland

[61] Karcı, Ö., Dede, M., & Oral, A. (2014). Design of a self-aligned, wide temperature range (300 mK-300 K) atomic force microscope/magnetic force microscope with 10 nm magnetic force microscope resolution. *Review of Scientific Instruments*, *85*(10), 103705.

[62] T. Fukuma and S. P. Jarvis, Development of Liquid-Environment Frequency Modulation Atomic Force Microscope with Low Noise Deflection Sensor for

Cantilevers of Various Dimensions, *Review of Scientific Instruments*, 77, 043701, **2006**.

[63]TappingModeAFM, 019,www.nanophys.kth.se/nanophys/facilities/nfl/afm/fast-scan/bruker-elp/Content/TappingMode%20AFM/TappingMode%20AFM.htm.

[64] Choi, S. J., Kim, K. H., Cho, Y. J., Cho, S. H., Kwon, S. J., Moon, J. H., & Lee, K. J. (2010). Demonstration of ultra-high-resolution MFM images using Co90Fe10-coated CNT probes. *Journal of Magnetism and Magnetic Materials*, *322*(3), 332-336.

[65] 2019, www.physlab.org/wp-content/uploads/2016/04/VSM-Service-Manual-Evacuating-and-Recharging-the-System-min.pdf.

[66] Banjare, Y. P. (2009). Theoretical and experimental studies on pulse tube refrigerator (Doctoral dissertation).

[67] "Closed Cycle Cryocooler Principles of Operation." *Advanced Research ystems*, 2019, www.arscryo.com/cryocooler-principles-of-operation.

[68] Newport Corp., S2000 Stabilizer Series.1791 Deere Avenue, Irvine, CA 92606, United States.

[69] A. Oral, R. A. Grimble, H. Ö. Özer and J. B. Pethica, High-Sensitivity NonContact Atomic Force Microscope/Scanning Tunneling Microscope (nc AFM/STM) Operating at Subangstrom Oscillation Amplitudes for Atomic Resolution Imaging and Force Spectroscopy, *Review of Scientific Instruments*, 74(8), 3656-3663, **2003**.

[70] B. W. Hoogenboom, P. L. T. M. Frederix, J. L. Yang, S. Martin, Y. Pellmont, M. Steinacher, S. Zäch, H. Heimbeck, A. Engel, and H. J. Hug, A Fabry–Perot Interferometer for Micrometer-Sized Cantilevers, *Applied Physics Letters*, 86, 074101, 5–8, **2005**.

[71] H. I. Rasool, P. R. Wilkinson, A. Z. Stieg, and J. K. Gimzewski, A Low Noise All-Fibre Interferometer for High Resolution Frequency Modulated Atomic Force Microscopy Imaging in Liquids, *Review of Scientific Instruments*, 81, 023703, **2010**.

[72] B. W. Hoogenboom, P. L. T. M. Frederix, D. Fotiadis, H. J. Hug, and A. Engel, Potential of Interferometric Cantilever Detection and Its Application for SFM/AFM in Liquids, *Nanotechnology*, 19, 384019, **2008**.

[73] D. T. Smith, J. R. Pratt, and L. P. Howard, A Fibre-Optic Interferometric with Subpicometer Resolution for DC and Low-Frequency Displacement Measurement, *Review of Scientific Instruments*, 80, 035105, **2009**.

[74] H. Hölscher, P. Milde, U. Zerweck, L. M. Eng, and R. Hoffmann, The Effectiv Quality Factor at Low Temperatures in Dynamic Force Microscopes with Fabry-Pérot Interferometer Detection, *Applied Physics Letters*, 94, 223514, **2009**.

[75] Subba-Rao, V., Sudakar, C., Esmacher, J., Pantea, M., Naik, R., & Hoffmann, P. M. (2009). Improving a high-resolution fiber-optic interferometer through deposition of a TiO 2 reflective coating by simple dip-coating. *Review of Scientific Instruments*, *80*(11), 115104.